Semiconductor optical amplifier based wavelength converters for photonic transmission systems

2002

Toshio Ito

Abstract

Increasing the bit rate per wavelength division multiplexing (WDM) channel, not only increasing the number of channels, is attractive for upgrading the traffic capacity of optical transmission systems. The remaining problems are the difficulties in connecting different types of WDM system, and the signal waveform distortion due to the polarization mode dispersion (PMD). Therefore, a simultaneous wavelength conversion and high bit rate PMD compensation are expected. Semiconductor optical amplifier (SOA) based wavelength conversion is the most promising device for those subsystems, because of its advantages of bit-rate-independent and format-independent operation.

Chapter 1: The background and the purpose of this work are described.

Chapter 2: The described SOA has an extremely low loss-less current of 5.4 mA, which is the lowest record so far reported. The scattering of the polarization dependence gain (PDG), which is due to the unintended stain in the active layer, is within 0.5 dB, while the scattering in conventional SOA is 2.5 dB.

An SOA array integrated with spot size converter (SS-SOA) has been fabricated for connecting the SOA to planar lightwave circuit (PLC). To reduce the evaluation cost, I have proposed a novel method of measuring the PDG. By averaging the signal gain over a wide wavelength range, the PDG can be accurately estimated with low reflection from gain ripples. The PDG of an angled-facet SS-SOA was successfully evaluated even before the AR coating process.

Chapter 3: Chapter 3 discusses hybrid integration of SS-SOA and PLC. Hybrid integration is attractive to fabricate practical modules with functional PLC, such as arrayed waveguide grating (AWG).

A 4-channel SS-SOA gate array was assembled on a PLC platform for the first time. It has an extinction ratio higher than 35 dB, operating at less than 50 mA. The PDG is less than 1 dB throughout an ultra-wide-band of 1530-1600 nm. The spot-size converting structure of the SS-SOA reduces the coupling loss to 4 dB, and improves the horizontal 1-dB down tolerance to 2 μm.

Using the SS-SOA gate array and AWG, first in the world, a high-speed wavelength selector was demonstrated. The rise- and fall-times were less than 1 ns, which is fast enough for packet switching.

Chapter 4: Chapter 4 describes photonic subsystems for upgrading transmission network.

I demonstrated, for the first time, a simultaneous wavelength conversion from C- to L-band using four-wave mixing (FWM) in a wavelength selector. Another type of simultaneous wavelength conversion, from equal to unequal channel spacing, was demonstrated using cross-gain modulation (XGM). My aim is not a random wavelength switching but a fixed wavelength shifting to connect different networks. This allows easy operation and control, which is necessary for practical use.

I proposed a novel technique in monitoring the state of the differential group delay (DGD) of an optical fiber. Thanks to the XOR operation of the cross phase modulation (XPM), this technique is bit-rate independent and format independent. The PMDs of 80-Gbit/s RZ format and 40-Gbit/s NRZ format were successfully compensated. The power penalty was only 0.9 dB.

Chapter 5: The main results of this study, which shows the possibility to solve the main problems of future high-speed WDM systems, the polarization mode dispersion (PMD) compensation and simultaneous wavelength conversion, are summarized.

Contents

Chapter 1

Introduction

Chapter 1 describes the background and purpose of this thesis. The history and problems of wavelength division multiplexing (WDM) networks are summarized. Novel approach using all-optical signal processing as simultaneous wavelength conversion, bit rate conversion, and polarization mode dispersion (PMD) compensation, are proposed to upgrade WDM networks. Notice that those new technologies can be used with simple and easy control circuits. Semiconductor optical amplifier (SOA) based wavelength converter is expected as a key device for realizing these subsystems, because of its superior properties of bit rate transparency and format independency.

intervals.

WDM introduced a third degree of freedom, adding wavelength to space and time as a dimension in which system capacity could expand. It successfully overcame the bandwidth limit of the traditional time division multiplexing by multiplying the number of high bit rate channels. With the introduction of dense WDM, commercial systems are approaching terabit per second (Tbit/s) per fiber, to accommodate the increasing number of broadband subscribers and satisfy the demand for higher-quality services. The developments of Erbium-doped fiber amplifier (EDFA) has resulted in the progress of various types of WDM system; the S-band (1460-1530 nm) [1.1, 1.2] C-band (1530-1565 nm)[1.1, 1.2], and L-band (1565-1625 nm) [1.3] have all been used. Several networks use equal-channel spacing, such as 25, 50 and 100 GHz, with conventional single-mode fibers [1.1, 1.2], while others have adopted unequal-channel spacing to avoid four-wave-mixing (FWM) impairment over dispersion-shifted fiber (DSF) [1.1, 1.4]. Unequal-channel spacing that repeats 60/80 GHz spacing also increases the number of WDM channels in the EDFA-band [1.5].

However, problems, such as the limited wavelength resources and the insufficient flexibility of the photonic networks, remain. Increasing the bit rate per WDM channel, not only increasing the number of WDM channels, is attractive for upgrading the capacity of WDM systems and reducing the demand on wavelength resources.

Internet traffic is still growing at a rate of 100% per year, though this is much slower than the frequently heard claims in the mid nineties (1995/1996) that the growth rate would double every three or four months. This continuous growth is driving photonics technology toward ever-increasing capacity in both backbone long-haul fiber networks, flexible metro-networks, and access networks. A sufficiently high bit rate of 10 Gbit/s per WDM channel will be required for metro-network (Fig. 1-2). For long-haul transmissions, a higher (> 40-Gbit/s) bit rate will be needed in order to enlarge the total throughput with a limited number of wavelengths and O/E converters. Already, transmission systems of 40 Gbit/s per WDM channel and 10 Tbit/s per fiber have been demonstrated [1.5, 1.6], as shown in Fig. 1-3. It is expected that in the next

several years, the bit rate will begin to be limited by the 50-THz transmission bandwidth of silica optical fiber.

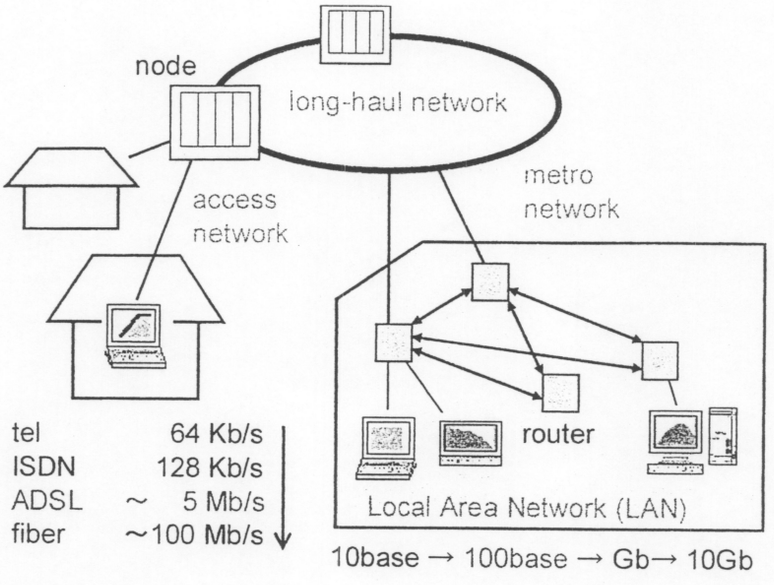

Figure 1-2 Increase of bit rate per user

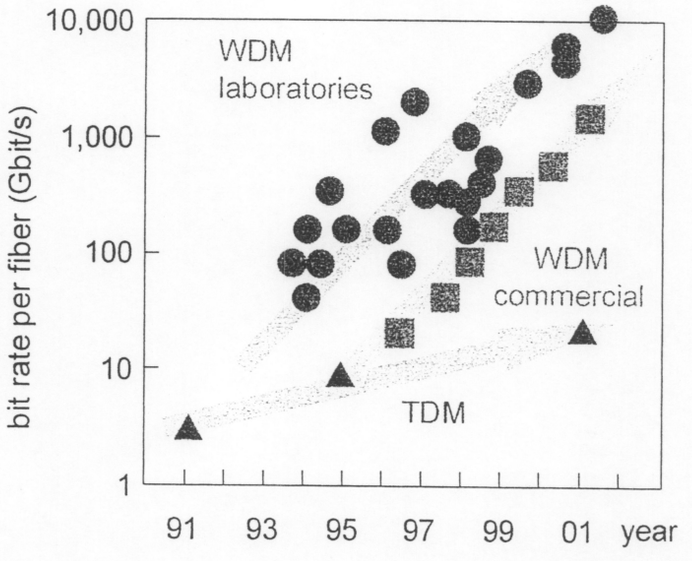

Figure 1-3 Increase of bit rate per fiber

1.1.2. Problems in upgrading WDM systems

The growing need for more channels and higher bit rate brings several new challenges. One of the most serious is polarization mode dispersion (PMD). PMD, which is caused by the slight birefringence of the optical fiber, is an obstacle to upgrading long-haul transmission networks, because it results in waveform distortion by causing differential group delay (DGD) between the two principal polarization states, as shown in Fig. 1-4. As describe below, the maximum fiber length decreases with increasing bit rate, due to the PMD.

The DGD value is estimated as $DGD = K \cdot L^{0.5}$ [ps], where L [km] is optical fiber length. The constant K [ps/km$^{0.5}$] is from 0.05 (newest fiber) to 2.0 (as is often the case for US traditional fiber), and typically 0.2. Normally, the DGD value, which is found as a timing jitter of the optical signal, must be less than 1/10 of the bit width. Therefore, the maximum fiber length L, assuming $K=0.2$, is 2500 km for 10 Gbit/s (bit width = 100 ps) but only 156 km for 40 Gbit/s (bit width = 25 ps).

Another problem is the difficulty in connecting different types of WDM systems. Recent progress in EDFA and high-speed modulation technique has led to flexible networks with different wavelengths, channel spacings, or bit rates. Then, two conversion systems, simultaneous wavelength conversion and bit-rate conversion, are expected to support the connection of near-future photonic networks. Simultaneous wavelength conversion aims to connect different WDM systems with different wavelengths or channel spacings, and the full bit-rate conversion aims to connect

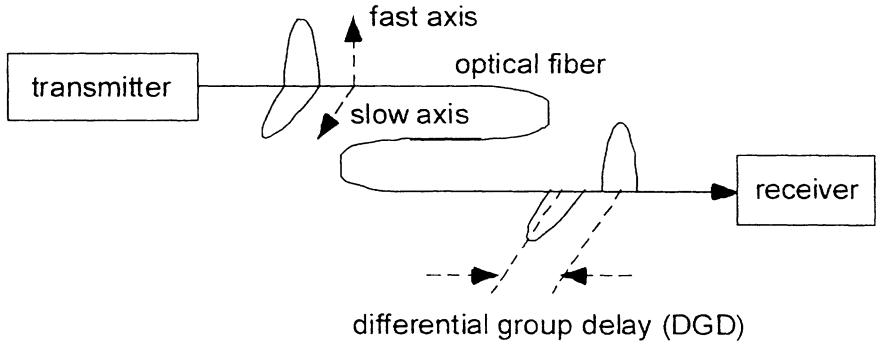

Figure 1-4 Polarization mode dispersion (PMD) of a optical fiber

relatively slow 10-Gbit/s local networks to fast 40-Gbit/s backbone networks. A number of efforts have focused on achieving these conversions, as summarized next.

1.2. Conventional techniques used in WDM systems

1.2.1. Simultaneous wavelength conversion

Simultaneous wavelength conversion of multi-WDM channels is expected to be a key technique for connecting networks with different bands or channel spacings. So far, ten-channel wavelength conversion with 9-GHz channel spacing and a 140-Mbit/s modulation rate has been achieved by using four-wave-mixing (FWM) in a semiconductor optical amplifier (SOA) [1.7]. Watanabe et al. demonstrated five-channel wavelength conversion using FWM with a highly-nonlinear-fiber [1.8]. The FWM technique, as shown in Fig. 1-5, is very simple and useful because it needs only a single FWM device and a single pump source for conversion. However, the signal-to-noise ratio (SNR) drops rapidly with increasing channel number [1.9], and the power level fluctuates due to the saturation output power of the single converter. This tendency will

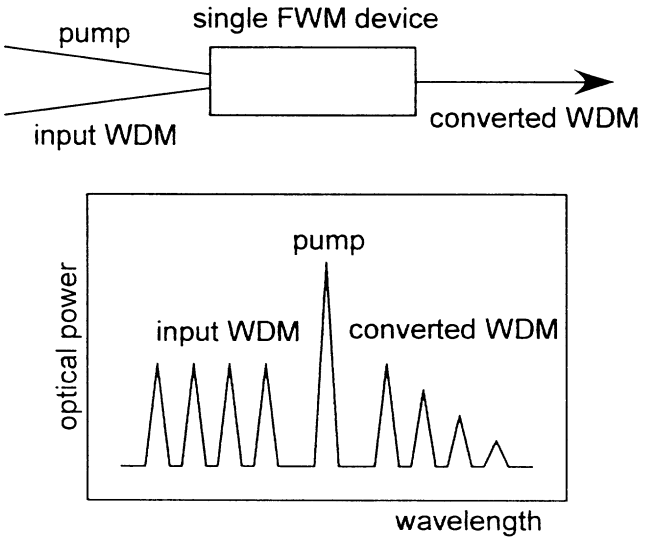

Figure 1-5 Simultaneous wavelength conversion using four-wave mixing (FWM)

become more pronounced when the number of the WDM channels varies as a result of network reconfiguration or network failure. Furthermore, it is impossible to change the WDM channel spacing, for example from 100 GHz to 50 GHz or from equal to unequal, in a single FWM device.

1.2.2. Full bit rate conversion

Figure 1-6 shows what the network configuration will look like in the near future. The huge amount of data traffic will require a high bit rate of 10 Gbit/s, even in metropolitan networks. The long-haul backbone network, which serves a number of metropolitan networks, will need an extremely high bit rate of more than 40 G networks and extremely high-speed 40-Gbit/s long-haul networks is indispensable, because it is clear that most metropolitan users will not use the full capacity of 40 Gbit/s. All optical bit-rate conversion has a merit of bit-rate independent operation, and has a potential o overcome the speed limit of electrical devices. Prior to bit-rate conversion, a simple technique that adjusts the phase of the 10-Gbit/s channels is needed. Furthermore, the conversion should operate for random WDM channel wavelength.bit/s. Therefore, practical full bit-rate conversion between high-speed 10-Gbit/s metropolitan

For all-optical bit-rate conversion, extremely high-speed wavelength conversion using differential-phase modulation (DPM) is one of the most promising

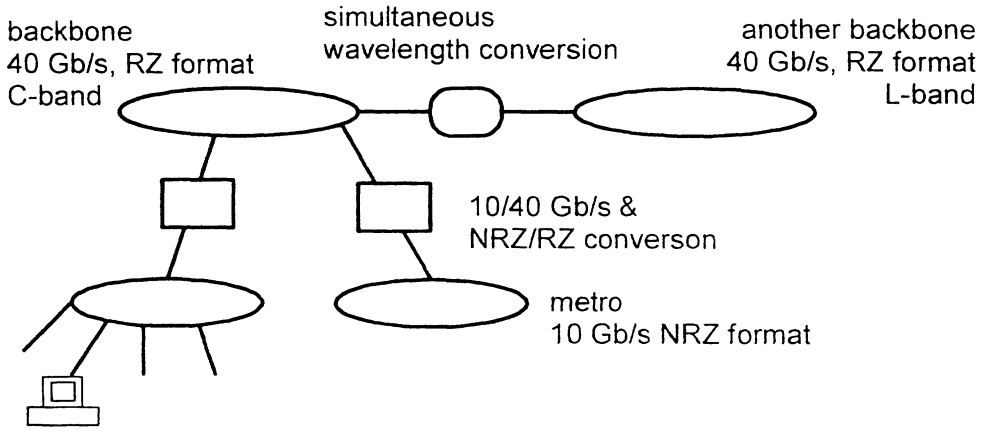

Figure 1-6 Network configuration in the near future

approaches [1.10, 1.11]. Several papers have reported extremely high-speed operation of more than 100 Gbit/s [1.12, 1.13]. However, there have been few DPM devices aiming for practical use, such as in filterless operation [1.14] for a large wavelength range. We have proposed a DPM wavelength converter with a monolithic Sagnac Interferometer integrated with Parallel-Amplifier Structure (SIPAS) [1.15, 1.16]. SIPAS has low wavelength dependence and can divide the input and converted signal, which promises filterless operation. It should be noted that DPM devices usually need the return-to-zero (RZ) format, while 10-Gbit/s WDM systems use the non-return-to-zero (NRZ) format. This RZ format is also convenient for high-speed optical transmission, because the short-pulse RZ signal reduces the signal degradation from fiber nonlinearities, such as self-phase modulation [1.17, 1.18]. Extremely high-speed systems are being developed at laboratories around the world. TDM to WDM conversion and WDM to TDM reconversion have been demonstrated using a supercontinum source [1.19]. TDM to WDM signal format translation has been achieved using bi-directional FWM in a SOA [1.20], or monolithic Mach-Zehnder interferometer (MZI) module [1.21]. B. Mikkelsen et al. reported RZ to NRZ conversion using monolithic integrated active Michelson interferometer [1.22]. However, a total experiment comprising bit-rate conversion and reconversion, including NRZ to RZ format conversion and reconversion, as well as phase adjustment for random WDM channels, had not been done until the present work.

1.2.3. Polarization mode dispersion (PMD) compensation

The compensation of PMD is an important issue for high-speed photonic networks. Monitoring the state of the differential group delay (DGD) is indispensable for PMD compensation, as shown in Fig. 1-7, and several approaches have been implemented using electronic circuits. A simple method for DGD monitoring is to measure the intensity of half the frequency of the input signal. It is an elegant method because only a photodiode (PD), a narrow band-pass filter (BPF), and a power meter are needed. Using this method, the PMD of a 40-Gbit/s signal in NRZ format has been

equalized [1.23, 1.24]. However, this technique requires a high-speed PD, for example, 20 GHz for 40 Gbit/s, which prevents the network upgrading to more than 100-Gbit/s. The BPF should be strictly adjusted to the input frequency, which disturbs the bit-rate transparency of photonic networks. Moreover, the BPF is difficult to use in an RZ format, especially in systems using a short pulse of a few ps.

Another technique for DGD monitoring involves evaluating the eye opening of the data signals [1.25]. This technique provides the most reliable information because the eye opening has a high correlation to the bit error rate (BER), which is the final target for improvement. However, the bit rate in this method is limited by the operation speed of the decision circuit and electronic exclusive OR (XOR) circuit, which is about 40 Gbit/s.

For the polarization mode dispersion (PMD) compensation of extremely high-speed signal of more than 80 Gbit/s, optical monitoring techniques are expected. Rosenfeldt et al. demonstrated, first in the world, PMD compensation at 80 Gbit/s, using a polarization-resolved evaluation of the degree of polarization (DOP) combined with a polarization scrambler at the fiber input [1.26]. Another technique for 160-Gbit/s compensation monitors the eye opening of the data signals using an optical sampling eye monitoring method [1.27]. This technique provides the most reliable information because the eye opening has a high correlation to the bit error rate (BER), which is the final target for improvement. However, both techniques may need large and expensive equipment for each WDM channel, which would make them difficult to use in large WDM systems with numerous channels.

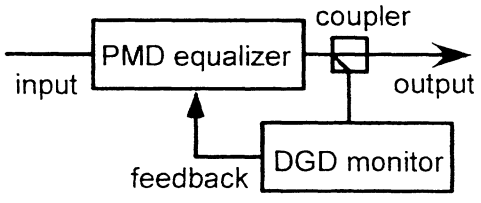

Figure 1-7 Configuration of PMD compensator

1.3. Novel approach using all-optical signal processing

1.3.1. All-optical signal processing using wavelength conversion technique

This thesis presents optical devices for future transmission systems. The conventional transmission systems have mainly used electrical devices. It is well known that electrical devices, such as CPUs and buffer memories in computers, are very intelligent and perform complex operations, such as packet routing, buffering, retiming/reshaping of distorted pulses, and error correction to improve the bit error rates (BERs) of the transmitted optical signals.

Though optical devices have advantages of bit-rate transparency and format independency, most of them are difficult to control. Optical devices cannot read the headers of optical packets, nor can they memorize a bit stream series. Even a perfect optical switch, i.e., one that is fast, large scale, lossless and noiseless, may be unusable in future systems, unless someone find a good way to receive the "control information", such as "switch from which port to which port?" or "when is the start time for switching?"

However, two optical devices have achieved great successes in commercial use. One is the erbium doped fiber amplifier (EDFA), which has replaced electrical 3R (regeneration, reshaping and retiming circuits), and the other is the arrayed waveguide grating (AWG), which has replaced electrical matrix switches. Both are "passive" and do not need control circuits, which may be key points in achieving efficient optical devices.

This thesis describes several photonic subsystems for simultaneous wavelength conversion, bit rate conversion and polarization mode dispersion (PMD) compensation. Direct connections between different optical networks were successfully demonstrated. Using wavelength conversion techniques, these all-optical processing provide bit-rate and format transparency. The same wavelength converters can be used in both 10-Gbit/s and 160-Gbit/s networks. They do not matter if the signal format changes from NRZ to RZ. Furthermore, they have the possibility to be used in future commercial networks,

because no complex control circuits are needed. We are sure that, in the near-future, those subsystems will upgrade the scale and capacity of WDM transmission systems.

1.3.2. Hybrid integration of SOA and PLC

The above subsystems use semiconductor optical amplifier (SOA) based wavelength conversion techniques such as four-wave mixing (FWM), cross-gain modulation (XGM), cross-phase modulation (XPM), and differential-phase modulation (DPM). The SOA has superior characteristics of large signal amplification, small size, high efficiency and low power consumption.

Another important issue is the fabrication cost of the wavelength converter module. To enlarge the misalignment tolerance, two spot-size converters were integrated to both side of an SOA. An integrated passive optical circuit that uses a silica waveguide on silicon substrate, named a planar lightwave circuit (PLC), is used as a platform. Figure 1-8 show the hybrid integration between SOA and PLC. Passive alignment technique is used to reduce the fabrication cost.

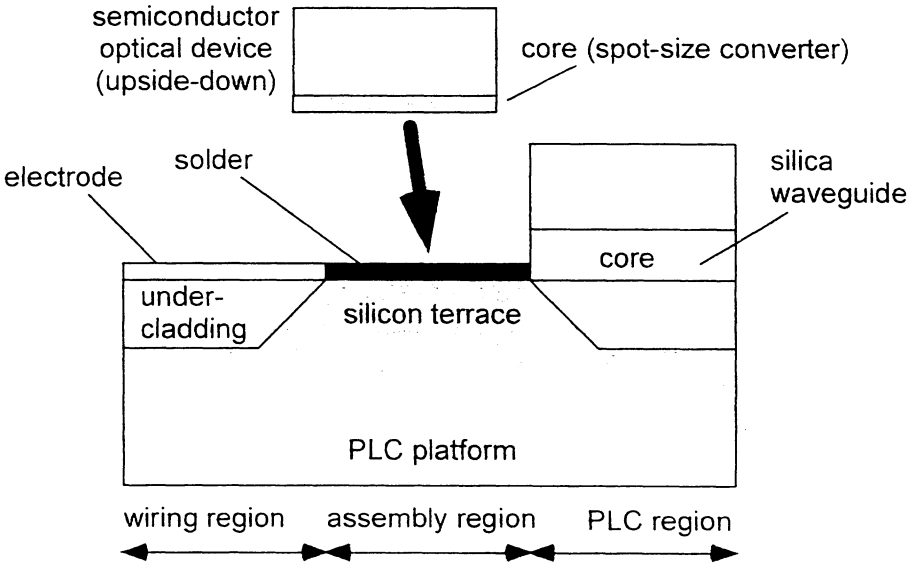

Figure 1-8 Cross-sectional view of a PLC platform

1.4. Summary of Chapter 1

With the progress of the wavelength division multiplexing (WDM) system, both the bit rate and the number of channels are increasing. Many types of bit rates and signal formats are used in the same time, in the same system. Optical signal processing is attractive for upgrading the WDM system, because of its superior characteristics of bit rate and format independent.

The problems of WDM systems are the difficulties in connecting different types of WDM system, and the signal waveform distortion due to the polarization mode dispersion (PMD). Therefore, a simultaneous wavelength conversion and high bit rate PMD compensation are expected. Electronic technologies have been developed to solve these problems, but the bit rate and format dependence in electronic circuit limit the traffic capacitance of the WDM system.

In this thesis, a novel approach using semiconductor optical amplifier (SOA) based wavelength conversion is presented. It is one of the most promising devices, because of its advantages of bit-rate-independent and format-independent operation.

References in Chapter 1

1.1. J. Kani, T. Sakamoto, M. Jinno, K. Hattori, M. Yamada, T. Kanamori, and K. Oguchi, "Novel 1470-nm-band WDM transmission and its application to ultra-wide-band WDM transmission", IEICE Trans. Commun., vol. E82-B, no. 8, pp. 1131-1139, Aug. 1999.

1.2. A. K. Srivastava, D. L. Tzeng, A. J. Strentz, J. E. Johnson, M. L. Pearsall, O. Mizuhara, T. A. Strasser, K. F. Dreyer, J. W. Sulhoff, L. Zhang, P. D. Yeates, J. R. Pedrazzani, A. M. Sergent, R. E. Tench, J. M. Freund, T. V. Nguyen, H. Manar, Y. Sun, C. Wolf, M. M. Choy, R. M. Kummer, D. Kalish, and A. R. Chrapilyvy, "High-speed WDM transmission in allwave™ fiber in both the 1.4-μm and 1.55-μm bands", Proc. 9th Opt. Amp. and their Applications (OAA), Vail, Colorado, post deadline paper, PD 2, 1998.

1.3. T. Sakamoto, K. Hattori, M. Fukutoku, M. Fukui, M. Jinno, and K. Oguchi, "Properties of gain-shifted EDFA (1580 nm-band EDFA) cascades in WDM transmission systems", Proc. 9th Opt. Amp. and their Applications (OAA), Vail, Colorado, TuB3, pp. 88-91, 1998.

1.4. F. Forghieri, R. W. Tkach, A. R. Chraplyvy, and D. Marcue, "Reduction of four-wave mixing crosstalk in WDM systems using unequally spaced channels", IEEE Photon. Technol. Lett., vol. 6, pp.754-756, 1994.

1.5. S. Bigo, Y. Frignac, G. Charlet, W. Idler, S. Borne, H. Gross, R. Dischler, W. Poehlmann, P. C. Tran, D. Bayart, G. Veith, A. Jourdan, and J.-P. Hamaide, "10.2 Tbit/s (256x42.7 Gbit/s PMD/WDM) transmission over 100 km TeraLight™ fiber with 1.28 bit/s/Hz spectral efficiency", Optical Fiber Communication Conference and Exhibit, (OFC), Anaheim, CA, USA, PD25-P1-3, vol. 4., 2001.

1.6. K. Fukuchi, T. Kasamatsu, M. Morie, R. Ohhira, T. Ito, K. Sekiya, D. Ogasawara, and T. Ono, "10.92-Tb/s (273x40-Gb/s) triple-band/ ultra-dense WDM optical repeated transmission experiment", Optical Fiber Communication Conference and Exhibit, (OFC), Anaheim, CA, USA,

PD24-P1-3, vol. 4., 2001.

1.7. R. Schnabel, U. Hilbk, Th. Hermes, P. Meiβner, Cv. Helmolt, K. Magari, F. Raub, W. Piepper, F.J. Westphal, R. Ludwig, L. Kuller, and H. G. Weber, "Polarization insensitive frequency conversion of a 10-channel OFDM signal using four-wave-mixing in a semiconductor laser amplifier", IEEE Photon. Tech. Lett., vol. 6, no. 1, pp. 56-58, Jan. 1994.

1.8. S. Watanabe, S. Takeda, G. Ishikawa, H. Ooi, J. G. Nielsen, and C. Somme, "Simultaneous wavelength conversion and optical phase conjugation of 200-Gbit/s (5x40 -Gbit/s) WDM signal using a highly nonlinear fiber four wave mixer", Proc. 11th International Conf. on Integrated Optics and Optical Fibre Communications (IOOC), and 12th European Conf. on Opt. Commun. (ECOC), Edinburgh, UK, Vol. 5, post-deadline papers, TH3A, pp. 1-4, Sept. 1997.

1.9. A. Mecozzi, S. Scotti, A. D'Ottavi, E. Iannone, and P. Spano, "Four-wave mixing in traveling-wave semiconductor amplifiers", Journ. Quant. Elect., vol. 31, no. 4, pp.689-699, Apr. 1995.

1.10. E. Jahn, N. Agrawal, W. Pieper, H.-J. Ehrke, D. Franke, W. Furst, and WEINERT, C.M. Weinert, "Monolithically integrated nonlinear Sagnac interferometer and its application as a 20 -Gbit/s all-optical demultiplexer", Electron. Lett., vol. 32, no. 9, pp. 782 –784, 1996.

1.11. M. Vaa, B. Mikkelsen, K. S. Jepsen, K. E. Stubkjaer, M. Schilling, K. Daub, E. Lach, G. Laube, W. Idler, K. Wunstel, S. Bouchoule, C. Kazmierski, and D. Mathoorasing, "A bit rate flexible and power efficient all-optical demultiplexer realized by monolithically integrated michelson interferometer", 22nd European Conference on Optical Communication, ECOC' 1996, Oslo, Norway, ThB.3.3, pp. 5.11-5.14, 1996.

1.12. J. Leuthold, C. H. Joyner, B. Mikkelsen, G. Raybon, J. L. Pleumeekers, B. I. Miller, K. Dreyer, and C. A. Burrus, "100-Gbit/s all-optical wavelength conversion with integrated SOA delayed-interference configuration", Electron. Lett., vol. 36, no. 12, pp. 1129 –1130, 2000.

1.13. S. Nakamura, Y. Ueno, K. Tajima, J. Sasaki, T. Sugimoto, T. Kato, T. Shimoda, M. Itoh, H. Hatakeyama, T. Tamanuki, and T. Sasaki, "Demultiplexing of 168-Gbit/s data pulses with a hybrid-integrated symmetric Mach-Zehnder all-optical switch", IEEE Photon. Technol. Lett., vol. 12, no. 4, pp. 425 –427, 2000.

1.14. D. Wolfson, T. Fjelde, A. Kloch, C. Janz, F. Ponigt, F. Pommereau, I. Guillemot, F. Gaborit, and M. Renaud, "Detailed experimental investigation of all-active dual-order mode Mach-Zehnder wavelength converter", Electron. Lett., vol. 36, no. 15, pp. 1296 –1297, 2000.

1.15. Y. Shibata, N. Kikuchi, S. Oku, T. Ito, H. Okamoto, Y. Kawaguchi, Y. Suzuki, and Y. Kondo, "Monolithically integrated parallel amplifiers structure for filter-free wavelength conversion" the Indium Phosphide and Related Materials, IPRM2001, FB1-5, Nara, Japan, pp. 587 –590, May 2001.

1.16. Y. Shibata, N. Kikuchi, S. Oku, T. Ito, H. Okamoto, Y. Kawaguchi, Y. Kondo, and Suzuki, "Filter-free wavelength conversion using a Sagnac interferometer integrated with parallel amplifiers structure (SIPAS)", the Optoelectronics and Communications Conference / the Integrated Optics and Optical Fibre Communication Conference, OECC/IOCC 2001, Sydney, Australia, pp.212-213, July 2001.

1.17. D. Breuer, and K. Petermann, "Comparison of NRZ- and RZ-modulation format for 40-Gbit/s TDM standard fiber systems", IEEE Photon. Technol. Lett., vol. 9, no. 3, pp. 398-400, 1997.

1.18. R. Ludwig, U. Feiste, E. Dietrich, H. G. Weber, D. Breuer, M. Martin, and F. Kuppers, "Experimental comparison of 40 -Gbit/s RZ and NRZ transmission over standard singlemode fibre", Electron. Lett., vol. 35, no. 25, pp. 2216 –2218, 1999.

1.19. T. Hashimoto, H. Sotobayashi, K. Kitayama, and W. Chujo, "Photonic conversion of OC-192 OTDM-to-4 x OC-48 WDM by supercontinuum generation", Electron. Lett., vol. 36, no. 13, pp. 1133 –1135, 2000.

1.20. A. Buxens, H. N. Poulsen, A. T. Clausen, and P. Jeppesen, "All-optical OTDM-to-WDM signal-format translation and OTDM add-drop functionality using bi-directional four wave mixing in semiconductor optical amplifier", Electron. Lett., vol. 36, no.2, pp. 156-158, 2000.

1.21. St. Fischer, M. Duelk, M. Puelo, R. Girardi, E. Gamper, W. Vogt, W. Hunziker, E. Gini, and H. Melchor, "40-Gbit/s OTDM to 4x10 -Gbit/s WDM conversion in monolithic InP Mach-Zehnder interferometer module", IEEE Photon. Tech. Lett., vol. 11, no. 10, pp.1262-1264, 1999.

1.22. B. Mikkelsen, M. Vaa, H. N. Poulsen, S. L. Danielsen, C. Joergensen, A. Kloch, P. B. Hansen, K. E. Stubkjaer, K. Wunstel, K. Daub, E. Lach, G. Laube, W. Idler, M. Schilling, and S. Bouchoule, "40 Gb/s all-optical wavelength converter and RZ-to-NRZ format adapter realized by monolithic integrated active Michelson interferometer", Electron. Lett., vol. 33, no. 2, pp. 133-134, 1997.

1.23. R. Noe, D. Sandel, M. Yoshida-Dierolf, S. Hinz, V. Mirvoda, A. Scopflin, C. Glingener, E. Gottwald, C. Scheerer, G. Fisher, T. Weyrauch and W. Haase, "Polarization mode dispersion compensation at 10, 20, and 40 Gb/s with various optical equalizer", IEEE J. Light. Technol., 17, pp. 1602-1616, 1999.

1.24. H. Ooi, Y. Akiyama, and G. Ishikawa, "Automatic polarization-mode dispersion compensation in 40 Gb/s transmission", Optical Fiber Communication Conference, 1999, and the International Conference on Integrated Optical Fiber Communication. OFC/IOOC'99. Technical Digest, vol. 2, pp. 86-88, 1999.

1.25. F. Buchali, S, Lanne, J.-P. Thiery, W. Baumert, and H. Bulow, "Fast eye monitor for 10 Gb/s and its application for optical PMD compensation", Optical Fiber Communication Conference and Exhibit, 2001, OFC'2001, vol. 2, TuP5-1, 2001.

1.26. H. Rosenfeldt, R. Ulrich, E. Brinkmeyer, U. Feiste, C. Schubert, J. Berger, R. Ludwig, H. G. Weber, and A. Ehrhardt, "Feed-forward approach for automatic PMD compensation at 80 Gbit/s over 45 km installed single mode fibre", 27th

European Conference on Optical Communication, ECOC' 2001, Amsterdam, The Netherlands, vol. 6, pp. 68-69, 2001.

1.27. H. Sunnerud, M. Westlund, Jie Li, J. Hansryd, M. Karlsson, P. Hedekvist, and P. A. Andrekson, "Long-term 160 Gb/s-TDM, RZ transmission with automatic PMD compensation and system monitoring using optical sampling system", 27th European Conference on Optical Communication, ECOC' 2001, Amsterdam, The Netherlands, vol. 6, pp. 18-19, 2001.

Chapter 2

Semiconductor optical amplifiers as key devices of wavelength converters

Chapter 2 describes three types of polarization insensitive semiconductor optical amplifier (SOA) gates for wavelength division multiplexing (WDM) applications: 1) a low-operating-current SOA gate with a small square bulk active region but without spot-size converters, 2) a multi-channel SOA gate array with tapered waveguide spot-size converters on both sides (SS-SOA), and 3) an SOA with tensile strained multi-quantum well (MQW) active layer. The low operating current SOA gate provides an extremely low current for fiber-to-fiber loss-less operation (5.4-7.0 mA) and a high extinction ratio (> 30 dB) over a wide wavelength range (1530-1580 nm). For hybrid integration to the planar lightwave circuit (PLC) platform, the spot-size converter is indispensable. The design, fabrication, and characteristics of SS-SOA gate array are summarized. A novel technique of estimating the polarization dependence gain (PDG) is proposed. The PDG of an SS-SOA is presented using this measurement technique. Wide polarization independence of tensile-strained MQW-SOA was also demonstrated.

2.1. Semiconductor optical amplifier (SOA)

The important elements for the wavelength converters, which are the key technologies for optical signal processing, are semiconductor optical amplifiers (SOAs) and planar lightwave circuits (PLCs). The following gives the background of SOAs.

2.1.1. SOA gate array

The SOA is expected to be the key component in future photonic networks, because of such superior properties as signal amplification capability, high extinction ratio, and wide wavelength independency. One of the principle functions of the SOA is signal amplification as shown in Fig. 2-1, which requires high gain and high saturation output power with a relatively high injection current.

Another important function is optical gating. The SOA gate can switch off and on the input signal, which requires a high extinction ratio and fast switching time for routing and buffering operations [2.1, 2.2], with a relatively low injection current. So far, electro-absorption (EA) optical gates have been demonstrated [2.3]. The switching time of the EA gate is very fast (several 10 ps), and polarization independence within a wavelength range of 1545 to 1560 nm has been achieved. However, the insertion loss, which is about 7 dB, limits the cascadability of the EA gate. Moreover, the

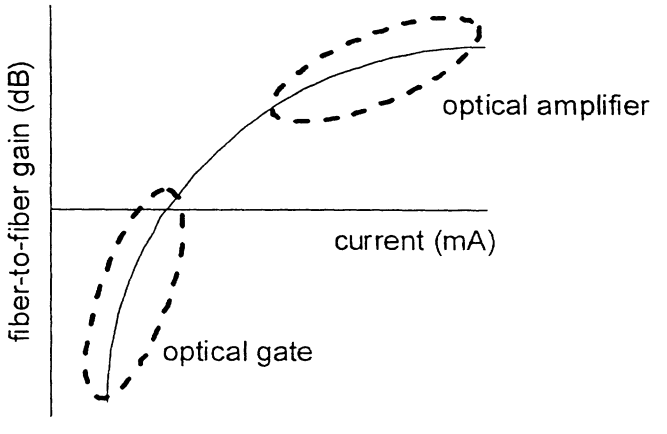

Fig. 2-1 Current versus gain of semiconductor optical amplifier (SOA)

polarization-independent band range is not enough for several applications of wide-range WDM systems [2.4]. SOA is one of the most promising options for gate elements because its provides a fiber-to-fiber lossless operation and a high extinction ratio over a wide wavelength range, 1530 nm to 1600 nm for example.

Many groups have investigated integrating SOA gate arrays into wavelength selector or matrix switches, by means of monolithic- [2.5, 2.6] or hybrid- [2.7, 2.8] integration techniques. The switching time is limited by the carrier lifetime, but is fast enough for several packet switching systems [2.1, 2.2] because a guard time of several ns is usually set between packets.

The most significant problem of the SOA is how to get polarization independence in single pass gain. There are three SOA configurations for achieving polarization independent gain: an SOA whose cross-sectional view of the bulk active layer is almost square (mesa width nearly equal to active layer thickness), an SOA with a tensile-strained bulk active layer, or an SOA with tensile-strained multiple quantum well (MQW) active layer. As mentioned below, we utilized an SOA with square bulk active layer for hybrid integration, and an SOA with tensile-strained bulk active layer for monolithic integration.

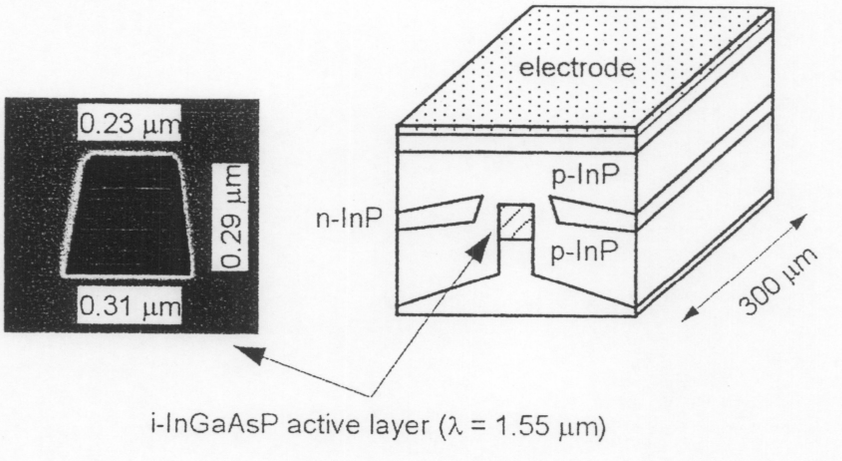

Figure 2-2 SOA with square bulk active layer

2.1.2. SOA with square bulk active layer

The simplest method to achieve polarization independence in single-pass gain is to use a square lattice-matched bulk active region, 0.3-μm thick and 0.3-μm wide for example, as shown in Fig. 2-2, so that the confinement factors of the transverse-electric (TE) and transverse-magnetic (TM) modes become equal. This type of SOA tends to have a relatively low saturation output power, but it has superior characteristics for specific applications, such as wavelength conversion that a strong gain saturation in response to a low input power combined with a short gain recovery time is needed, as shown in Fig. 2-3. For this application, the thick active layer and high confinement factor are more efficient than the thin active region, which is adopted in a SOA with tensile-strained active layer. Furthermore, the high confinement factor achieves an extremely low-power-consuming optical gate for use in packet switching application.

The advantage of the square bulk active region is that the polarization independence in the single pass gain remains stable, even when the injection current or the input signal wavelength is changed. Furthermore, the SOA keeps polarization independence, despite the unintended strain (within 0.05 %) introduced due to the fluctuation of the epitaxial growth or fabrication process. This is because the strain from the slab substrate can be reduced by the opposite strain from the buried structure [2.9, 2.10]. Conventional numerical analysis assumed a slab structure. The uniaxial strain is introduced as shown in Fig. 2-4 (a), where the strains are uniform both parallel to the

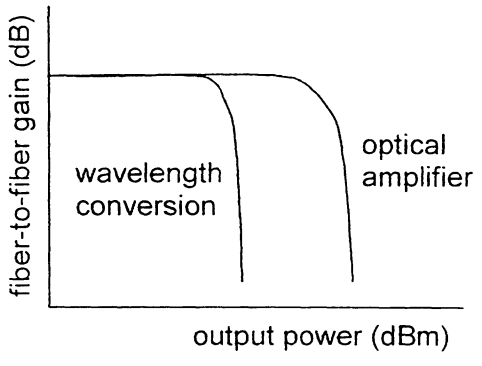

Figure 2-3 Gain saturation characteristics

substrate and growth direction. But in the buried structure, as shown in Figure 2-4 (b), the burying material re-strains the active layer, which results in strain relaxation and low scattering of polarization dependence in single pass gain.

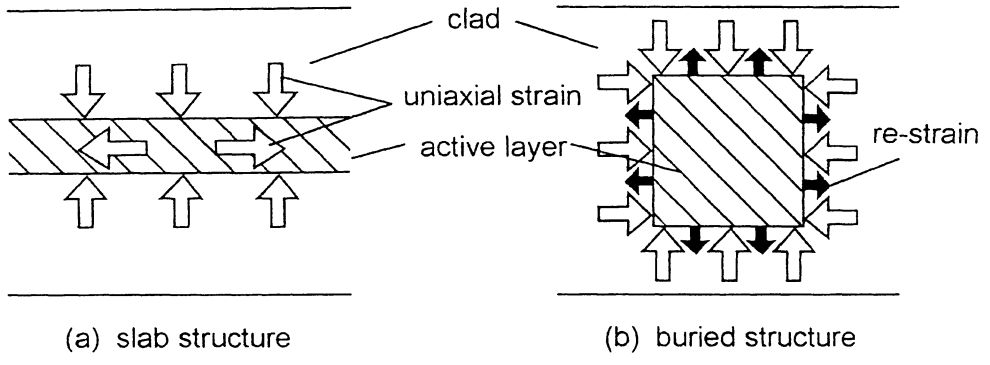

Figure 2-4 Schematic view of strain relaxation

2.1.3. SOA integrated with spot size converters (SS-SOA)

The problem with a square bulk active region is large far field divergence, which causes poor coupling efficiency to optical fiber. This problem is more serious in the case of coupling a multi-channel SOA gate array to a fiber array. Since the SOA is a two-port device which couples to fibers or planar lightwave circuit (PLC) waveguides at both its input and output port, the coupling loss has a larger impact on the loss performance, compared to a single-port device, such as a laser diode (LD). Moreover, the loss degrades the extinction ratio significantly. Large variation in the gain and extinction ratio may arise due to just a slight coupling loss variation, caused by a small misalignment or the variation of the gap between the SOA and fibers/PLC waveguides. To solve these problems, Doussiere et al. proposed a lateral taper at the end of the square active region, which reduces the far field divergence and improves both the coupling efficiency and misalignment tolerance [2.11]. Leclerc et al. presented a 4-channel SOA gate array module using the Si V-groove flip-chip technique for fiber

coupling [2.12]. At NTT, vertically tapered waveguides are used as spot-size converters, as shown in Fig. 2-5.

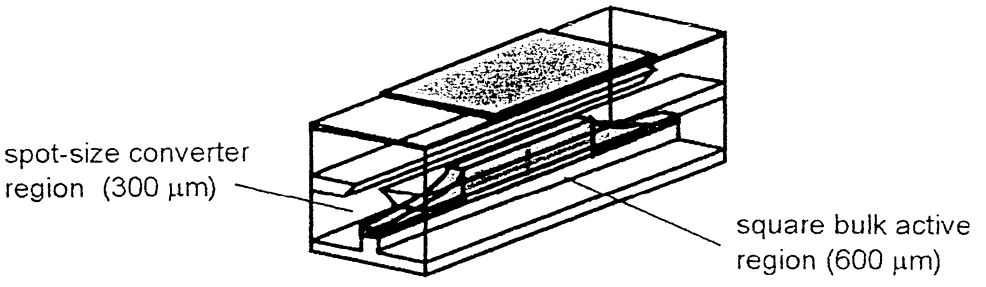

Figure 2-5 SOA integrated with spot-size converters

2.1.4. SOA with tensile strained active region

Precise control of the strain introduced in the active layer enables polarization independence, as shown in Fig. 2-6. So far, SOA structures based on a tensile-strained MQW active region have been constructed by controlling the strain value in both wells and barriers, carefully adjusting the wells and barriers thickness, and optimizing the

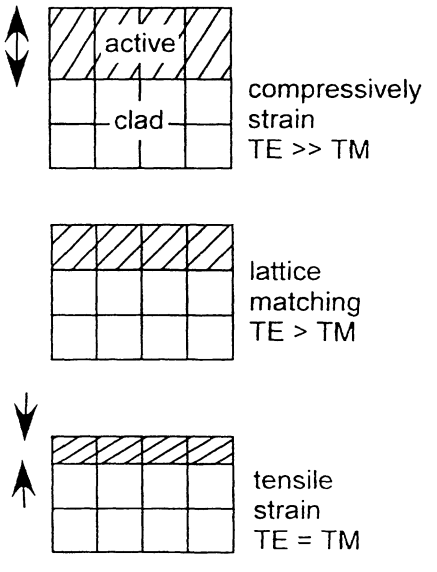

Figure 2-6 SOA with strained active layer

number of wells [2.13, 2.14]. The advantages of the tensile-strained MQW active layer structure are saturation output power superior to that of square bulk active layer structures and large fabrication tolerance because of the wide stripe width. Moreover, with this wide stripe width, it is easy to integrate the SOA with a passive semiconductor waveguide having a typical stripe width of 1.5 μm [2.15]. However, the weak point of the tensile-strained MQW active layer structure is wavelength dependence. Godefroy et al. reported a MQW-SOA that has polarization dependence over a limited wavelength range of 1520-1535 nm, but this is not enough for practical use [2.16].

Another method for polarization independence is to utilize a slightly (0.1-0.15 %) tensile-strained bulk active layer [2.17]. This structure, with its easy growth control and relatively thick active layer, provides a high confinement factor that is an advantage for wavelength conversion, and has a wide stripe width suitable for monolithic integration.

2.2. Low-operating-current SOA gate (SOA without spot-size converters)

2.2.1. Design and structure

SOA is a key element for the future photonic subsystems. Notice that one important requirement is not a "amplifier device" with high gain, high saturation output power and relatively high operating current, but is a "gate device" with low saturation output power and low power consumption. Therefore, an SOA with square bulk active layer structure, which has a large optical confinement factor, may be the best choice.

Figure 2-7 shows the structure of the polarization-independent SOA gate with a low operating current. The optical signal from a lens fiber is coupled to a facet of the active region. The active layer is a 0.29-μm thick InGaAsP bulk layer with a band-gap wavelength of 1.55 μm. The narrow sub-μm stripe provides an almost square form to achieve polarization insensitivity. The device length is 300-μm. Both facets are anti-reflection (AR) coated.

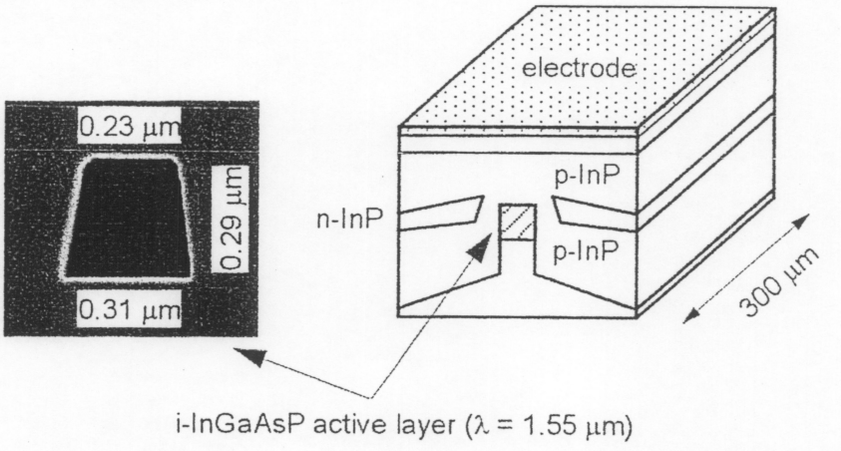

Figure 2-7 SOA with square bulk active layer

Figure 2-8 shows the polarization dependence gain (PDG) as a function of stripe width. The PDG is the gain difference between the TE and TM mode. The PDG was calculated using a semi-vectorial finite elemental method for two structures, one having a 0.3- and the other a 0.4–μm thick active layer. The TE mode gain was assumed to be 10 dB. The PDG is zero, when the stripe width is equal to the thickness. This

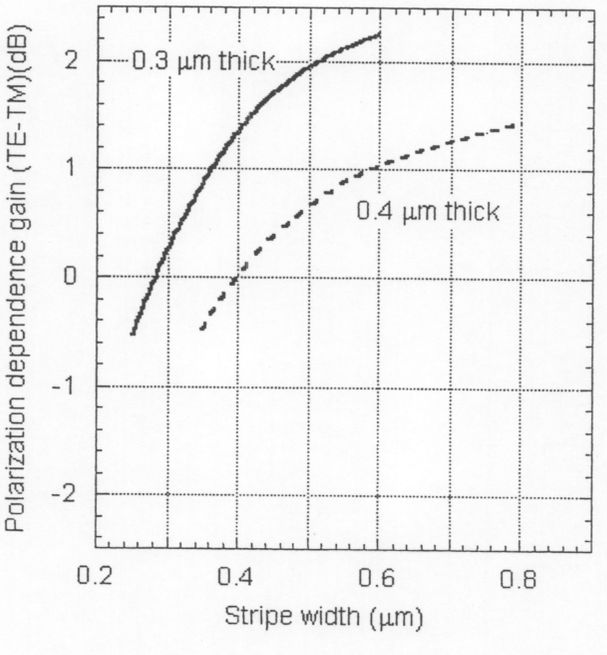

Figure 2-8 Design of the active region

indicates that the polarization independence is achieved with a square active layer. As the stripe width becomes larger than the active layer thickness, the TE mode gain increases more than the TM mode gain. This is because the confinement factor for the TE mode becomes larger than that of the TM mode. If a small polarization sensitivity of ± 0.5 dB is permitted, the fabrication tolerance will be ± 0.05 μm.

The SOA gates were fabricated using a full 2-inch wafer process. The mesa structure was formed using CH_4/H_2 dry-etching and was buried with *p*- and *n*-InP using a buffer-inserted buried hetero-structure (BIBH) method [2.18]. The mesa stripe is 0.23-μm (top) to 0.31-μm (bottom) wide, and with this small and almost square active region, a low operating current as well as polarization insensitivity is achieved. Another SOA gate with a 0.4-μm-thick-and-0.4-μm-wide active region was also fabricated.

2.2.2. Setup and measurement

Figure 2-9 shows the setup for the gain measurement of a low-operation-current SOA gate chip. Gating characteristics were measured using a polarization exchanger and polarization-maintaining dispersion-shift fibers with tapered lens facets. The polarization extinction ratio of the measurement setup was more than 20 dB throughout a wide-band range of 1530-1600 nm. The polarization exchanger could switch the linear polarization of the signal light (TE to TM, and TM to TE) within 0.5 s. The fiber-to-fiber gain for TE and TM signal was estimated. The measurement limit of the polarization dependence gain (PDG) was 0.2 dB, which included the polarization dependence of the measurement setup, the effect of the gain ripple of the SOA gate, and

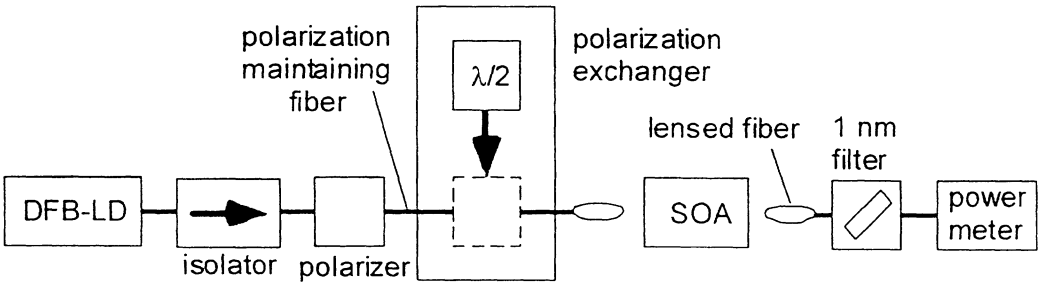

Figure 2-9 Experimental setup for gain measurement

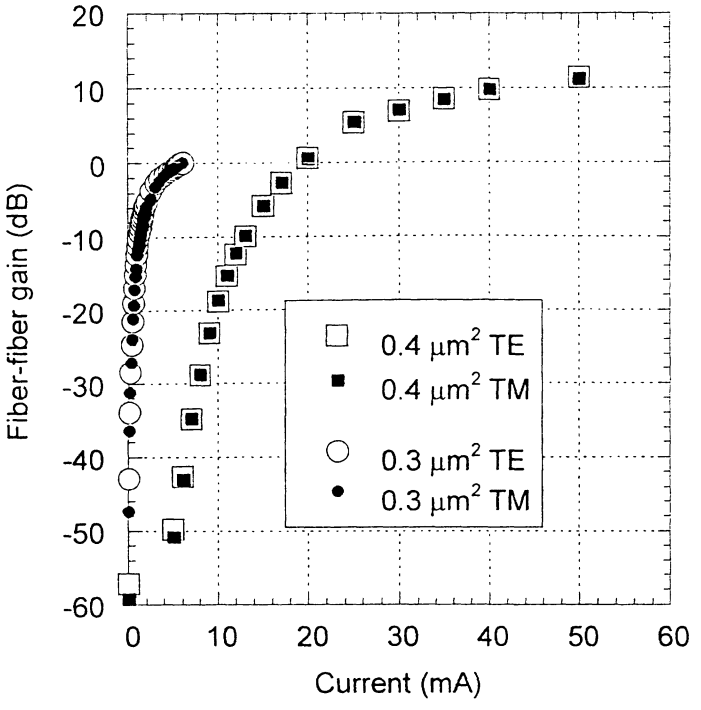

Figure 2-10 Gain characteristics

the fiber-coupling misalignment during the measurement.

Figure 2-10 shows the SOA gate gain characteristics for a continuous wave (CW) optical input of –10 dBm at 1553 nm. The circles correspond to an SOA with a 0.3 (thick) x 0.3 (width)-μm active layer. Loss-less gating for an input power of less than –5 dBm was obtained at an extremely low current of 6.0 mA. The extinction ratio of the SOA gate was more than 40 dB for an input power lower than –10 dBm and 33 dB for a –5 dBm input. The reduction of the extinction ratio is due to the saturation of the optical loss. The PDG at the loss-less operating current was less than 0.2 dB, which was the measurement limit. These results show that the very narrow mesa structure of 0.3-μm was successfully formed within the fabrication tolerance of 0.05 μm. The squares correspond to a 0.4(t) x 0.4(w)-μm active layer. A loss-less operating current of 20 mA and polarization independence were achieved. The fiber-to-fiber gain was 12 dB at 50 mA and was larger than that of the 0.3(t) x 0.3(w)-μm active layer. This may be because the confinement factor of the 0.4(t) x 0.4(w)-μm active layer is as large as 37%, while that of the 0.3(t) x 0.3(w)-μm one is 12%.

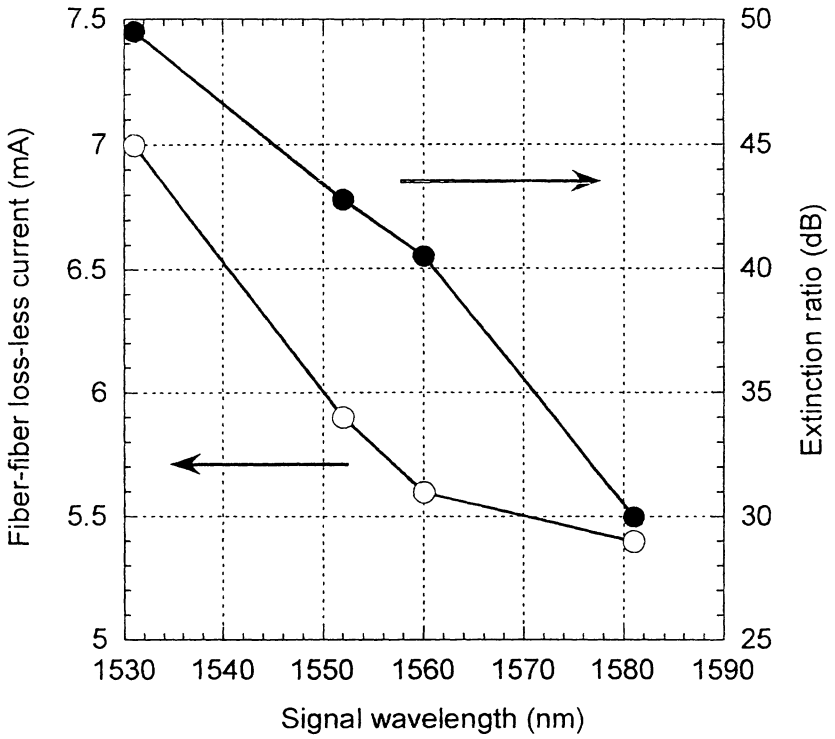

Figure 2-11 Wavelength dependence of loss-less current and extinction ratio

The loss-less current and the extinction ratio change with the wavelength of the input signal. This wavelength characteristic of the SOA gate with a 0.3(t) x 0.3(w)-μm active layer is shown in Fig. 2-11. The minimum loss-less current is as low as 5.4 mA at a wavelength of 1580 nm, which is the gain peak of the SOA gate. This is the lowest record, as the lowest reported loss-less current had been 25 mA [2.19]. Although the loss-less current increases with shorter input, low operating current of less than 7.0 mA was obtained over 1530-1580 nm. The maximum extinction ratio was 50 dB at 1530 nm. The extinction ratio decrease with longer wavelength input because of the saturation of the optical loss, but a high extinction ratio of more than 30 dB was obtained over a wide-band of 1530-1580 nm. These results indicate that the SOA gate is very useful for use in wide band WDM systems.

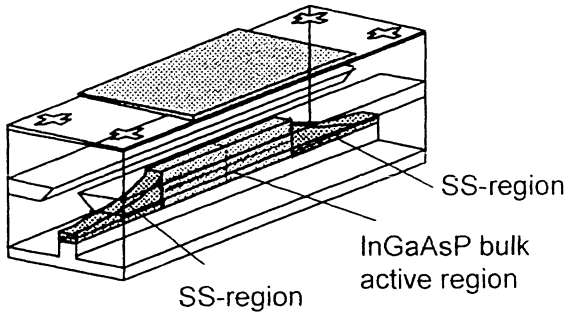

Figure 2-12 Structure of SS-SOA with straight facets

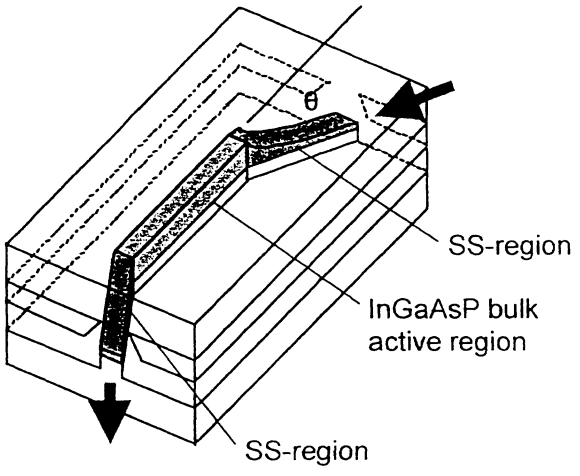

Figure 2-13 Structure of SS-SOA with angled facets

2.3. SS-SOA gate array

2.3.1. Design for polarization independence

Figures 2-12 and 2-13 show the structure of an SS-SOA gate with straight and angled facets, respectively. Both SS-SOA gates consist of 600-μm bulk active layer (band-gap wavelength = 1.55-μm) and two 300-μm vertically tapered bulk passive regions (band-gap wavelength = 1.3-μm at the facet) [2.20]. To get higher fiber-to-fiber gain, the thickness of the active region is set to 0.4 μm. The thickness of the spot-size converter layer gradually changes from 0.4 μm at the butt-joint interface to 0.2 μm at the facet. The basic type with a straight spot-size converter region was fabricated to

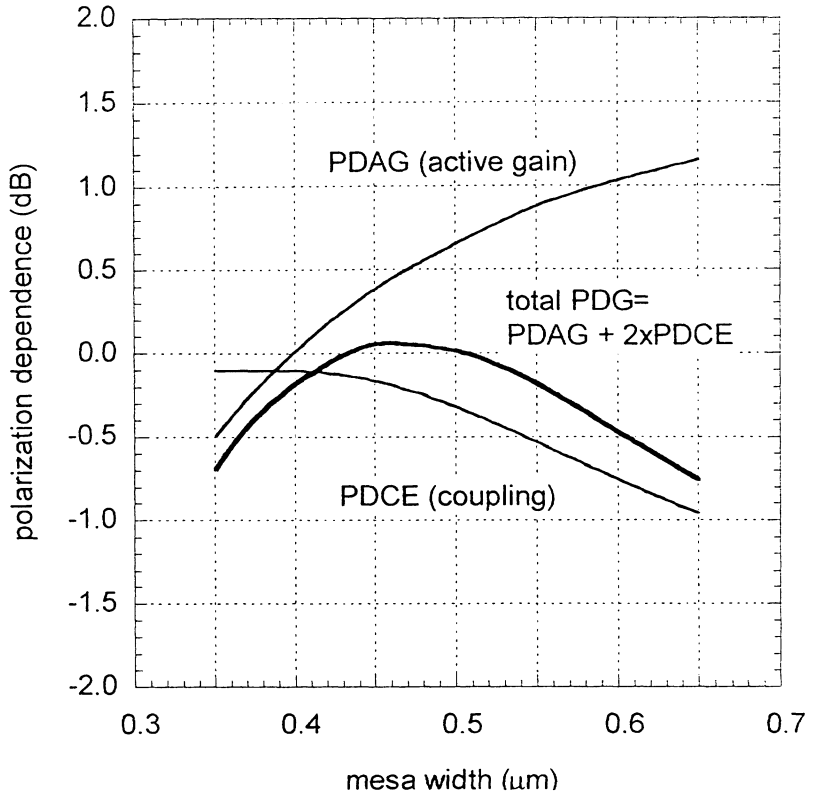

Figure 2-14 Calculated polarization dependence

confirm the basic characteristics (such as polarization dependence gain), and an angled type having a 7-degree angled-facet SS was fabricated to have low reflectivity at the facet, high gain, and low gain ripple for commercial use.

The polarization dependence gain (PDG) of an SS-SOA is the sum of polarization dependence of the active region gain (PDAG) and the polarization dependence of the coupling efficiency (PDCE) at the both facets. Since we have adopted a butt-joint structure in which the SS-SOA is divided into the active region and passive SS region, we can consider that the polarization dependence of the active region gain (PDAG) is only due to deviation from the square shape of the active layer, and the polarization dependence of the coupling efficiency (PDCE) is due to the shape of the tapered guiding layer in the spot-size converter region. It should be noted that the SS-SOA has proven to be polarization independent even if an undesired strain is introduced during the epitaxial growth or fabrication process, because the buried

structure reduces the strain in the square active layer [2.21]. Figure 2-14 shows the mesa width dependence of the total polarization dependence gain (PDG), the polarization dependence of the active region gain (PDAG) and the polarization dependence of the coupling efficiency (PDCE), calculated by the 2-D finite element method [2.22]. The spot size of the coupled PLC (or fiber) was assumed to be 4.0 μm. As for the polarization dependence of the active region gain (PDAG), the perfectly square active layer (mesa width 0.4 μm) provides a polarization insensitive gain. As the mesa width is increased, the gain of the TE mode becomes larger than that of the TM mode. On the other hand, the coupling efficiency of the TE mode decreases as the mesa becomes wider. This is because the optical confinement of the TM mode becomes smaller than that of the TE mode at the facet of the spot-size converter region. This tendency is enhanced when the mesa becomes wider. Consequently, the spot size of the TM mode expands more efficiently than that of the TE mode, which leads to the difference in the coupling efficiency. Fortunately, since the mesa width dependence of the polarization dependence of the active region gain (PDAG) and the polarization dependence of the coupling efficiency (PDCE) is of opposite polarity, the total polarization dependence gain (PDG) becomes smaller. Assuming that an acceptable PDG is within 0.5 dB, the fabrication tolerance of the mesa width ranges from 0.36 to 0.54 μm, which is wide enough to control it using photolithography and the dry-etching technique.

2.3.2. Fabrication process of a SS-SOA

The SS-SOA was fabricated, as shown in Fig. 2-15, using 2-inch wafer processes. A 0.4-μm thick bulk-active layer was grown on an *n-InP* substrate using metal organic vapor phase epitaxy (MOVPE). The island of the active region was formed by dry- and wet-etching techniques. The vertical guiding SS region was butt jointed to the active layer using selective area growth [2.23]. The mesa was formed using an *i*-line photolithographic stepper. A high contrast *i*-line positive photoresist was used to achieve good verticality at sub-micrometer patterning, consisting of 0.3-μm dimensional fidelity. The 0.5-μm wide mesa stripe was formed by CH_4/H_2 dry-etching,

which provides verticality of the mesa stripe. The etched mesa structure was buried with the buffer-inserted buried hetero-structure (BIBH) method and the upper electrode was formed at the active region. Finally, both facets were coated with antireflection (AR) films [2-24].

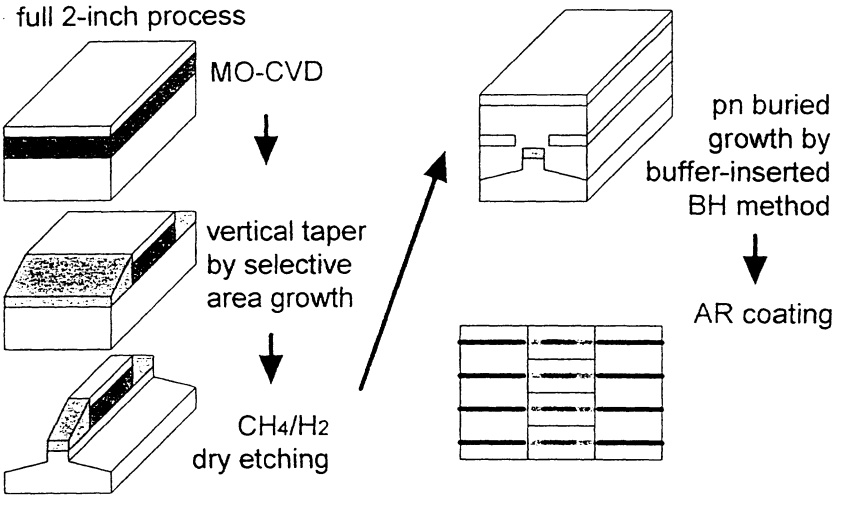

Figure 2-15 Fabrication of a SS-SOA

2.3.3. Uniformity of fabrication

The structure uniformity was checked to ensure reproducibility of the straight facet SS-SOA. Figure 2-16 shows a histogram of mesa width distribution, which indicates that the mesa width is within 0.05 μm of the design value. This results in the polarization dependence gain (PDG) increase of less than 0.5 dB and the coupling loss increase of less than 0.5 dB. Figure 2-17 show a histogram of the distribution of the spot size converter thickness at the facet. The thickness is fabricated to 0.03 μm of the design size, which ensures a coupling loss increase of less than 0.5 dB. The uniformity of the threshold current was first checked using as-cleaved samples. Figure 2-18 shows the threshold current distribution over a 2-inch wafer. The averaged threshold current was 19.8 mA, and the standard deviation was 1.0 mA. Even with a very narrow stripe, these results indicate that the SS-SOA was well fabricated with good uniformity.

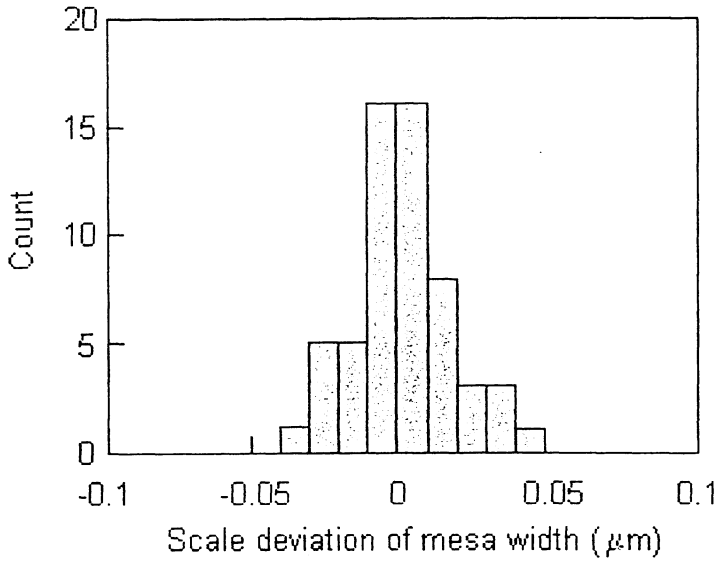

Figure 2-16 Scale deviation of mesa width

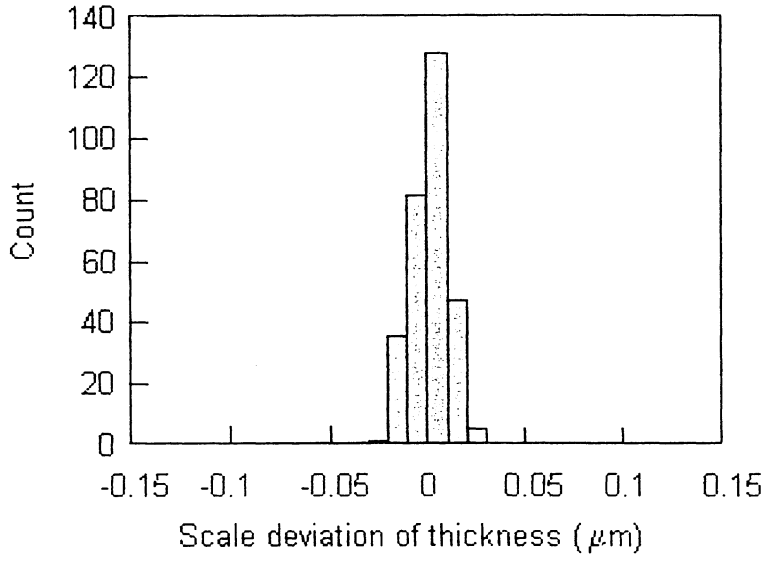

Figure 2-17 Scale deviation of the thickness

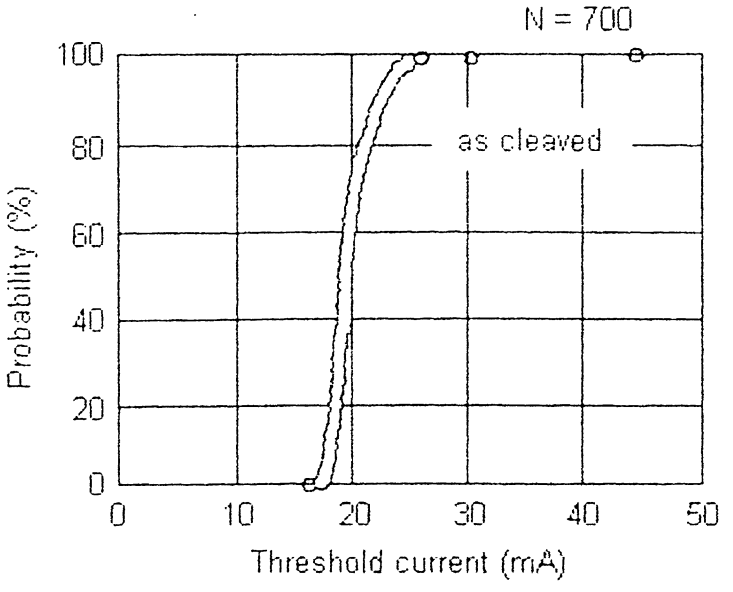

Figure 2-18 Probability of threshold current

2.3.4. Characteristics of straight-facet SS-SOA

After AR coating, the gain and polarization characteristics of the SS-SOA were evaluated using flat-end dispersion- shifted fibers with a spot-size of 4.0 μm. The fibers were butt-coupled to the facet of the straight facet SS-SOA. Figure 2-19 shows the fiber-to-fiber gain and polarization dependence gain (PDG) characteristics versus injection current. The wavelength of the input light is 1550 nm at an input power of −10 dBm. Fiber-to-fiber loss-less current is 28 mA, and fiber-to-fiber gain is 10 dB at 40 mA. The PDG is less than 0.2 dB, which is the measurement limit, independent of injection current. The extinction ratio, defined as the difference in the optical power between at the loss-less current and at 0-mA, is greater than 35 dB. Figure 2-20 shows the PDG versus wavelength, which is less than 0.2 dB.

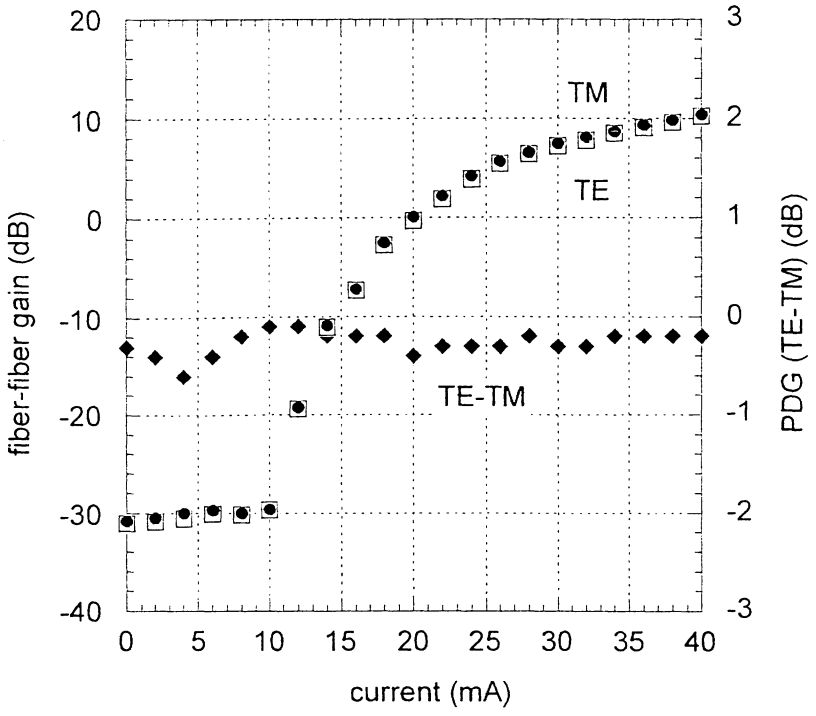

Figure 2-19 Gain characteristics

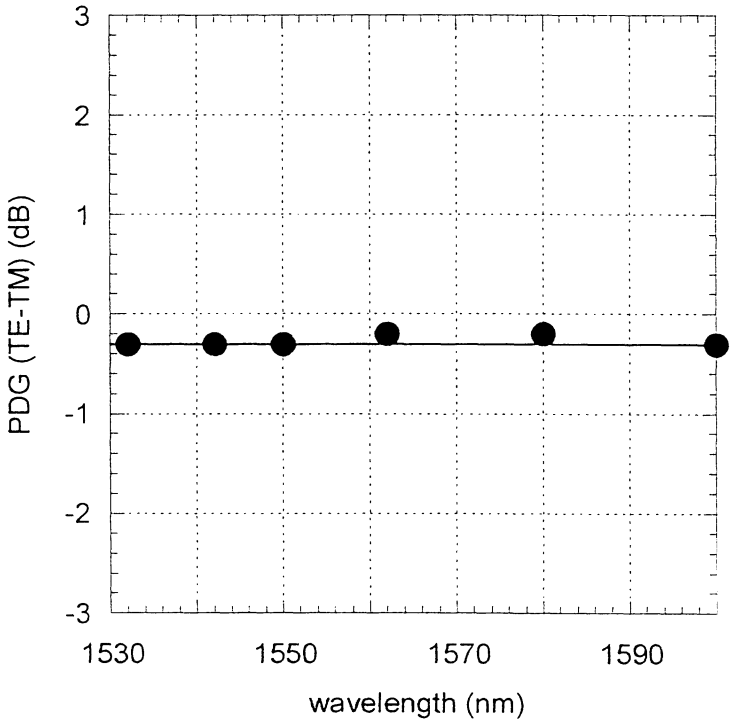

Figure 2-20 PDG versus wavelength

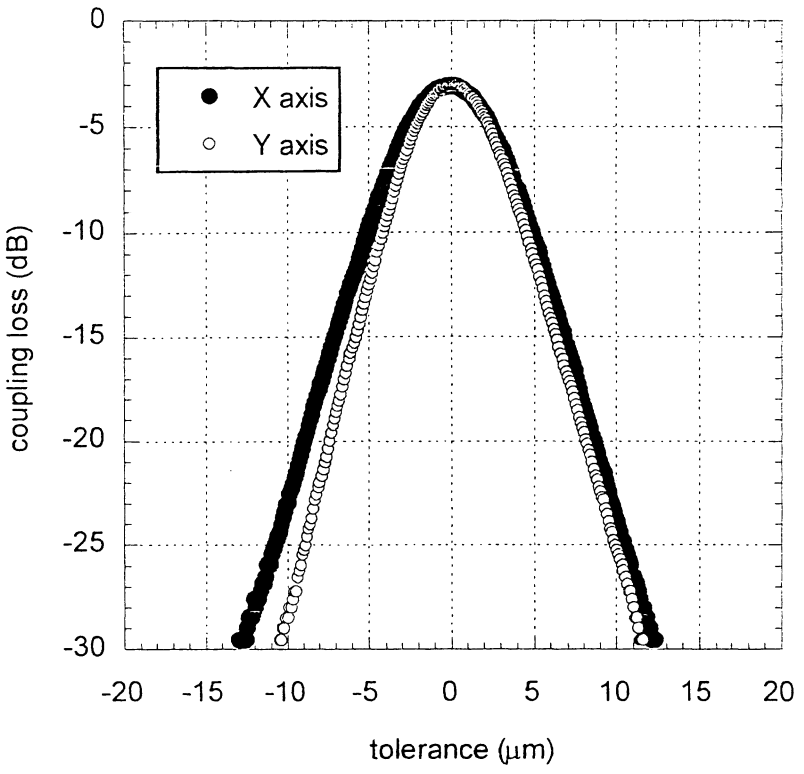

Figure 2-21 X- and Y-axis tolerance of the coupling loss

Figure 2-21 shows the tolerance of the coupling loss between an SS-SOA and an optical fiber, versus the offset. The typical coupling loss was 2.6 dB. A 1-dB increase in coupling loss corresponds to alignment tolerances of 2.1-μm (horizontal: X-axis) and 1.9-μm (vertical: Y-axis). The alignment tolerance of the optical (Z)-axis direction was 12.0-μm. These large tolerances mean the SS-SOA is suitable for hybrid PLC module using passive alignment.

2.3.5. Characteristics of angled-facet SS-SOA

Figure 2-22 shows the fiber-to-fiber gain and polarization dependence gain (PDG) characteristics versus injection current of an angled-facet SS-SOA after AR coating, with a DFB-LD of a wavelength of 1550.0 nm at an input power of –20 dBm. Fiber-to-fiber loss-less current is 40 mA, and fiber-to-fiber gain is 20 dB at 150 mA. The fiber-to-fiber gain is higher than that of the straight-facet SS-SOA, because the

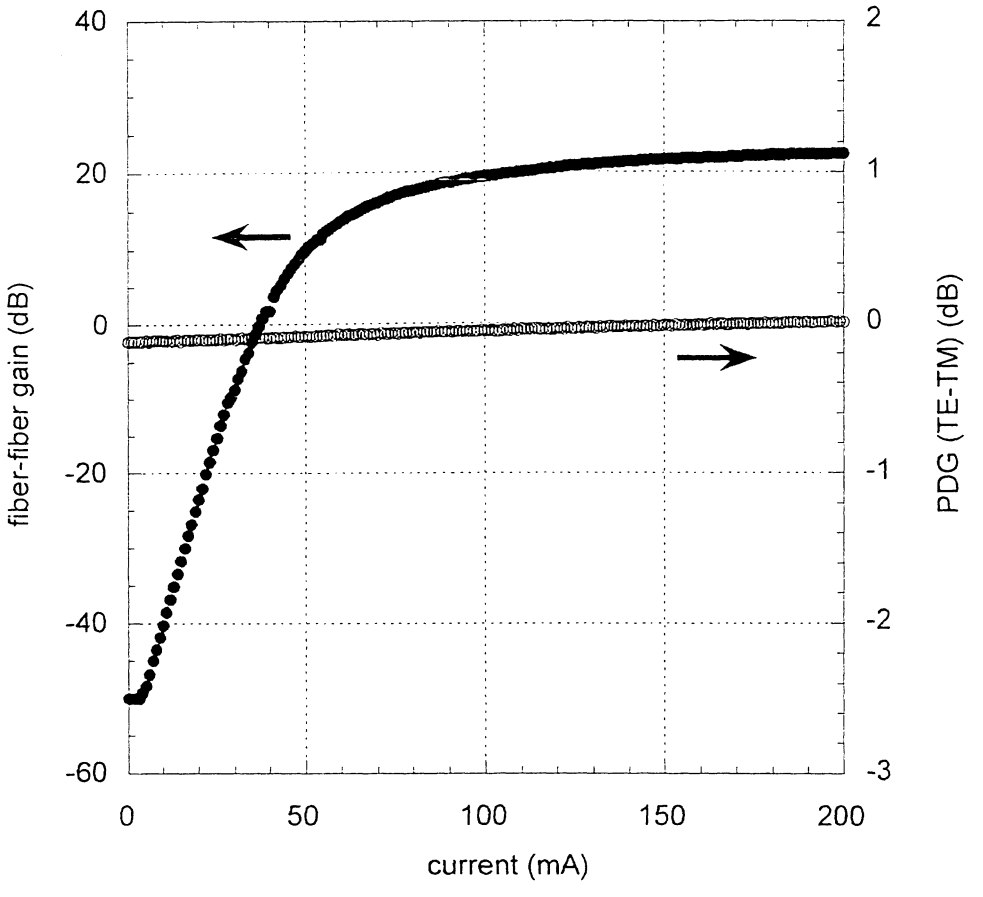

Figure 2-22 Gain characteristics of angled-facet SS-SOA

carrier density of the angled-facet SS-SOA is higher than the straight-facet SS-SOA due to the low reflectivity at the facet. The PDG is less than 0.2 dB, which is the measurement limit, independent of injection current. The extinction ratio, defined as the difference in the optical power between at the loss-less current and at 0 mA, is greater than 50 dB. The extinction ratio is larger than that of the straight-facet SS-SOA, because the un-coupled input light from the input fiber does not couple to the output fiber. Figure 2-23 shows the PDG versus wavelength, which is less than 0.2 dB. The gain ripple of the SS-SOA is less than 0.5 dB. The coupling efficiency is 2.5 to 3 dB. These results indicate that the angled-facet SS-SOA is useful for optical gate with high-gain and large extinction ratio.

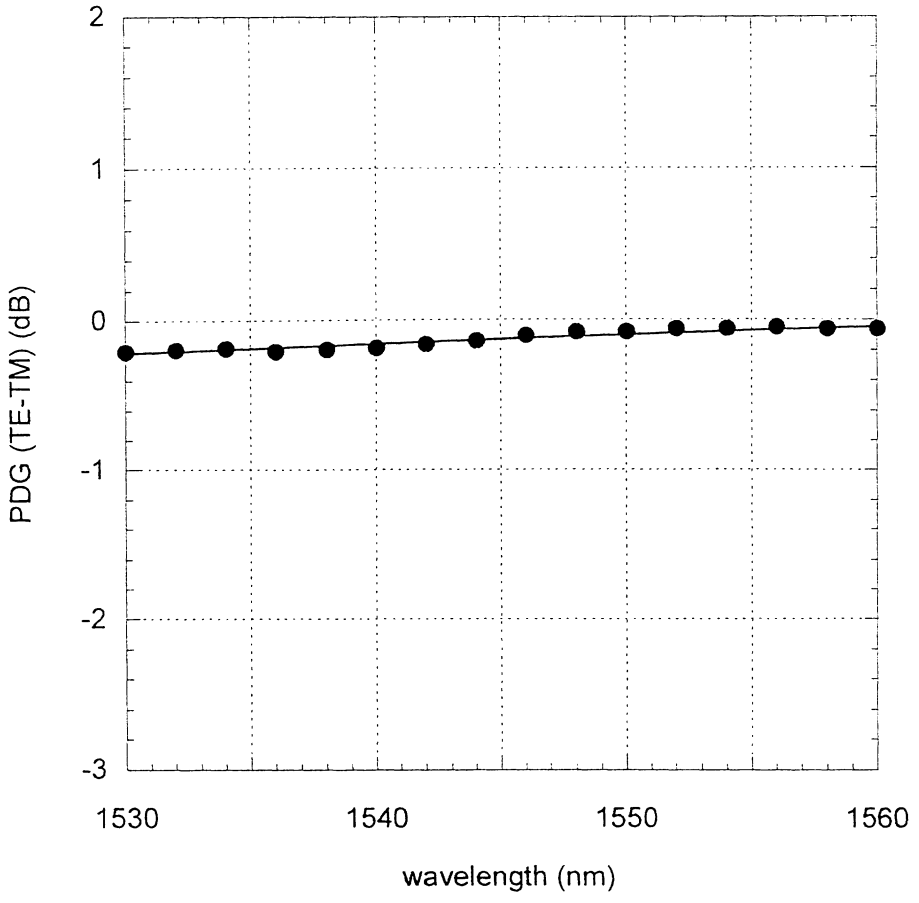

Figure 2-23 Wavelength dependence of PDG

2.3.6. Details of polarization estimation

(1). Theory for evaluating total polarization dependence

Our aim is to measure the polarization dependence gain (PDG) of a SS-SOA with a certain gain ripple, such as found in an angled-facet SS-SOA without AR coating. By averaging the signal gain over a wide wavelength range, the PDG can be accurately estimated with low reflection of gain ripples. Using this method, the PDG of the angled-facet SS-SOA can be estimated before AR coating. Therefore, the evaluation cost, which is one of the most serious problems of SS-SOA, can be reduced.

Assuming residual reflectivities R_1 and R_2 at both facets, we express the signal

gain G due to a Fabry-Perot resonator as

$$G(\varphi) = \frac{(1-R_1)(1-R_2)G_s}{(1-\sqrt{R_1R_2}G_S)^2 + 4\sqrt{R_1R_2}G_s \sin^2(\varphi)}, \qquad (\varphi = 2\pi nL/\lambda) \qquad (1)$$

where G_s is the single pass gain (equal to signal gain G at R_1=R_2=0), φ the phase of the gain ripples, L the cavity length, n the refractive index, and λ the signal wavelength [2.25].

To know the potentiality of G_s, when the SS-SOA has no gain ripples, we introduce the signal gain averaged over the wavelength range, G_{av}, such that

$$G_{av} = \frac{\int_0^{2m\pi} d\varphi G(\varphi)}{\int_0^{2m\pi} d\varphi} = \frac{(1-R_1)(1-R_2)G_s}{2m\pi\left[1-(\sqrt{R_1R_2}G_s)^2\right]} \tan^{-1}\left(\frac{1+\sqrt{R_1R_2}G_s}{1-\sqrt{R_1R_2}G_s} \cdot \tan 2m\pi\right), \qquad (2)$$

where m is the ratio of the averaging bandwidth to a gain ripple period, which is about

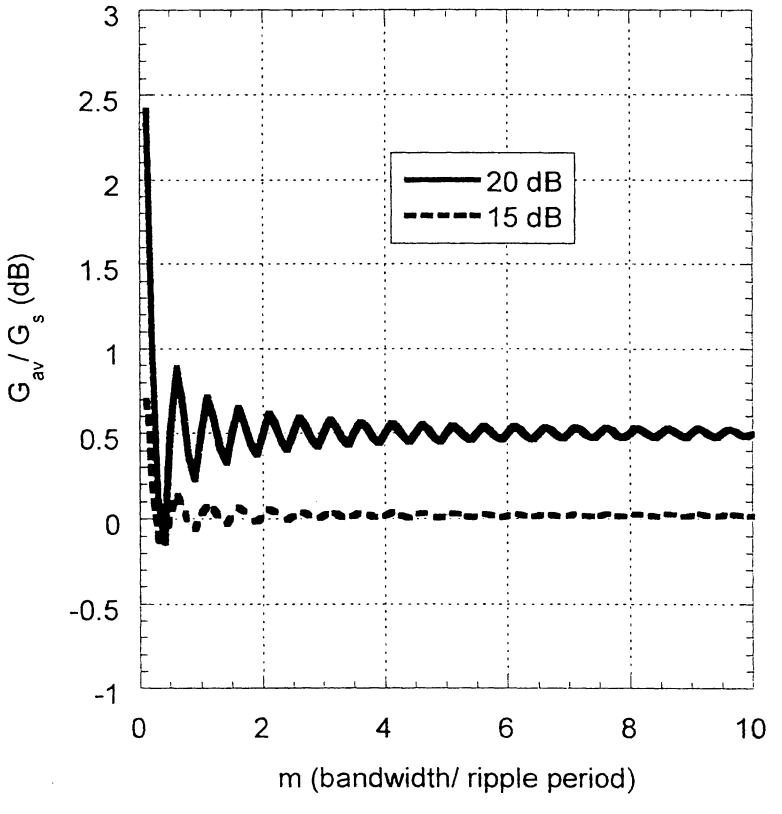

Figure 2-24 Fluctuation of G_{av} against m

0.25 nm for the 1200-μm-long SS-SOA. Figure 2-24 shows the fluctuation of G_{av} against m when G_s=20 dB or 15 dB at $R1$=$R2$=-24.7 dB. The fluctuation seems to be negligible when m>6. Note that if R_1, R_2 << 1 and $\sqrt{R_1 R_2} G_s$<<1, G_{av} becomes close to G_s. Therefore, we can know G_s with some accuracy by measuring G_{av}. The accuracy is good enough at 0.5 dB even when G_s=20 dB.

Then we looked at the deviation between G_{av} and G_s. When we simply set R_1=R_2=R and assume m as a integer, the ratio of G_{av} and G_s, Q, is

$$Q = \frac{G_{av}}{G_s} = \frac{(1-R)^2}{1-(RG_s)^2} \quad . \tag{3}$$

Figure 2-25 shows the relation between R and G_s under the condition that the accuracy of Q=0.50 dB is the solid line (curve A) and Q=-0.50 dB is the broken line (curve B). If

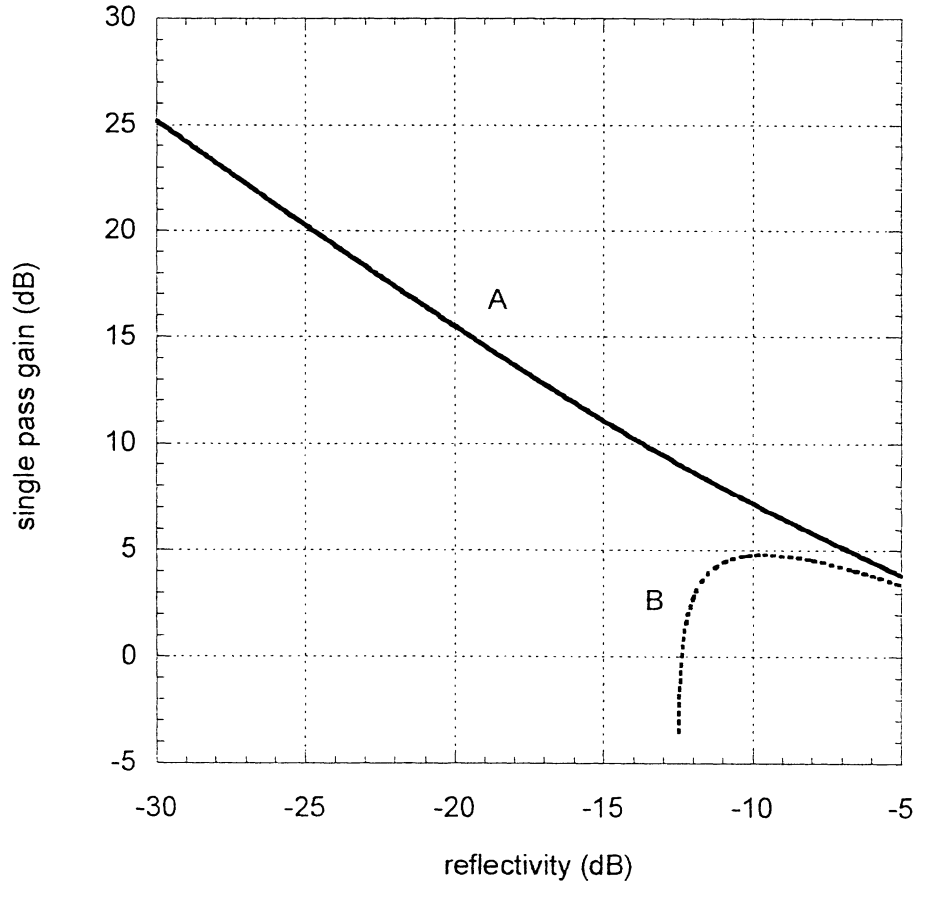

Figure 2-25 Relation between reflectivity and single pass gain

G_s and R satisfy the condition within the range of the two curves, we can measure G_{av} with a small difference, within 0.50 dB from G_s. As R becomes smaller, the range of G_s becomes wider. Curve A is almost linear, because RG_s is nearly constant in the small-R region. Curve B has a threshold of $(1\text{-}R)^2$ for the small-G_s region, and is also linear above the threshold. Figure 2-26 shows the relation between R and ripple V at the upper limit of G_s under the condition of the accuracy Q=0.50 dB (curve A) and Q=-0.50 dB (curve B), which satisfy the equation

$$V = ((1 + RG_s)/(1 - RG_s))^2 . \quad (4)$$

If R=-24.7 dB (0.34 %, which is the reflectivity that may be achieved in an angled-facet SS-SOA without AR coating [2.26]), V and Gs are permitted to be about 6.0 and 20 dB, respectively. Even if the reflectivity is as bad as R=-19.5 dB, V=6.5 dB and Gs=15 dB

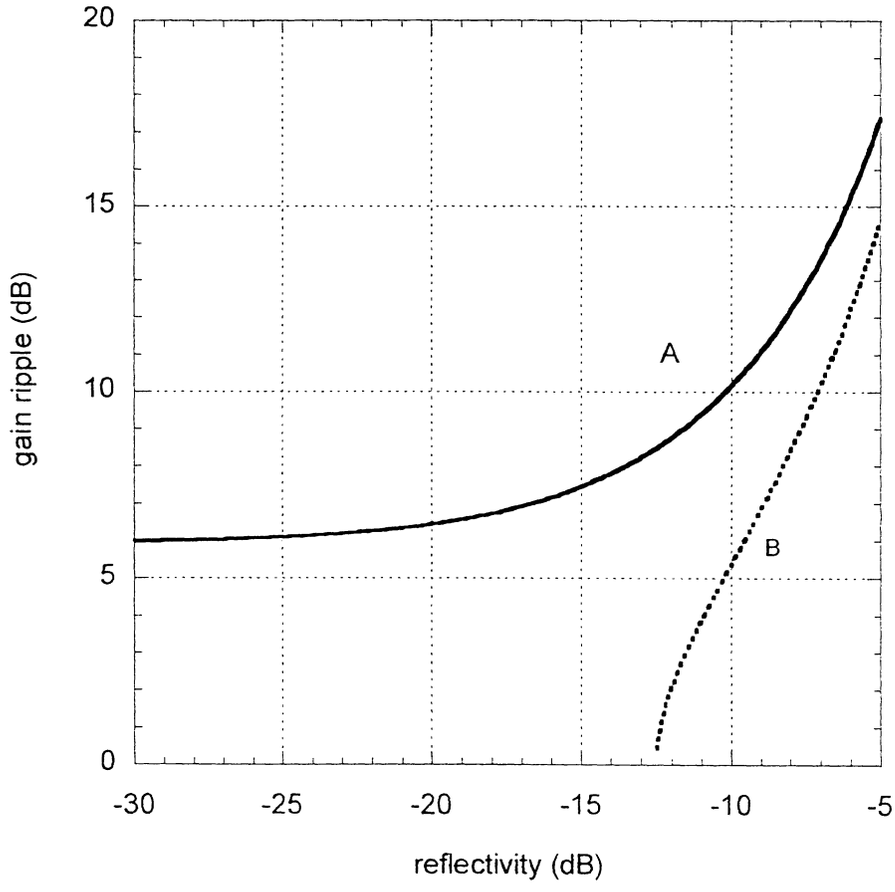

Figure 2-26 Relation between reflectivity and gain ripple

are allowed. Therefore, we can obtain the PDG from the difference by measuring G_{av} instead of G_s for TE and TM modes:

$$PDG = G_{av}(TE \bmod e) - G_{av}(TM \bmod e) . \quad (5)$$

Accordingly, the PDG also has accuracy within an error of less than 0.5 dB under the condition of $R << 1$ and $RG_s << 1$, even when the gain ripples reach about 6.0 dB.

(2). Evaluate total polarization dependence using the EDF-ASE method

The gain ripple of an angled-facet SS-SOA without AR coating is shown in Figure 2-27, which indicate that the maximum gain-ripple is lower than 6 dB when the injection current is lower than 73 mA. Therefore, the PDG with a current of less than 73 mA can be evaluated without AR coating. According to Fig. 2-22, the chip gain G_s at 73 mA is about 20 dB, assuming a coupling efficiency of 2.5-3 dB.

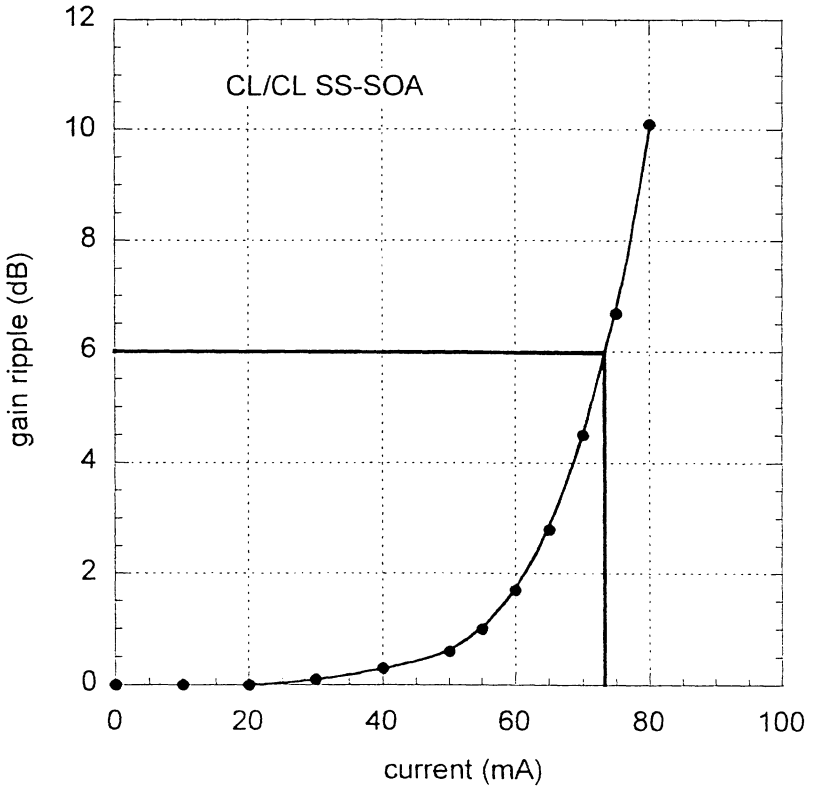

Figure 2-27 Gain ripple of an angled-facet SS-SOA

The experimental setup for measuring the averaged gain to determine PDG is shown in Fig. 2-28. The wide band amplified spontaneous emission (ASE) from a polarization maintaining Er-doped fiber (EDF) was coupled to an angled-facet SS-SOA through an optical filter and polarization exchanger. By using the polarization maintaining EDF-ASE, an input signal of a linear TE polarized light was selected. The bandwidth of the optical filter was set at 7 nm, which is more than 25 times larger than the gain ripple period in the SS-SOA This means m in eq. (2) is larger than 25, which is enough even if the power level of the gain ripple fluctuates because of multiple resonances. The center wavelength was 1550 nm. The polarization state was maintained by using polarization maintaining fibers, and the polarization of the injection signal, TE or TM, was switched by the polarization exchanger. The polarization extinction ratio was maintained at up to 20 dB. The input power was –20 dBm

Figure 2-29 shows the results of the PDG measurement of a SS-SOA without AR coating, using the ASE of Er-doped fiber (●) and conventional DFB laser source of a wavelength of 1550.0 nm (×). With the DFB, the PDG varied from –1.4 to 1.5 dB at the current of 45 to 73 mA, because of the gain ripple of the SS-SOA without AR coating. On the other hand, when the ASE of Er-doped fiber was used, the measured G_{av} of the TE and TM light seemed to be averaged [according to eq. (2)], and PDG was obtained by eq. (5). The PDG in the ASE method was less than 0.2 dB and did not vary with the driving current less than 73 mA. These results agree well with the measurement for an angled SS-SOA with AR coating using a DFB-LD, as shown in Fig. 2-22.

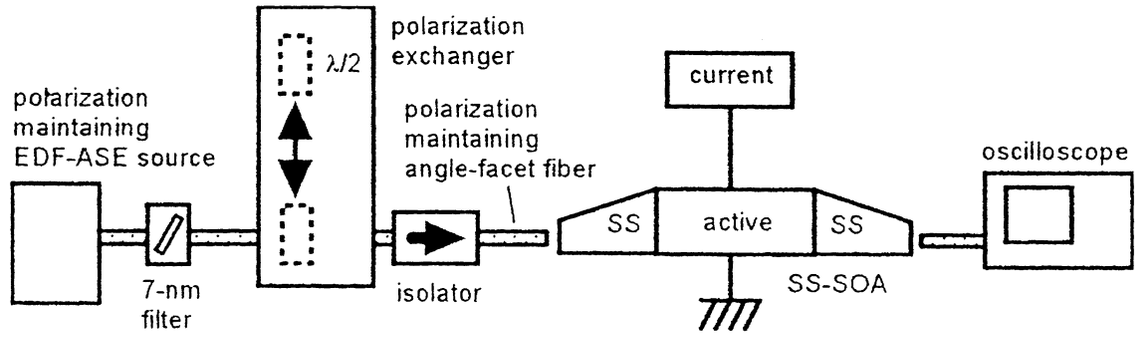

Figure 2-28 Experimental setup for PDG estimation

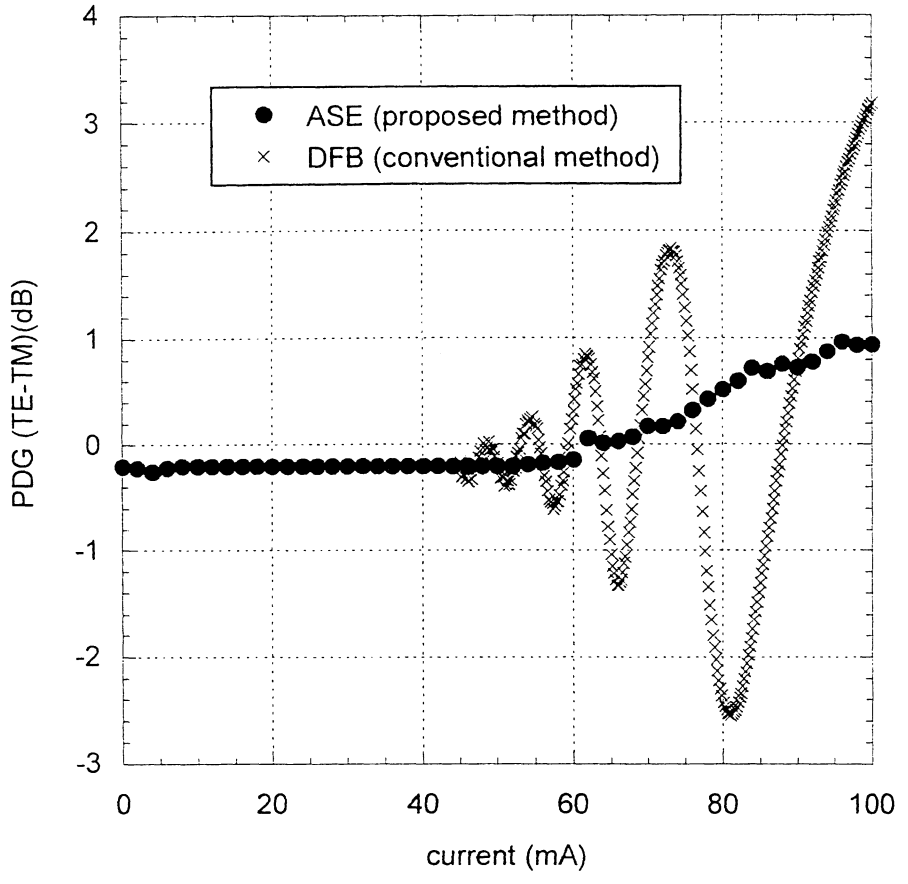

Figure 2-29 Estimation of PDG using ASE source

Figure 2-30 shows the measured PDG against the mesa width of a straight SS-SOA with AR coating that has a gain ripple of 3 dB. With the ASE method, the evaluation results are in good agreement with the simulation (Fig. 2-14), and we can conclusively state that the ASE method is a very effective way to ascertain the PDG in a SS-SOA.

(3). Polarization dependence in coupling efficiency

Figure 2-31 shows the experimental setup for evaluating the polarization dependence in coupling efficiency (PDCE), which clarifies the factors of PDG. An input signal from a DFB-LD with a wavelength of 1.51 μm was launched into a SS-SOA through a polarization exchanger. A minus bias of –1 V was applied to the SS-SOA, and

the photo-current of the SS-SOA was measured. As the active region of the SS-SOA is long enough (600 μm), the SS-SOA perfectly absorbs the input signal. The absorption loss is more than 40 dB for both TE and TM input. Therefore, the TE/TM mode difference of the photo current is equal to the power input to the active layer, that is

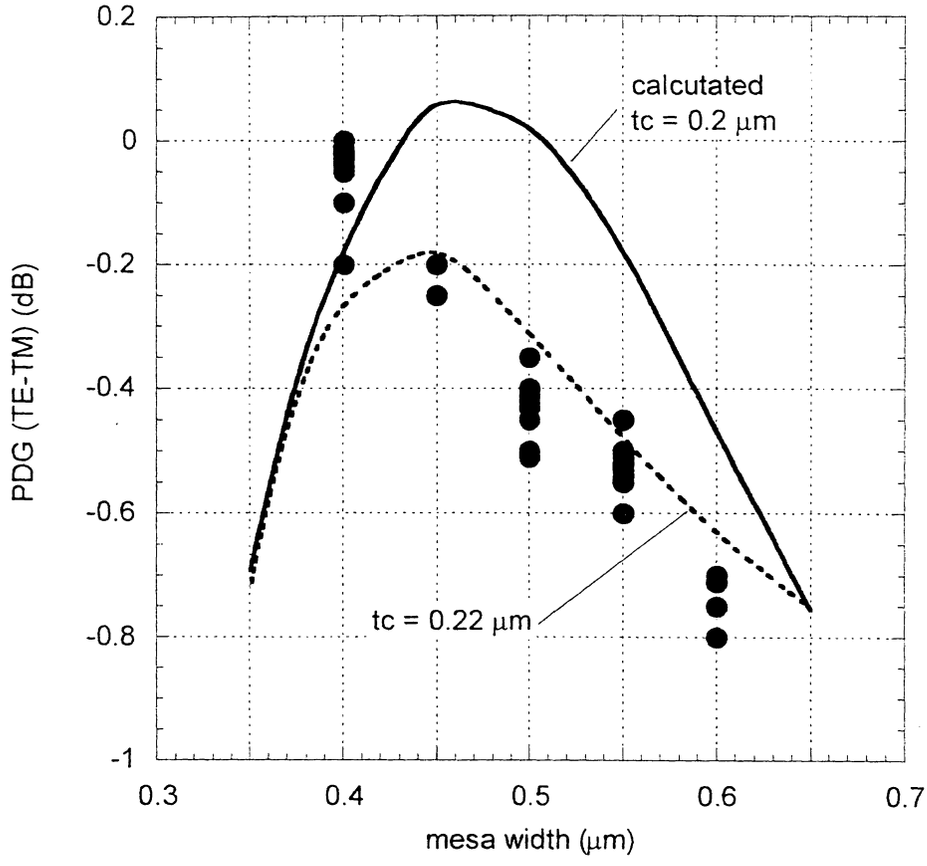

Figure 2-30 PDG versus mesa width

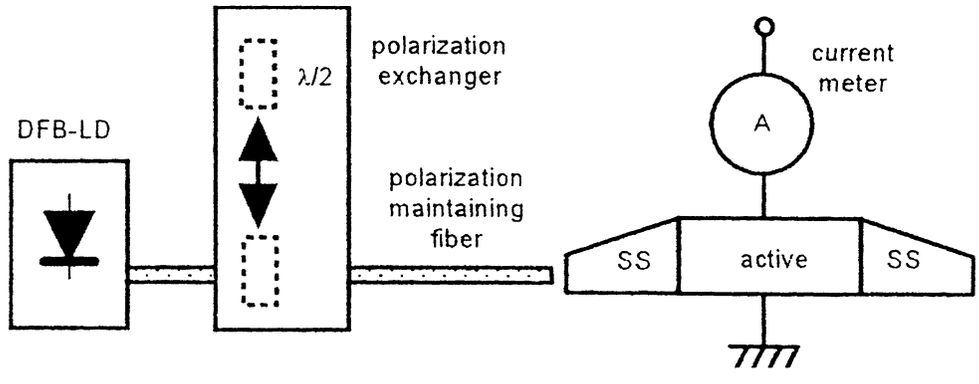

Figure 2-31 Experimental setup for estimating polarization dependence in coupling efficiency (PDCE)

polarization dependence in coupling efficiency (PDCE) including the SS loss. Figure 2-32 shows the measured polarization dependence in coupling efficiency (PDCE) against the mesa width, which is in a good agreement with the simulations (Fig. 2-14). Therefore, this technique is effective for separating the polarization dependence in coupling efficiency (PDCE) and in active gain (PDAG), which is very beneficial in SS-SOA design and fabrication.

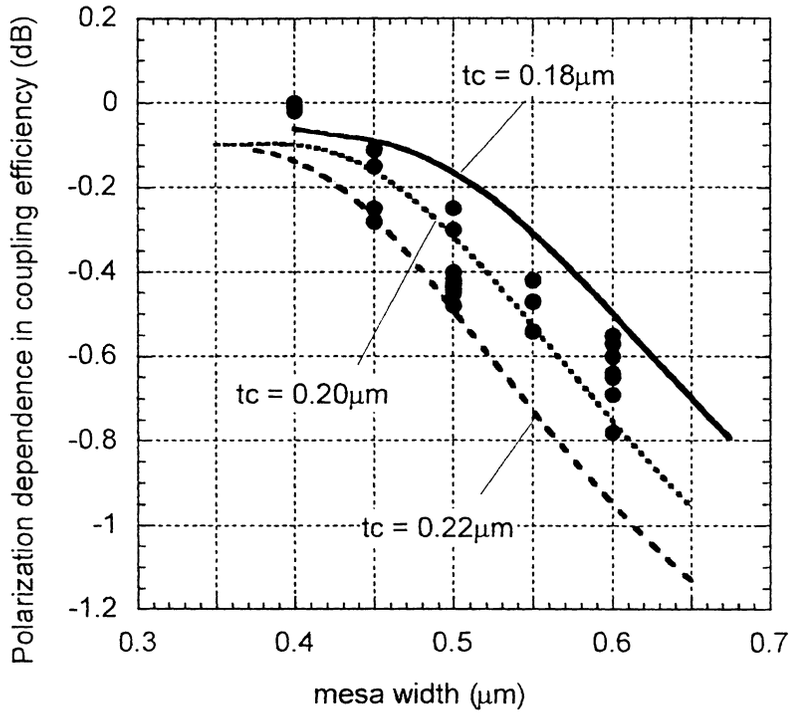

Figure 2-32 Polarization dependence in coupling efficiency (PDCE) versus mesa width

2.3.7. Relaxation of strain in the buried active region

One of the most serious problems of commercial SOAs is how to confirm polarization independence. Usually the epitaxial growth, such as MOVPE, may introduce an undesired strain of less than 0.05% to the wafer, which results in a deviation of polarization dependence gain (PDG). The fabrication process also may

introduce an undesired strain. To evaluate the influence of the undesired strain, we measured the PDG of SOAs with a slightly strained active layer. Three types of SOAs (without spot-size converter) with a strain of –0.09%, +0.02%, and +0.08% were fabricated using a specially controlled MOVPE growth method. Each active region was 0.4-μm wide and 0.4-μm thick. The cavity length was 600-μm. After AR coating, the PDG at a chip gain of 10 dB was measured using tapered fiber. The optical power of the input signal was –10 dBm with a wavelength of 1550 nm.

Figure 2-33 shows the PDG of a slightly strained square bulk SOA. The deviation of PDG is less than 1 dB. As the run-to-run undesired strain of the epitaxial growth can be controlled to be less than +/-0.05%, the influence of the strain on the PDG is less than 0.5 dB. This value is small enough compared to the SOA with wide active region such as tensile-bulk or tensile-MQW active layer, which is about 2.0-2.5 dB/0.05% [2.27, 2.28]. This may be because of the relaxation of strain in the square active layer, as described at session 2.1.2. Figure 2-34 shows the relaxation of strain versus the aspect ratio, mesa width divided by the thickness, of the active layer [2.10]. A

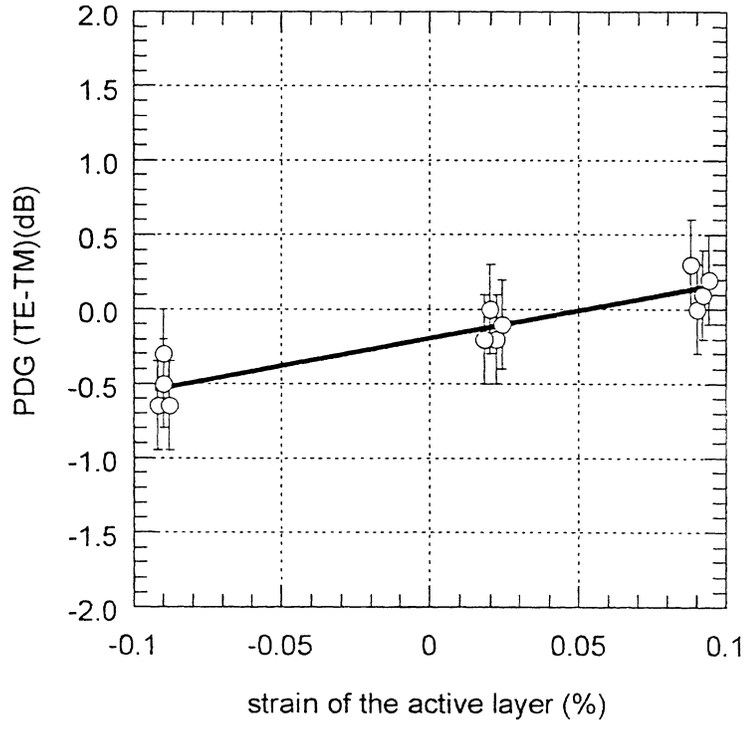

Figure 2-33 PDG versus gain

prefect square, with an aspect ratio of 1, reduces the stain to one-fifth compared to an active region with a wide aspect ratio.

As mentioned above, the advantage of square bulk active region is the stability of polarization independence, even the injection current or the input signal wavelength is changed. Furthermore, the square active region maintains polarization independence even though an unwilling strain (within 0.05 %) is introduced during the epitaxial growth or fabrication process.

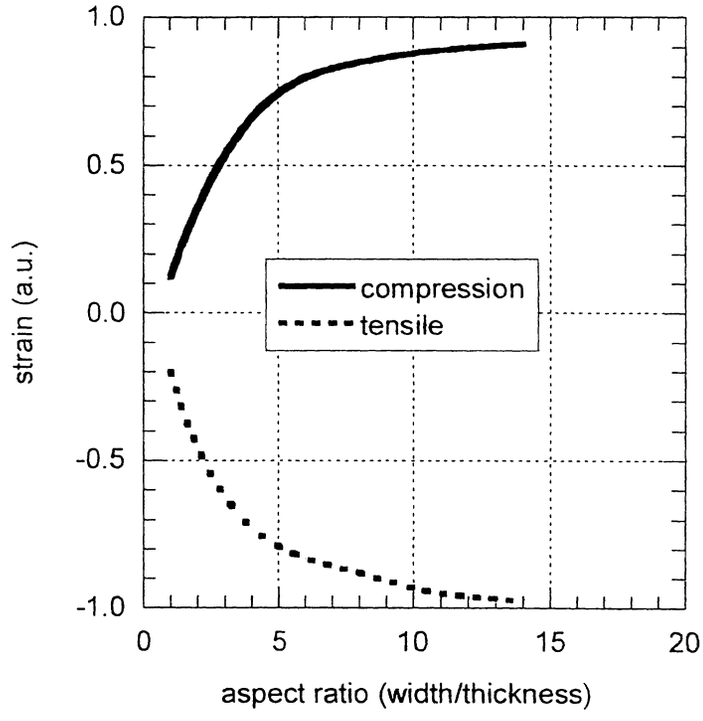

Figure 2-34 Relaxation of strain

2.3.8. Details in switching characteristics

The switching time of the straight facets SS-SOA was improved using a speed-up condenser, located beside the terminal resistor of 45 ohm, as shown in Fig. 2-35. The turn-on current was 40 mA. Both the 10%-to- 90 % rise-time *Tr* and the fall-time *Tf* were 0.5 ns with a condenser larger than 30 ps, as shown in Fig. 2-36. The sum of the delay time *Td* and *Tr* versus the bias current was also evaluated. The *Td* is

large influenced by the bias current. As the bias current becomes larger, both the *Td* and the extinction ratio become smaller. As shown in Fig. 2-37, the *Td* + *Tr* is less than 2 ns when the bias current is 8 to 10 mA. On the other hand, the on/off ratio is expected to be more than 40 dB with a bias current of less than 10 mA. Figure 2-38 shows the gated eye patterns with 10-Gbit/s input signal at the driving condition of a bias current of 8 mA and turn-on current of 40 mA.

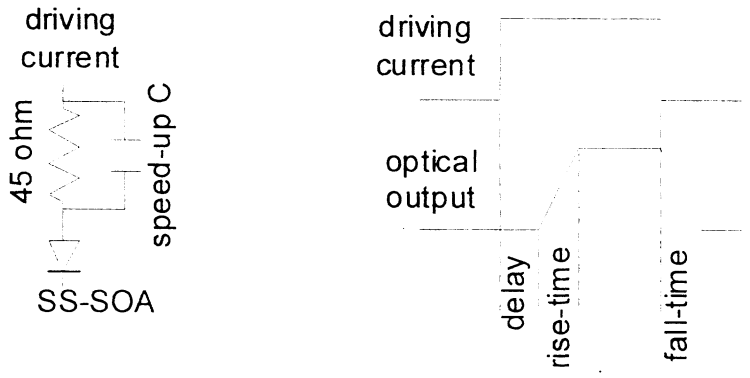

Figure 2-35 Driving circuit and input/output waveform

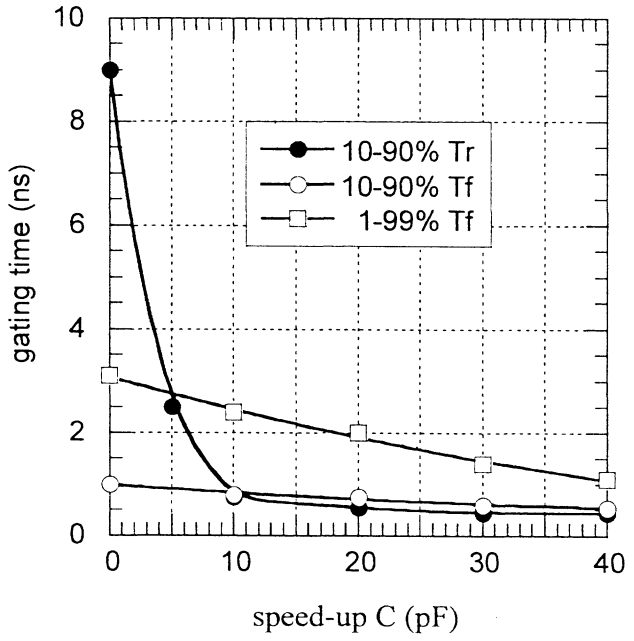

Figure 2-36 Gating time versus speed-up condenser

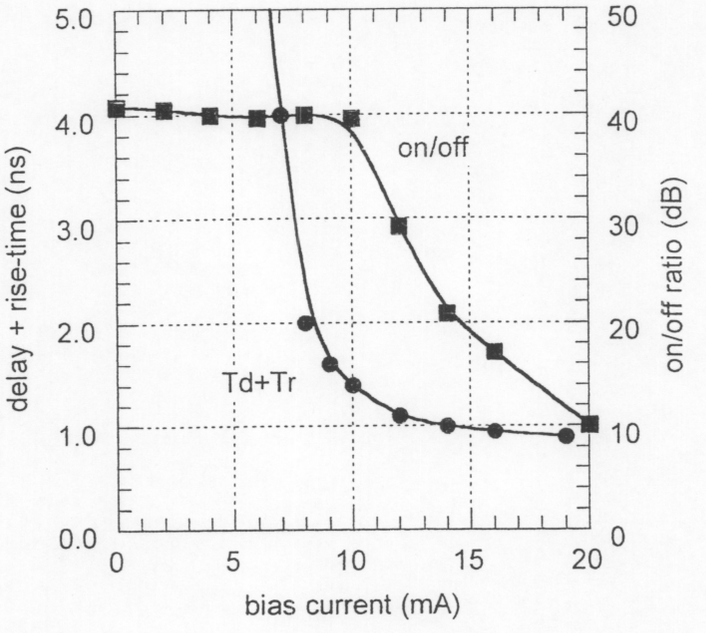

Figure 2-37 Switching characteristics versus bias current

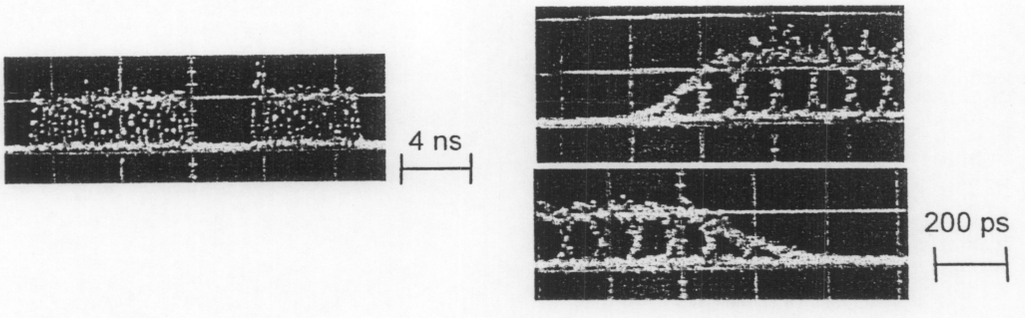

Figure 2-38 Gating eye patterns

2.4. Tensile-strained MQW-SOA

2.4.1. Abstract of MQW-SOA

The SOA gate with a tensile-strained multi-quantum well (MQW-SOA) as the active layer [2.14, 2.29] has recently been studied. The advantages of the MQW-SOA gate are wide stripe width, large fabrication tolerance, and large fiber-to-fiber gain. Godefroy et al. reported a polarization-independent SOA gate that can operate over a limited wavelength range of 1520-1535 nm, which is not enough for practical use.

Our aim for the high-performance tensile-strained MQW-SOA gate was to control the peak wavelength of the amplified spontaneous emission (ASE) to be 1520 nm at the loss-less operating current in order to achieve polarization independence for a signal wavelength between 1530 and 1580 nm. The fabricated MQW-SOA has very low polarization dependence of 0.3 dB, which remains unchanged over a driving current ranging between 30 and 60 mA, input signal wavelength ranging between 1530 and 1580 nm, and a mesa stripe width ranging between 1.0 and 1.75 μm.

2.4.2. Device structure and measurement setup

SOAs with a 1-μm n-cladding layer and a 5-period tensile-strained InGaAs(13 nm)/InGaAsP(20 nm) MQW layer were grown on n-InP substrates by means of metal organic molecular beam epitaxy (MOMBE) [2.30]. The InGaAs strains were -0.47, -0.54, -0.61, or -0.68%. Mesa stripe widths of 1.0, 1.25, 1.50, and 1.75 μm were formed by CH_4/H_2 dry-etching. The MQWs with the mesa stripe were buried by the buffer inserted buried heterostructure (BIBH) method using metal organic vapor phase epitaxy (MOVPE). The device length was 600 μm. The facets were coated with antireflective (AR) coating. The peak wavelength of the ASE was set to a relatively short wavelength of 1520 nm at 40 mA. The ASE output power difference between the TE and TM modes has a large current dependence near the gain peak of 1520 nm, but a relatively small dependence for a longer wavelength between 1530 and 1580 nm. Therefore,

polarization independent fiber-to-fiber-gain can be expected throughout the wide fiber amplifier range of 1530-1580 nm.

Gating characteristics were measured using lensed polarization-maintaining dispersion-shift fibers and a polarization controller. Optical coupling loss between the lensed fiber and the SOA gate was 5 dB/facet. The polarization extinction ratio of the measurement setup was >20 dB over the entire fiber amplifier gain band (1530-1580 nm). The polarization controller could switch the linear polarization of signal light (TE to TM, TM to TE) within 0.5 s. The measurement limit of the polarization dependence was 0.2 dB, which includes the polarization dependence loss (PDL) of the measurement setup, the effect of the gain ripple, and the fiber-coupling misalignment during the measurement.

2.4.3. Experimental results

Figure 2-39 shows the polarization dependence gain (PDG) at the fiber-to-fiber loss-less current versus the InGaAs strain of the active layer. The input signal was -10 dBm at 1553 nm. The PDG decreases with decreasing strain. A very low PDG of 0.3 dB is achieved at a strain of -0.47%. This figure also shows that the PDG is very sensitive to InGaAs strain, i.e., 2dB/0.1%). Therefore, the strain value in MQW growth must be precisely controlled.

In the following, we describe the various characteristics of the -0.47% strained sample. Figure 2-40 shows the mesa width dependences of the fiber-to-fiber loss-less current, extinction ratio, and PDG. No change could be observed for an extinction ratio of 50 dB and a PDG of 0.3 dB for a wide range to of active layer width (1.0 to 1.75 μm). The loss-less current slightly increased from 30 to 40 mA. These results indicate that the mesa width tolerance is more than 10 times greater than that of bulk SOA. Figure 2-41 shows the gain characteristics of the 1.75-μm wide SOA gate for an optical input of 1553 nm. Fiber-to-fiber loss-less gating is obtained at a current of 40 mA. The polarization dependence gain at the loss-less operation current is 0.3 dB. It is worth noting that this value did not change when the driving current was varied from 23 to

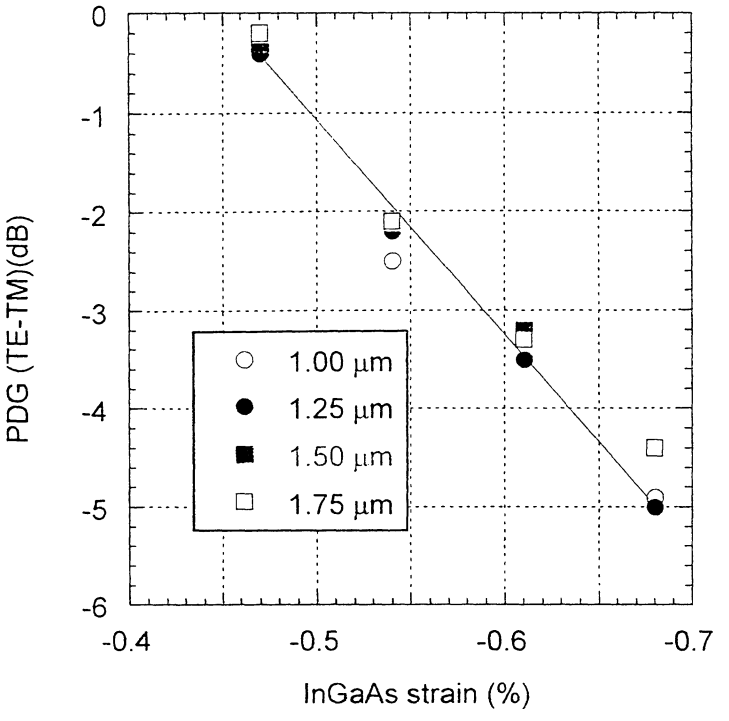

Figure 2-39 PDG versus strain

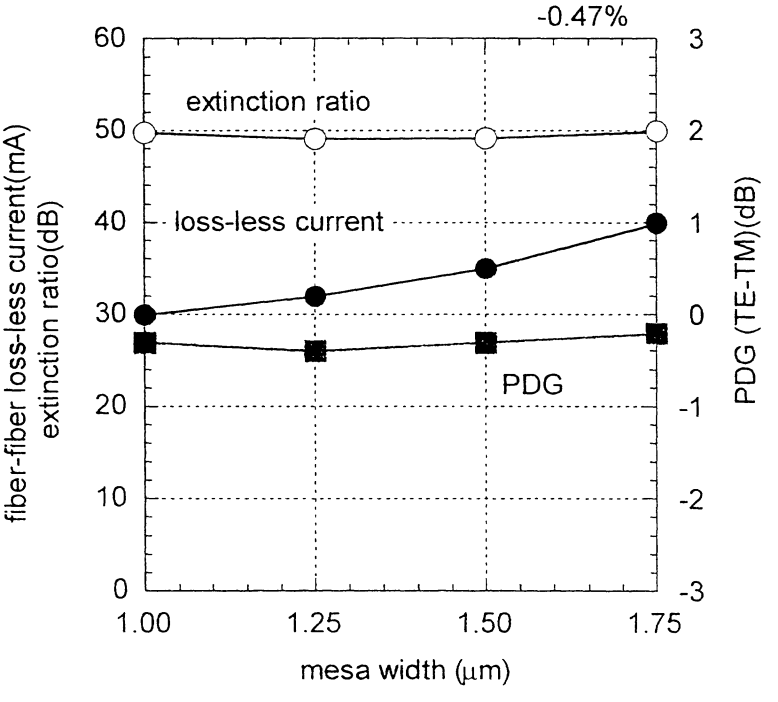

Figure 2-40 Mesa width dependences

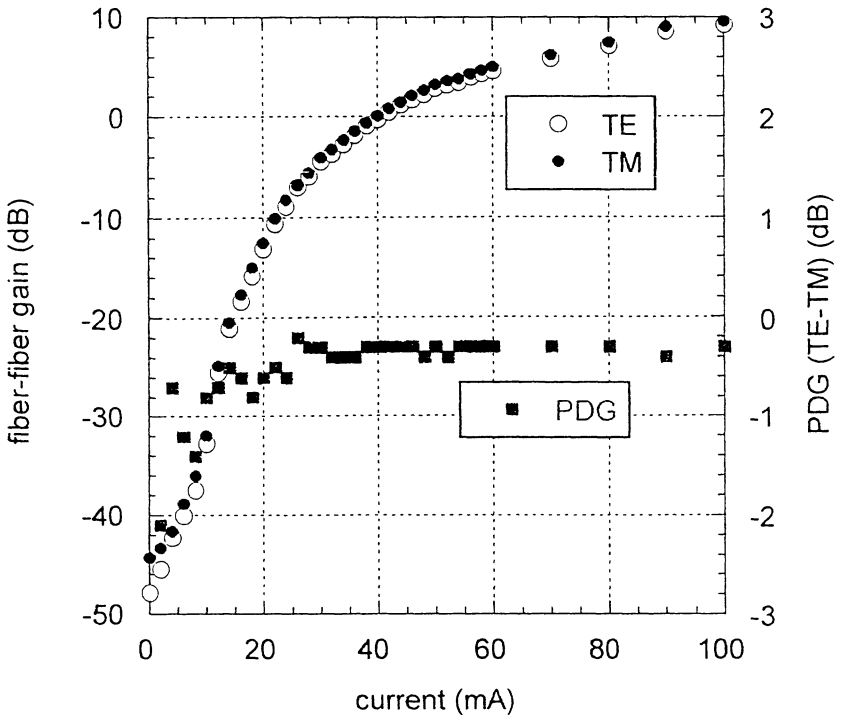

Figure 2-41 Gain characteristics

100 mA. Figure 2-42 shows the wavelength dependences of the fiber-to-fiber loss-less current, the extinction ratio, and the polarization dependence gain at an input of -10 dBm. Low loss-less operation current of less than 50 mA and a high extinction ratio of more than 40 dB are obtained over the entire fiber-amplifier gain band of 1530-1580 nm. It should be noted that the polarization dependence of 0.3 dB does not change over the entire 1530-1580 nm range. We carried out ASE spectrum measurement for the -0.47% strained sample. The spectrum shows that the ASE gain peak was 1520 nm at a loss-less current of 40 mA. The ASE output power difference between the TE and TM modes has relatively small wavelength dependence of less than 0.5 dB for the 1530-1580 nm region but it was 2 dB near 1520 nm. Therefore, we conclude that the short-wavelength ASE peak results in the insensitivity at longer wavelengths.

Other key parameters of the SOA gate were also measured. The saturation output power is 0 dBm, which is sufficient for an optical gate used in a loss-less condition. The noise figure is 8.5. The gating time is less than 1 ns (0-100%) or 600 ps (20-80%) for both rise- and fall-time on condition of 8 to 40 mA. The bit error rate for a

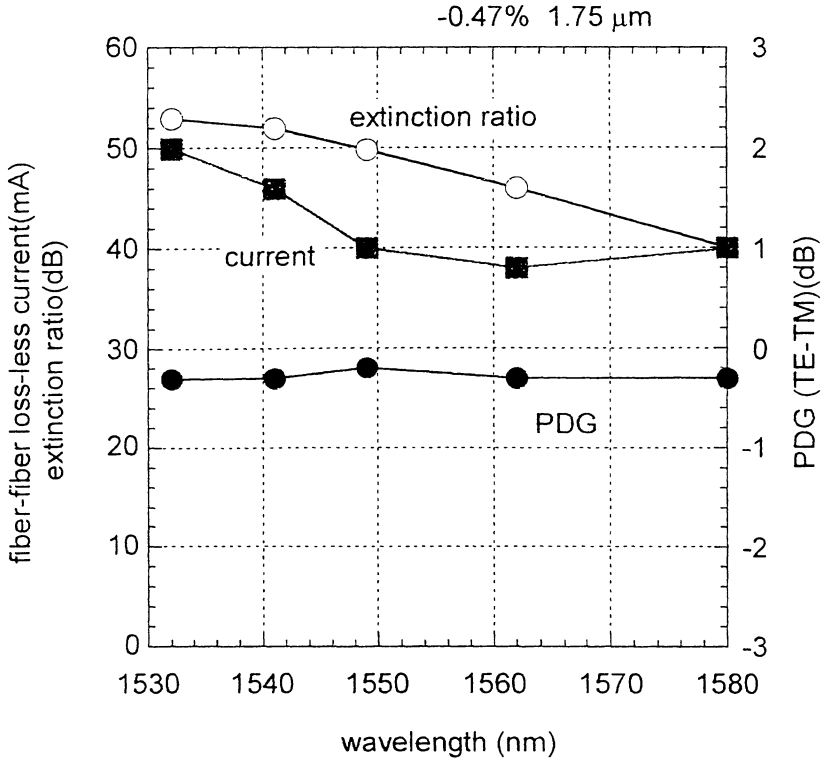

Figure 2-42 Wavelength dependences

10 Gbit/s optical signal is less than 10^{-11} when the received optical power is -31 dBm. These results indicate that the MQW-SOA is promising for use in optical packet switching, including a fast photonic asynchronous transfer mode (ATM) system [2.1, 2.2].

2.5. Summary of Chapter 2

The SOA described in Chapter 2 has an extremely low fiber-to-fiber lossless current of 5.4 mA at a 1580 nm input, because of its small square bulk active region of 0.3 μm (thickness)×0.3 μm (width). This operation current is lower than that of any SOAs so far reported.

The scattering of the polarization dependence gain, which is due to the unintended stain in the active layer, is within 0.5 dB, while the scattering in conventional SOA is as large as 2.0-2.5 dB. This is because the buried structure reduces

the amount of strain introducing to the square active layer.

The monolithic integration of spot size converters at both the input and output ports of the SOA array gates is indispensable for connecting an SOA to planar lightwave circuit (PLC) waveguide, because it enlarges the spot-size of SOA and keeps a large misalignment tolerance. A 4-channel polarization insensitive SOA integrated with spot-size converters (SS-SOA) gate array has been fabricated. The integrated spot-size converter utilizes a new butt-joint structure to optimize the bulk active layer and the spot-size converter region individually.

Cost is also an important issue. The SS-SOA array is generally much more expensive than a laser diode (LD), though their structures are very similar. This is because of the complexity involved in evaluating the polarization dependent gain of the SS-SOA. The polarization dependent gain in the SOA is known to be the sum of the polarization dependence in the active region gain and polarization dependence in the coupling efficiency at both facets. To reduce the evaluation cost, those characteristics must be measured through sampling and selection tests before the module fabrication process, and, if possible, before the anti-reflection (AR) coating is applied. We have proposed a novel method of precisely measuring the polarization dependent gain of a SS-SOA. By averaging the signal gain over a wide wavelength range, the polarization dependence gain can be accurately estimated with low reflection from gain ripples. We successfully evaluated the polarization dependence gain of an angled-facet SS-SOA even before the AR coating process. The measurement error is within 0.5 dB, which is small enough to evaluate the chip characteristics

The polarization dependence in the coupling efficiency between a SS-SOA and optical fiber has also been evaluated by measuring the photo-current for TE and TM input signals. It is possible, therefore, to specify the polarization characteristics of the active region and spot-size converter region of a SS-SOA. The details of the switching time of the SS-SOA gate are also described. By using a speed-up condenser, the switching time including the turn-on delay time is reduce to less than 2.5 ns, which is fast enough for packet switching.

Another type of SOA, with a 0.47 % tensile-strained MQW active region, has

also been constructed. By controlling the peak wavelength of the amplified spontaneous emission (ASE) to be 1520 nm at the lossless operating current, we achieved polarization independence for a signal wavelength between 1530 and 1580 nm. This is, to our knowledge, the largest wavelength range as an SOA with tensile-strained active layer. The fabricated MQW-SOA has low polarization dependence of 0.3 dB, which remains unchanged over driving currents between 30 and 60 mA and mesa stripe width between 1.0 and 1.75 μm.

References in Chapter 2

2.1. K. Habara, Y. Yamada, A. Misawa, K. Sasayama, M. Tsukada, T. Matsunaga, and K. Yukimatsu, "Demonstration of frequency-routing type photonic ATM switch (FRONTIER NET) prototype," ECOC'96, Oslo, Norway, post-deadline ThC.3.4, vol. 5-41, Sep. 1996.

2.2. K. Sasayama, K. Habara, W. De Zhong, and K. Yukimatsu, "Photonic ATM switch using frequency-routing-type time-division interconnection network," Electron. Lett., vol. 29, no. 20, pp.1778-1780, 1993.

2.3. M. Koizumi, T. Ido, S. Tanaka, M. Suzuki, and H. Inoue, "Ultra high speed switching of polarization and wavelength insensitive MQW electroabsorption optical gates," OECC'96, Makuhari Chiba, Japan, 17D4-3, pp. 206-207, 1996.

2.4. M. Jinno, T. Sakamoto, J. Kani, S. Aisawa, K. Oda, M. Fukui, H. Ono, M. Yamada, and K. Oguchi, "1580 nm band, equally spaced 8x10 Gb/s WDM channel transmission over 360 km (3x129 km) of dispersion-shifted fiber avoiding FWM impairment," OAA'97, Victoria, Canada, MC2-1, pp. 36-39, July 1997.

2.5. W. van Berlo, M. Janson, L. Lungen, A. C. Morner, J. Terlecki, M. Gustavsson, P. Granestrand, and P. Svensson, "Polarization-insensitive monolithic 4x4 InGaAsP/InP laser amplifier gate switch matrix", IEEE Photon. Technol. Lett., vol. 7, pp. 1291-1293, 1995.

2.6. K. Hamamoto and K. Komatsu, "Insersion-loss-free 2x2 InGaAsP/InP optical switch fabricated using bandgap energy controlled selective MOVPE", Electron. Lett., vol. 31, pp. 1779-1781, 1995.

2.7. R. Mestric, C. Porcheron, B. Martin, F. Pommereau, I. Guillemot, F. Gaborit, C. Fortin, J. Rotte, and M. Renaud, "Sixteen-channel wavelength selector monolithically integrated on InP", in Proc. OFC 2000, Baltimore, Maryland, TuF6, 2000.

2.8. Y. Yamada, H. Terui, Y. Ohmori, M. Yamada, and M. Kobayashi, "Hybrid-integrated 4x4 optical gate matrix switch using silica-based optical

waveguides and LD array chips", J. Lightwave Technol, vol. 10, pp. 383-389, 1992.

2.9. T. Kakitsuka, Y. Shibata, M. Itoh, Y. Tohmori, and Y. Yoshikuni, "Numerical analysis of polarization sensitivity in strained bulk semiconductor optical amplifiers", in Proc. IPRM 2001, Nara, Japan, ThA1-5, 2001.

2.10. M. Notomi, J. Hammersberg, H. Weman, S. Nojima, H. Sugiura, M. Okamoto, T. Tamamura, and M. Potemski, "Dimensionality effects on strain and quantum confinement in lattice-mismatched $InAs_xP_{1-x}$/InP quantum wires", Phys. Rev. B, vol. 52, pp. 11147-11158, 1995.

2.11. M. Bachmann, P. Doussiere, J. Y. Emery, R. N'Go, F. Pommereau, L. Goldstein, G. Soulage, and A. Jourdan, "Polarization-insensitive clamped-gain SOA with integrated spot-size convertor and DBR gratings for WDM system with 1.55 μm wavelength", Electron. Lett., vol. 32, no. 22, pp. 2076-2078, 1996.

2.12. D. Leclerc, P. Brosson, F. Pommereau, R. N'Go, P. Doussiere, F. Mallecot, P. Gavignet, I. Wamsler, G. Laube, W. Hunziker, W. Vogt, and H. Melchior: "High-performance semiconductor optical amplifier array for self-aligned packaging using Si V-groove flip-chip technique", IEEE photon. Technol. Lett., vol.7, no. 5, pp.476-478, 1995.

2.13. L. F. Tiemeijer, P. J. A. Thijs, T. v. Dongen, J. J. M. Binsma, E. J. Jansen, and A. J. M. Verboven, "27-dB gain unidirectional 1300-nm polarization-insensitive multiple quantum well laser amplifier module", IEEE Photon. Technol. Lett., vol. 6, no. 12, pp. 1430-1432, 1994.

2.14. K. Magari, M. Okamoto, and Y. Noguchi, "1.55-μm polarization-insensitive high-gain tensile-strained-barrier MQW optical amplifier", IEEE Photon. Technol. Lett., vol. 3, pp. 998-1000, 1991.

2.15. N. Yoshimoto, Y. Shibata, S. Oku, S. Kondo, Y. Noguchi, K. Wakita, and M. Naganuma, "Fully polarization independent Mach-Zehnder optical switch using a lattice-matched InGaAlAs/InAlAs MQW and high-mesa waveguide structure", Electron. Lett., vol. 32, no. 15, pp.1368-1369, 1996.

2.16. A. Godefroy, A. Le Corre, F. Clerot, S. Salaun, S. Loualiche, J. C. Simon, L. Henry, C. Vaudry, J. C. Keromnes, G. Joulie, and P. Lamouler, "1.55-μm polarization-insensitive optical amplifier with strain-balanced superlattice active layer", IEEE Photon. Technol. Lett., vol. 7, no. 5, pp. 473-475, 1995.

2.17. T. Ducellier, R. Basset, J. Y. Emery, F. Pommereau,, R. N'Go, J. L. Lafragette, P. Aubert, P. Doussiere, G. Laube, and L. Goldstein, "Record low noise factor (5.2 dB) in 1.55 μm bulk SOA for high bit rate low-noise preamplification", 22th European Conference on Optical Communication, ECOC' 1996, Oslo, Norway, vol. 3, pp. 173-176, WeD.2.5, 2001.

2.18. Y. Kondo, K. Kishi, M. Itoh, H. Oohashi, Y. Itaya, and M. Yamamoto, "1.3μm buried-heterostructure lasers using a CH4 reactive-ion-etched mesa structure grown by metalorganic vapor phase epitaxy," Indium Phosphide and their Related Materials, IPRM'96, Stadtgarten, Germany, TuB 2-3, pp. 384-387, 1996.

2.19. S. Kitamura, K. Komatsu, and M. Kitamura, "Very low power consumption semiconductor optical amplifier array", IEEE Photon. Technol. Lett., vol. 7, no. 2, pp. 147-148, 1995.

2.20. T. Ito, N. Yoshimoto, O. Mitomi, K. Magari, I. Ogawa, F. Ebisawa, Y. Yamada, and Y. Hasumi, "Polarization independent semiconductor optical amplifier gate and its application in WDM systems," IEICE Transaction on Electronics, Vol. E81-C, No. 8, pp. 892-897, 1998.

2.21. T. Kakitsuka, Y. Shibata, M. Itoh, Y. Tohmori, and Y. Yoshikuni, "Numerical analysis of polarization sensitivity in strained bulk semiconductor optical amplifiers", Indium Phosphide and their Related Materials, IPRM 2001, Nara, Japan, ThA1-5, 2001.

2.22. O. Mitomi, N. Yoshimoto, K. Magari, T. Ito, Y. Kawaguchi, Y. Suzuki, Y. Tohmori, and K. Kasaya, "Analyzing the polarization dependence in optical spot-size converter by using a semivectorial finite-element beam propagation method", IEEE J. Lightwave Technol., vol. 17, no. 7, pp. 1255-1262, 1999.

2.23. Y. Tohmori, Y. Suzaki, H. Fukano, M. Okamoto, Y. Sakai, O. Mitomi, S.

Matsumoto, M. Yamamoto, M. Fukuda, M. Wada, Y. Itaya, and T. Sugie: "Spot-size converted 1.3μm laser with butt-jointed selectively grown vertically tapered waveguide". Electron. Lett., 31, pp. 1838-1840, 1995.

2.24. N. Yoshimoto, K. Magari, T. Ito, K. Kawaguchi, O. Mitomi, Y. Tohmori, "Polarization-insensitive semiconductor optical amplifier gate switch with butt-jointed spot-size converters – its uniformity", IEE Proc. Optoelectron., vol. 146, no. 1, pp. 71-76, 1999.

2.25. T. Saitoh, and T. Mukai, "1.5 μm GaInAsP traveling-wave semiconductor laser amplifier", IEEE J. Quantum. Electron., vol. QE-23, no. 6, pp. 1010-1020, 1987.

2.26. Y. Suzaki, K. Magari, O. Mitomi, Y. Kondo, Y. Kawaguchi, Y. Kadota, "4-ch high-gain semiconductor optical amplifier array integrated with a bent spot-size converter", Optical Amplifier and their Applications, OAA 2000, Quebec, Canada, OMC3, 2000.

2.27. T. Ito, N. Yoshimoto, K. Magari, and H. Sugiura, "Wide-band polarization-independent tensile- strained InGaAs MQW-SOA gate," IEEE Photon. Technol. Lett., vol. 10, no. 5, pp. 657 –659, 1998.

2.28. J. Y. Emery, P. Doussiere, L. Goldstein, F. Pommereau, C. Fortin, R. N' Go, N. Tscherptner, J. L. Lafragette, P. Aubert, F. Brillouet, G. Laube, J. Barrau, "New, process tolerant, high performance 1.55 μm polarization insensitive semiconductor optical omplifier based on low tensile bulk GaInAsP", 22nd European Conference on Optical Communication, ECOC 1996, vol. 3, pp. 165-168, 1996.

2.29. L. F. Tiemeijer, P. J. A. Thijs, T. v. Dongen, J. J. M. Binsma, E. J. Jansen, and A. J. M. Verboven, "27-dB gain unidirectional 1300-nm polarization-insensitive multiple quantum well laser amplifier module", IEEE Photon. Technol. Lett., vol. 6, no. 12, pp. 1430-1432, 1994.

2.30. H. Sugiura, S. Kondo, M. Mitsuhara, S. Matsumoto, and M. Itoh, "Be-Zn interdiffusion and its influence on InGaAsP lasers fabricated by hybrid growth of chemical beam epitaxy and metalorganic vapor phase epitaxy," Appl. Phys.

Lett., vol. 70, no. 21, pp.2846-2851, 1997.

Chapter 3

SOA based modules as key elements of all-optical signal processing

Chapter 3 described the integrated SOA devices as key elements of all-optical signal processing. Hybrid integrations of the SS-SOA and PLC platform, such as the SOA gate array, wavelength selector, and wavelength converter, were discussed. The fabrication of the monolithic integrated wavelength converter, that is the Sagnac interferometer integrated with a Mach-Zehnder interferometer was described.

3.1. Planar lightwave circuit (PLC)

3.1.1. PLC waveguide

An integrated passive optical circuit that uses a silica waveguide on silicon substrate is named a planar lightwave circuit (PLC), and has been studied around the world [3.1, 3.2]. The silicon substrate is low in cost and available in electronics areas. The silica waveguides have the same refractive index as optical fibers, so a good coupling efficiency with fibers can be expected. The amplitude, phase, and polarization of optical signal are efficiently controlled, because the waveguide has a well-defined core shape. Therefore, a variety of PLCs such as optical splitters, switches, and arrayed waveguide gratings (AWG), have been fabricated.

The PLC has a square SiO_2-GeO_2 silica core defined by photolithography and reactive ion etching (RIE). The silica core is buried with SiO_2 glass using a frame hydrolysis deposition (FHD) technique developed for optical fiber fabrication [3.3]. The total thickness of the SiO_2 glass layer on the Si substrate is around 50 μm. The refractive index difference Δ between the core and cladding SiO_2 glass is 0.25 to 2 %, as listed in Table 1. Low-Δ waveguides are preferred for the fabrication of simple PLCs that require lower fiber coupling losses. The higher-Δ waveguides in Table 3-1 are used for the fabrication of large-scale PLCs with complex waveguide bends.

Table 3-1 Parameters for PLC waveguides

Waveguide type	low Δ	middle Δ	high Δ	super-high Δ
Refractive index difference (%)	0.25	0.45	0.75	1.5 - 2
Core size (μm)	8 x 8	7 x 7	6 x 6	4.5x4.5 – 3x3
Loss (dB/cm)	< 0.1	< 0.1	< 0.1	0.1
Coupling loss (dB)	< 0.1	0.1	0.5	2
Bending radius (mm)	25	15	5	2

Optical crossbar switches using the thermo-optic (TO) effect have been fabricated. Figure 3-1 shows the logical arrangement of an 8x8 crossbar switch using 2x2 elements. The 64 elements, forming a diamond-shaped area, are each controlled in a cross state or bar state. At zero bias, the element is fixed in the cross state, but it can be switched to the bar state with a control signal. Each 2x2 switch element, which is shown in Fig. 3-2, is a symmetrical Mach-Zehnder interferometer (MZI) that consists of two directional couplers and two waveguide arms. Phase shifters, which are thin-film heaters, are deposited on both arms to provide a silica core with optical tuning or switching functions utilizing the thermo-optic (TO) effect in the refractive index of silica core ($1x10^{-5}$/K). Figure 3-3 is the waveguide layout of an 8x8 switch matrix on a

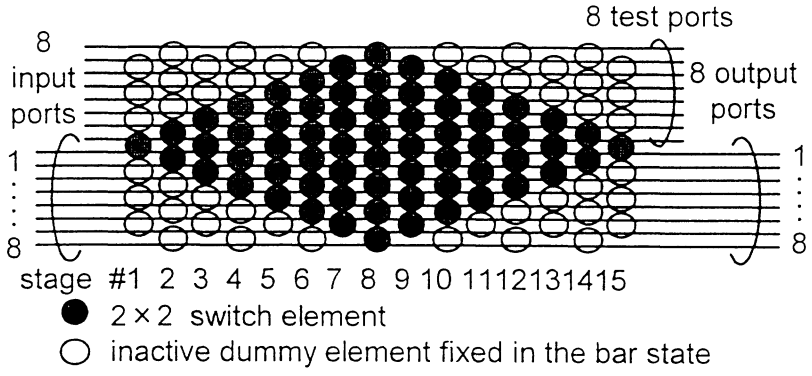

Figure 3-1 Switch matrix arrangement

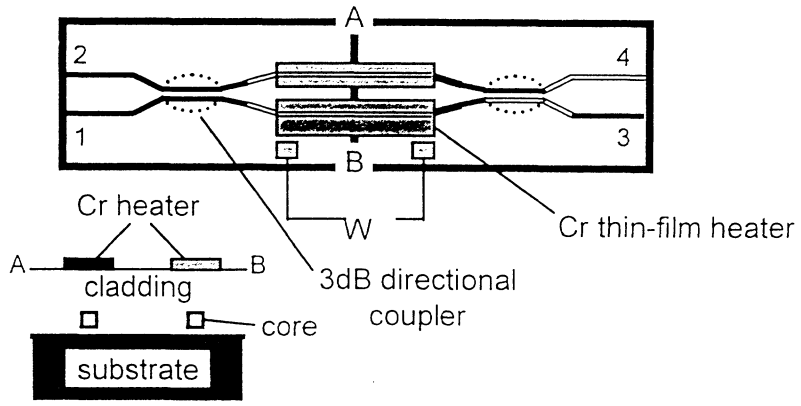

Figure 3-2 2x2 switch element

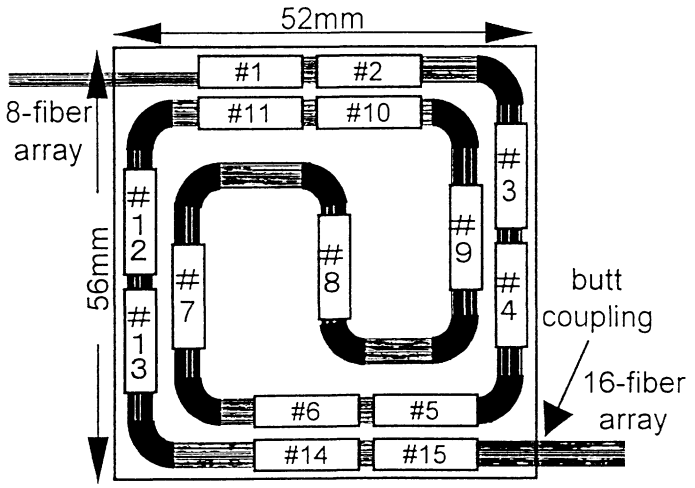

Figure 3-3 Waveguide layout on silicon substrate

3-inch silicon substrate. Since a single switch element is 15-mm long and a linear 15-stage switch matrix would exceed the diameter of the silicon wafer, the whole switch matrix is folded. Fiber arrays of 16 single-mode fibers (8 for the signals and 8 for the test) are butted to the facet of the input and output port. Figure 3-4 shows the relationship between supplied heating power and normalized output power for one of the elements of the TO switch. The solid line and the dotted line represent the output power normalized to the input power for a signal fiber and a test fiber, respectively.

Note that the crosstalk at 0 mW is not a minimum. This is due to a small difference in the optical length between the arms of the Mach-Zehnder interferometer (MZI). Therefore, a little bias power is applied and the crosstalk is reduced a few dB. The averaged loss of 64 paths is 12.7 dB. There is only a small difference of less than 3 dB between the loss values. The averaged crosstalk is –24.2 dB.

A practical 16 x 16 TO matrix switch was also fabricated [3.4] using a 6-inch wafer. Its arrangement has a strictly non-blocking structure and the insertion loss is path-independent. Each switch element has a double-MZI structure, as shown in Fig. 3-5, which is composed of two asymmetrical MZIs with an optical path length difference of a half-wavelength, a TO thin heater, and an intersection. As the leaked light power from the first MZI is blocked again by the second MZI, the double-MZI element provides a high extinction ratio in the bar-path, which is important in the matrix

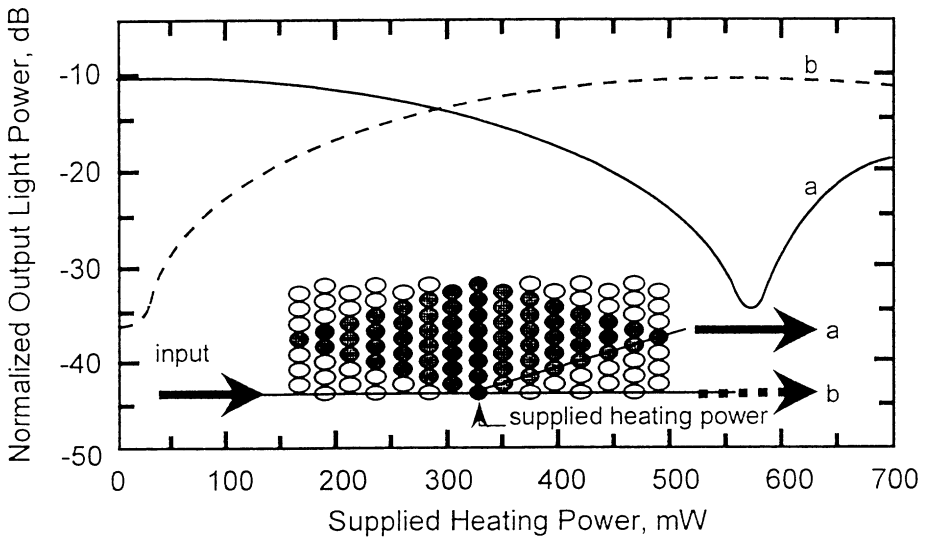

Figure 3-4 Supplied heating power versus normalized output light power

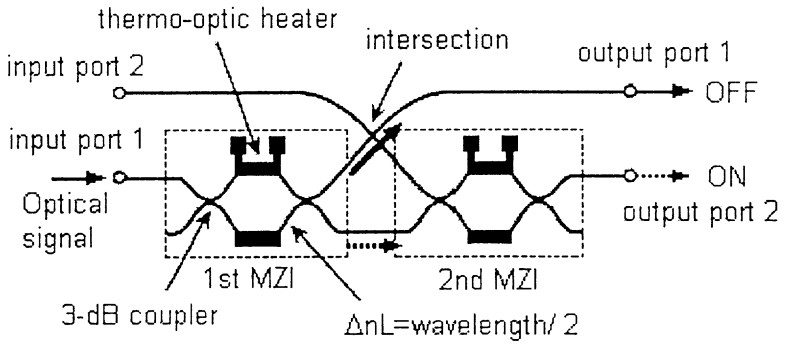

Figure 3-5 2x2 switching element with a double-MZI configuration

switch configuration. A simple phase trimming technique employing high-power local heating, corrects permanently the phase error in each MZI, eliminating the need for electrical biasing.

3.1.2. Arrayed waveguide grating (AWG)

The structure of the PLC arrayed waveguide grating (AWG) is shown in Fig. 3-6. It consists of input and output waveguide arrays, two slab waveguides, and a

phased-array region of multi-channel waveguides with an optical length difference ΔL between adjacent waveguides. A WDM optical signal from one of the input waveguides radiates in the slab waveguides and is then coupled to the multi-channel waveguides. After traveling through the multi-channel waveguides, the light converges on a focal line where the ends of the output waveguides are located. As each channel of the WDM signal converges on different positions on the focal line, depending on the wavelength, the AWG can be used as a multiplexer/demultiplexer of WDM signals.

The design of the AWG is as follows. The ΔL results in the phase difference of $2\pi n \Delta L/\lambda$, where n is the effective refractive index of the PLC waveguide, and λ is the light wavelength. The light emitted to the slab waveguide from the multi-channel waveguides is diffracted at an angle θ which satisfies

$$n(\Delta L + d\sin\theta) = m\lambda, \quad (1)$$

where d is the pitch of the multi-channel waveguides at their exits and m is the diffraction order. The dispersion $dx/d\lambda$, where x is position of the converged beam on the focal plane (the edge of the output waveguides at the slab waveguide), is derived by differentiating eq. 1 as

$$dx/d\lambda = fm/nd, \quad (2)$$

where f is the focal length, which is equal to the length of the slab waveguide. The full width at half-maximum (FWHM) of the converted beam is at best $\lambda f/nNd$ because of

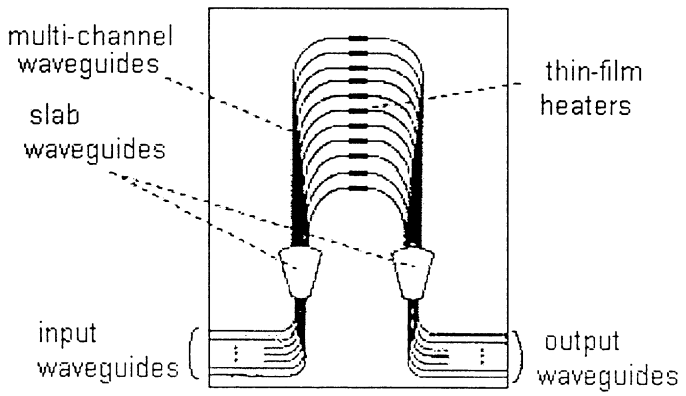

Figure 3-6 Arrayed waveguide grating

the diffraction limit, where N is the number of waveguides of the multi-channel waveguides. Using the FWHW and the dispersion, the wavelength resolution $\Delta\lambda$ is given by

$$\Delta\lambda = \lambda/Nm. \quad (3)$$

Equation 3 shows that high-order diffraction is needed or high resolution. In eq. 1 the diffraction order is given by $m = n\Delta L/\lambda$ for small θ. Therefore an AWG with large ΔL can multiplex and demultiplex the WDM signal with a small wavelength spacing. In fact, a practical AWG such as 32x32 channels with 100 GHz spacing and 64x64 channels with 50 GHz spacing have been fabricated.

3.1.3. SS-SOA/PLC hybrid integration

Another important role of the PLC is to provide platforms for semiconductor and PLC hybrid integration. The Si substrate can be used as the heat sink and optical bench on which the semiconductor chips, such as SOAs and laser diodes, are mounted and coupled to the silica core. Figure 3-7 illustrates the PLC platform structure [3.5]. The silica waveguide is formed only on the ground plane of the silicon substrate, and the terraced surface acts as an optical bench. High-speed electrical wiring can be formed

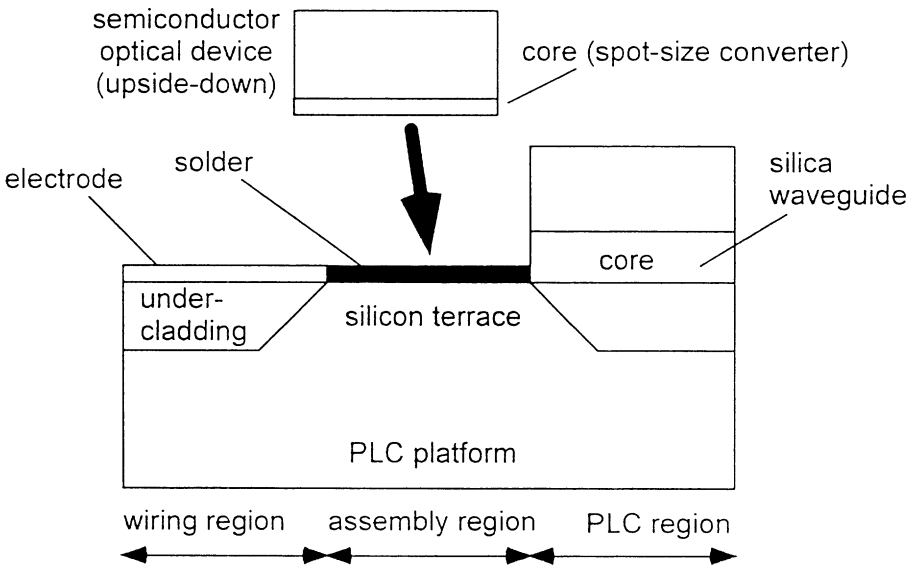

Figure 3-7 Cross-sectional view of a PLC platform

on the platform for ns operation of the SS-SOA gate.

One of the applications of the gate array module is a wavelength selector that consists of a two AWGs and a SOA gate array. It operates as a digital tunable dropping filter for WDM wavelength channels, as shown in Fig. 3-8. Zirngibl et al. demonstrated a monolithic wavelength selector with rib-loading InGaAsP AWGs and quantum well SOAs [3.6]. But it is hard to use practically because it is difficult to get wide wavelength range of polarization independence.

NTT Corporation has developed 8- and 32-channel wavelength selector modules, which consists of two and eight 4-channel SS-SOAs respectively, as shown in Fig. 3-9. The key technique is the multi-platform scheme using PLC-PLC direct attachment [3.7]. By using this technique, complicated and large-scale-integration modules can be simply constructed by attaching separately fabricated PLC elements without any deviation in the optical path length. It should be noted the PLC-PLC attachment can be easily achieved in the same way as the well established fiber-PLC connection. This modular scheme not only eliminates the wafer size limitation but also greatly simplifies the design and fabrication of hybrid-integrated modules.

The 32-channel wavelength selector consists of a 1 x 32 input AWG, a 32-ch optical gate array circuit (eight 4-ch SS-SOA on a PLC platform), and a 32 x 1 output AWG. The PLC-platform and two 100-GHz AWGs were fabricated separately, and then the AWGs were directly connected to either side of the PLC platform using UV curable adhesive. The input and out put fibers were also connected to the AWGs. The average insertion loss of the 32-channel is 2.3 dB. Eight sets of 4-channel electronic gate drivers, which has an emitter coupled logic digital interface, were installed on a printed wiring board.

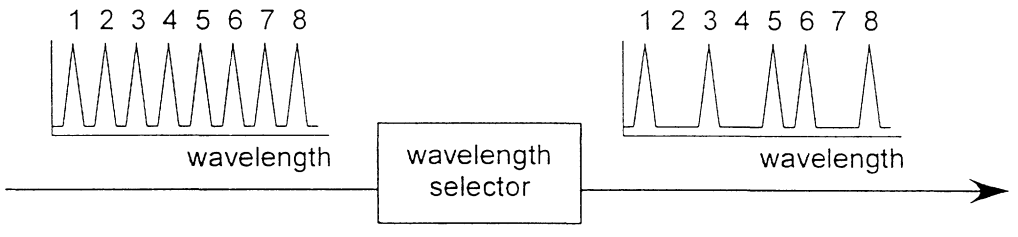

Figure 3-8 Principle operation of the wavelength selector

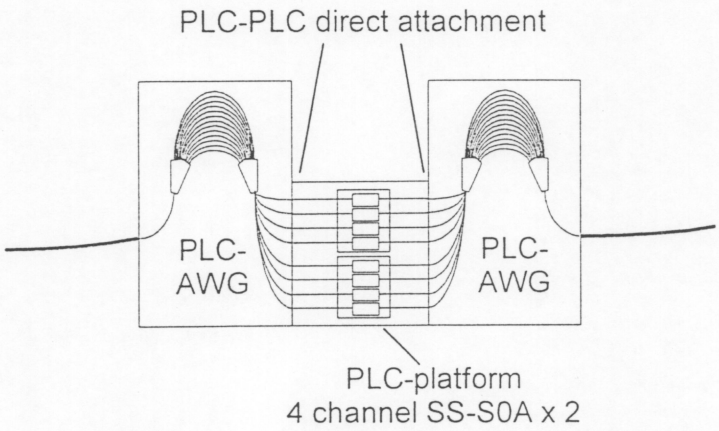

Figure 3-9 Configuration of the wavelength selector

3.2. Optical gate array modules

The SOA chip must be fully packaged with electrical connectors and input/ output fibers for the practical use in WDM system. The key point is how to connect the fiber to the SOA chip. It has been done using a couple of lenses, which is somewhat a expensive technique. Passive alignment, which mounts the SS-SOA on the PLC platform, is a very simple and low cost packaging technology.

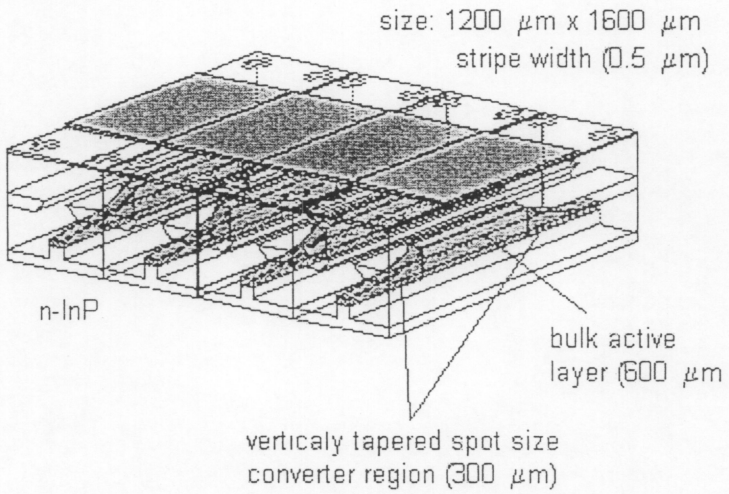

Figure 3-10 Four channel SS-SOA

3.2.1. SOA gate array module

After anti-reflection coating, a 4-channel SS-SOA chip (Fig. 3-10) was bonded with an AuSn solder on a PLC platform (Fig. 3-11) using the passive alignment technique. The core of the PLC waveguide was 6 μm x 6 μm in size with a refractive index difference of 0.75%. The space between the facet of the SS-SOA and the angled facet of PLC was 10-15 μm. The input and output single-mode fiber arrays were connected to both facets of the 4-channel PLC waveguides. The total coupling loss between the SOA gates and fiber, including the coupling loss between the SOA gates and the PLC, was 5 dB.

Figure 3-12 shows the fiber-to-fiber gain versus the driving current of the hybrid gate array module (a 4-channel SS-SOA gate on a PLC platform) at a wavelength of 1550 nm. The optical input power was -10 dBm. The gain characteristics of each channel are very similar. Fiber-to-fiber loss-less was obtained at 33 mA for all channels. The detailed gain characteristics of the 4 channels are shown in Fig. 3-13. A high extinction ratio of nearly 40 dB, defined as the optical loss at 0 mA, was achieved

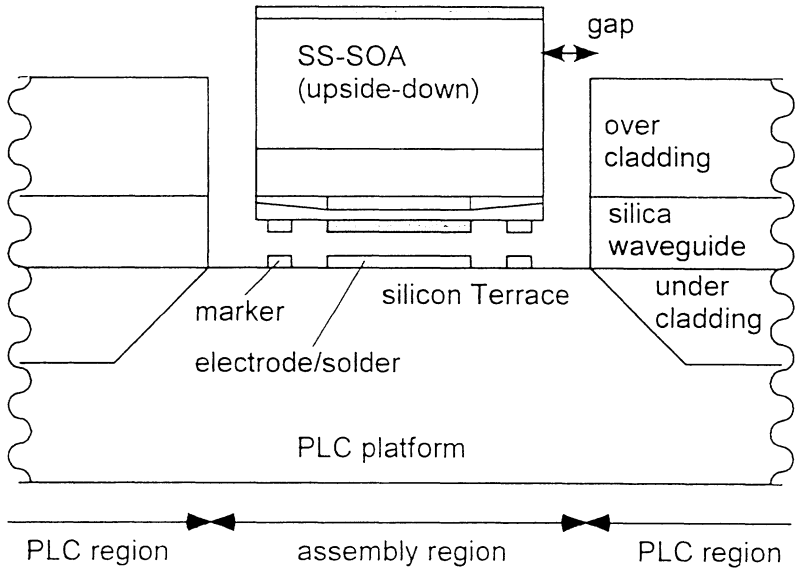

Figure 3-11 Cross-sectional view of SS-SOA/PLC hybrid integration

in all channels. The polarization dependence gain (PDG) was 0.5 to 0.8 dB, which agree well with the calculation (Fig. 2-14). Figure 3-14 shows the wavelength sensitivity of the extinction ratio and the loss-less current of a gate array module. The extinction ratio

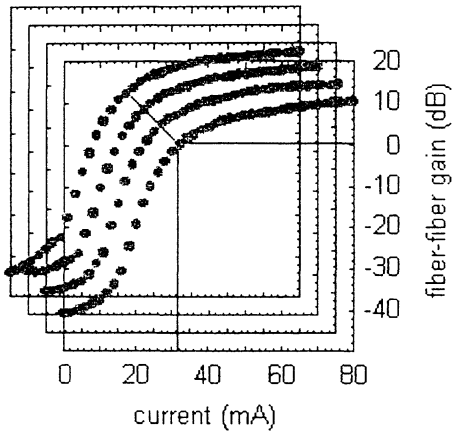

Figure 3-12 Gain characteristics of 4 channel SOA module

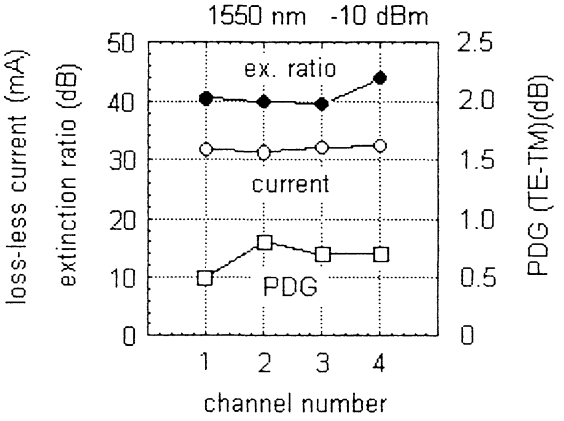

Figure 3-13 Details of gain characteristics

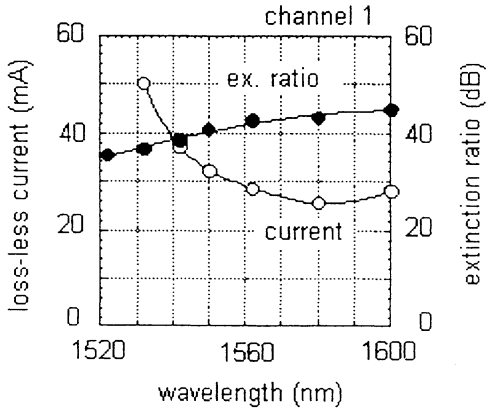

Figure 3-14 wavelength characteristics

was more than 35 dB and the fiber-to-fiber loss-less current was less than 50 mA over a wide wavelength range of 1530 to 1600 nm. The minimum lossless current was 25 mA for 1580 nm.

3.2.2. Wavelength selector (with a PLC-AWG and SOA gate array module)

One of the applications of the SOA gate array module is a wavelength selector, which operates as a digitally tunable dropping filter of wavelength channels. Using a hybrid SS-SOA gate array module and a PLC-AWG wavelength multiplexer, the wavelength selector can be applied in a practical system because the polarization independent and ultra-wide-band (1530-1600 nm) operations were proven. Figure 3-15 shows the high-speed wavelength selector using 4-channel gate array module and 8x8 PLC-AWG. Four wavelengths, 1532.0, 1553.5, 1554.3, and 1600.0 nm at 2.5 Gbit/s, 10 Gbit/s, 10 Gbit/s, and 633 Mbit/s, respectively, were demultiplexed by the PLC-AWG and were selected by the gate array module [3.8]. Note that the wavelength selector operated in an ultra-wide band of 1532 to 1600 nm. Wavelength separation can be set at 0.8 nm, as shown in the separation between channels 2 and 3. The crosstalk between the channels of the PLC-AWG is less than -30 dB. The input power to the SOA gate was

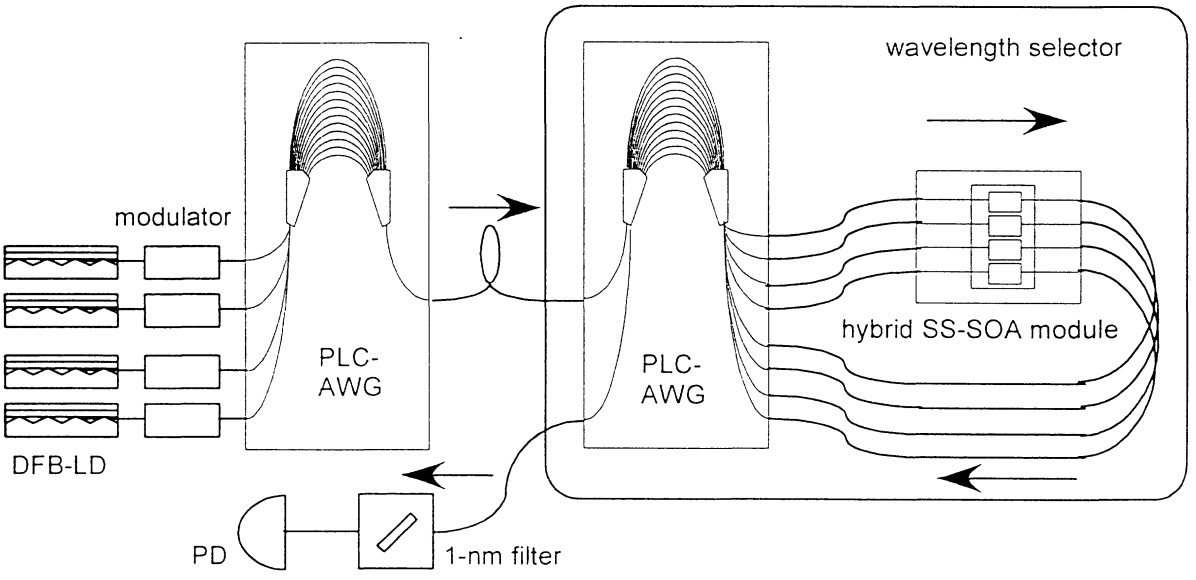

Figure 3-15 Setup for wavelength selector using a PLC-AWG and a SS-SOA module

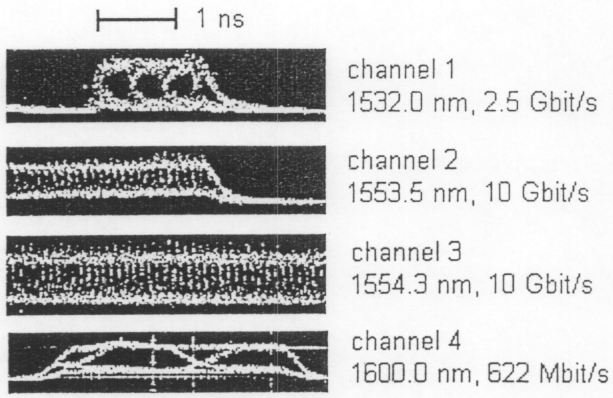

Figure 3-16 Dynamic responses of a wavelength selector

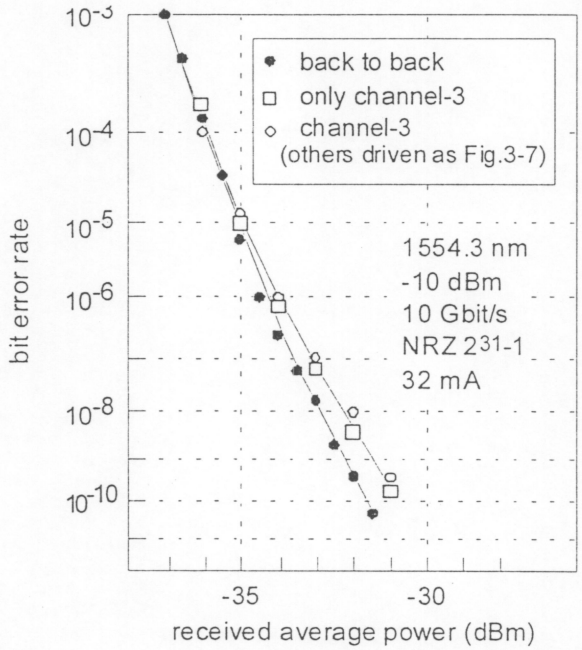

Figure 3-17 Bit error rate of a wavelength selector

-10 dBm. The driving currents for the SS-SOA gates were 10 mA at the off states and 50 mA at the on states. A tunable filter with a 1-nm bandwidth was used before the photodetector. Figure 3-16 shows the dynamic responses of the wavelength selector. Both the rise- and fall-times are less than 1 ns, which makes the wavelength selector suitable for high-speed optical packet switching, including photonic ATM system [3.1, 3.2]. We also checked the electrical and optical interference between channels by means of bit error rate (BER) measurements. The BER of channel-3 was measured, as shown

in Fig. 3-17. Though the other channels were randomly driven, no power penalty was observed. The electrical or optical interference between channels, which causes the noise to the measured channel-3 was, therefore, negligible.

3.2.3. Wavelength selector module

To reduce the size and cost of the wavelength selector, the PLC platform and AWG should be integrated. However, the wafer size limitation, the difficulty of evaluating the performance of each circuit element, and the fabrication yield prevent large-scale integration. To overcome these problems, we introduced a multi-platform scheme using the PLC-PLC direct attachment technique [3.3]. By using this technique, complicated and large-scale integration modules can be simply constructed by attaching separately fabricated PLC elements without any large degradation in the optical path length deviation. This modular scheme does not only eliminate the wafer size limitation, but greatly simplifies the design and fabrication of hybrid integration modules.

The 8-channel wavelength selector module is divided into three PLC elements: a 1 x 8 input AWG with a 100 GHz spacing, a 8-channel SS-SOA hybrid integrated on a PLC platform, and a 8 x 1 output AWG. The PLC platform consists of two 4-channel SS-SOA gate array chips, as shown in Fig. 3-18. The silica waveguide core is 6 μm^2 and has a refractive index difference of 0.75%. Au/Sn solder pads and Au electrodes were

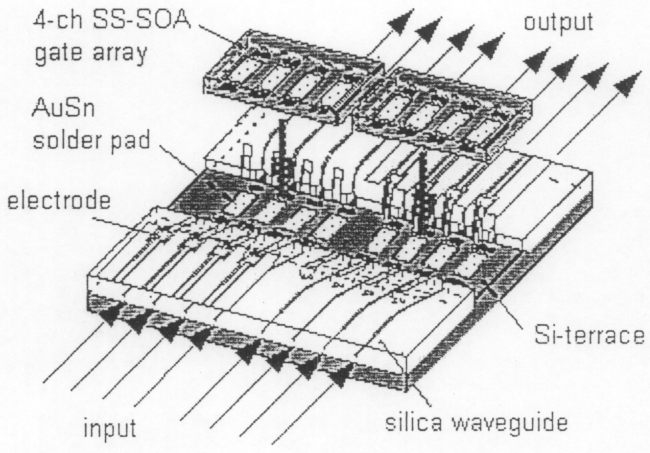

Figure 3-18 SS-SOAs on a PLC platform

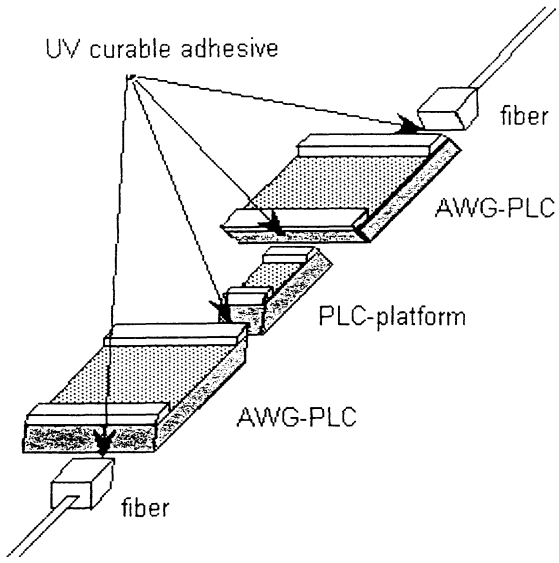

Figure 3-19 Direct attachment technology

SS-SOA gate arrays were flip-chip bounded on the PLC platform using passive alignment. The space between the SS-SOA and PLC' s angled facet is 10-15 μm, and the estimated coupling losses are 3.9-4.9 dB/point.

Two PLC-AWGs with a transmission loss of 3.2-3.9 dB were directly attached to the PLC platform using UV curable adhesive, as shown in Fig. 3-19. It should be noted that direct PLC-to-PLC attachment can be easily achieved using the same well-established procedure for PLC-to-fiber connection. The PLC-fiber and PLC-PLC coupling losses are 0.4 and 0.3 dB/point, respectively. The input and output fibers were also connected to the AWGs.

Figure 3-20 shows the structure, and Table 3-2 shows the loss budget of the 8-ch wavelength selector. Figure 3-21 is a photograph of the fabricated wavelength selector module. Figure 3-22 shows the optical transmission spectra of the wavelength selector at an injection current of 50 mA and input optical power of -10 dBm. The 3-dB bandwidth of each channel is about 30 GHz. The peak transmission powers are almost uniform. Figure 3-23 shows the gain characteristics at the center wavelength of the transmission band. For all 8-channel, fiber-to-fiber lossless operation was obtained at an injection current of 40-45 mA. The polarization dependence gain is less than 1 dB for

injection current of 40-45 mA. The polarization dependence gain is less than 1 dB for input power of 8 dBm.

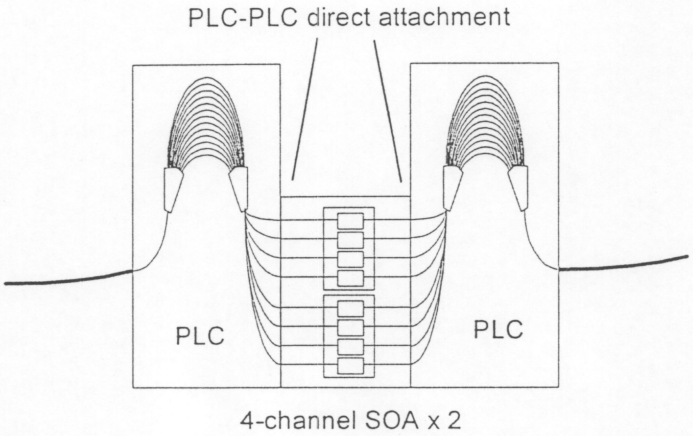

Figure 3-20 Structure of wavelength selector

Table 3-2 Loss diagram

	loss (dB)
AWG transmission loss	3.2 – 3.9
SOA/PLC coupling loss	3.9 – 4.9
PLC/fiber coupling loss	0.4
PLC/PLC coupling loss	0.3

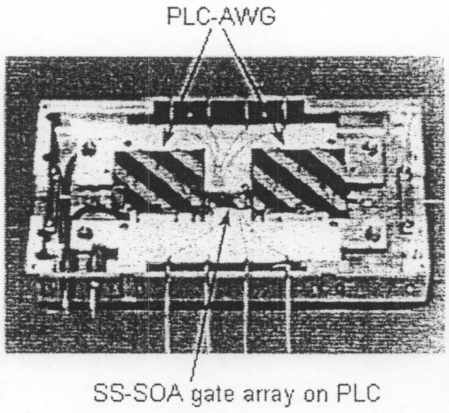

Figure 3-21 Photograph of a wavelength selector

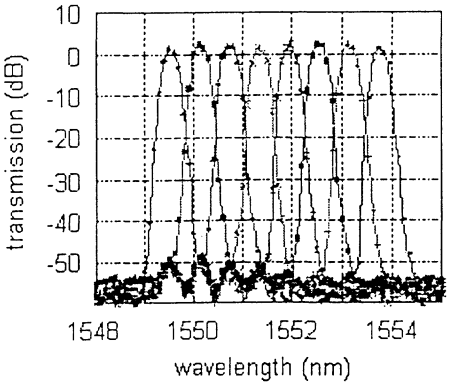

Figure 3-22 Transmission spectra

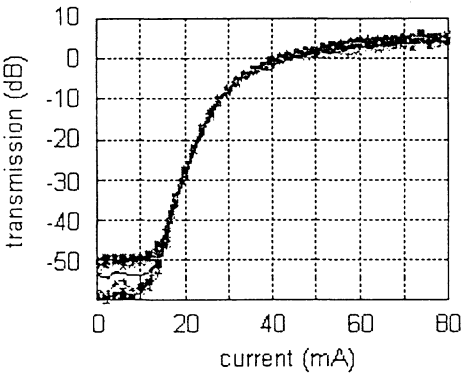

Figure 3-23 Gain characteristics

3.3. Wavelength conversion device

3.3.1. Hybrid integrated cross phase modulation (XPM)

Figure 3-24 shows schematic views of the hybrid integrated MZI module [3.12]. The 2-channel SS-SOA was flip-chip bonded with a Au/Sn solder on a PLC platform. The space between the SS-SOA and the PLC' s angled facet is 10-15 μm. The averaged coupling loss between the SS-SOA and the PLC waveguide was estimated as

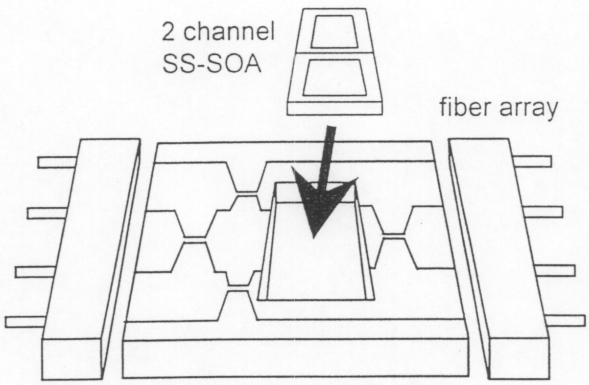

Figure 3-24 Hybrid integrated wavelength converter

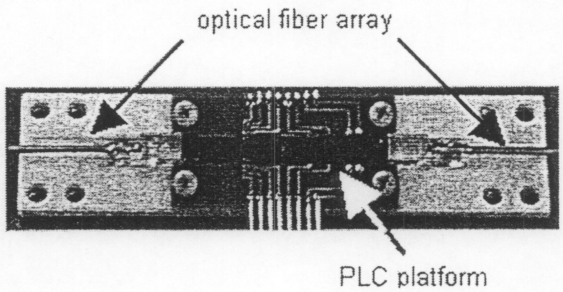

Figure 3-25 Photograph of a hybrid integrated wavelength converter

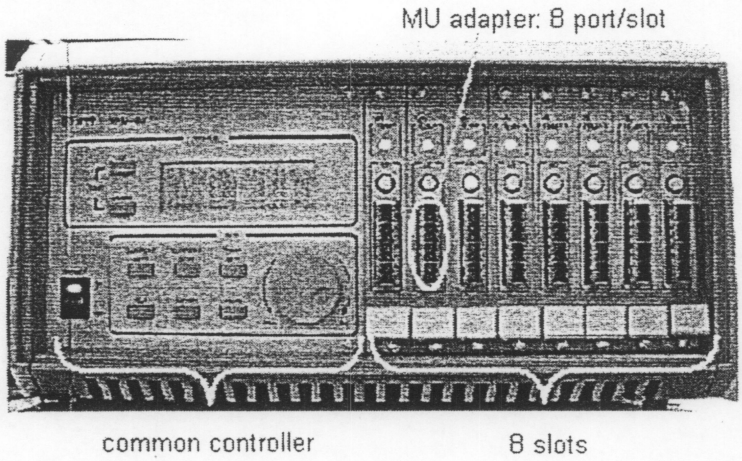

Figure 3-26 Eight-slot module

4 dB. The four-single-mode-fiber array is directly attached to the both sides of the PLC by using UV-curable adhesive. Figure 3-25 and 3-26 show photographs of a module and eight- slot equipment with eight modules.

Figure 3-27 is an example of static all-optical switching curve, which shows wavelength conversion from the input signal with wavelength of λ_{in} to the converted

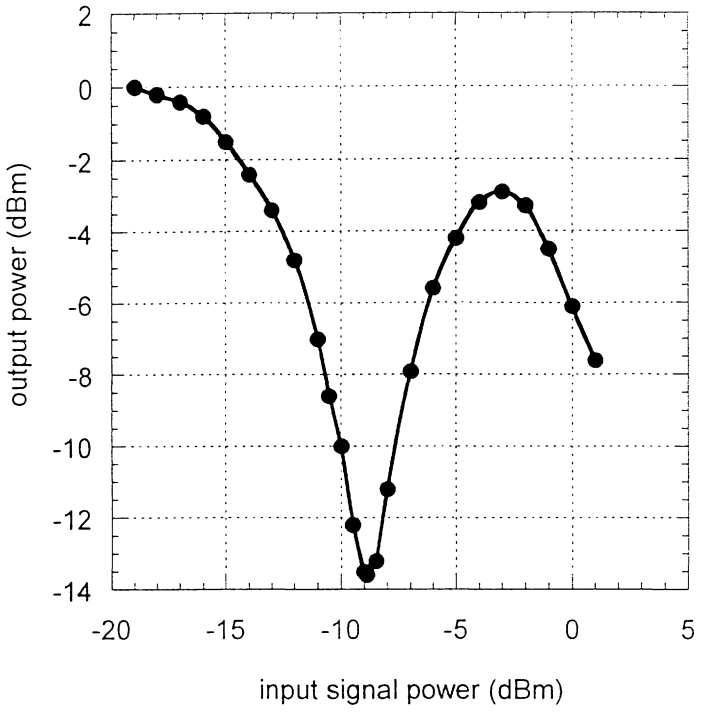

Figure 3-27 Characteristics of cross phase modulation

signal with a wavelength of λ_c. The module was set to the inverted operation mode. A low input signal power operation of −10 dBm was achieved. The bias currents of the two SS-SOAs were 85 and 130 mA.

3.3.2. Monolithic integrated differential phase modulation (DPM)

Figure 3-28 is a photograph of a Sagnac interferometer with parallel-amplifier structure (SIPAS), which is a deep-ridge waveguide MZI having polarization insensitive SOAs in both arms [3.13]. It was fabricated with a technique for joining the deep-ridge waveguide to a buried passive waveguide, and the passive waveguide to the SOA. The SOA active layer is 0.1 % tensile-strained bulk InGaAsP and 0.3-μm thick. A 0.5 μm-thick InGaAsP core (λg= 1.05 μm) was used for the passive waveguide. The

propagation loss of the deep-ridge passive waveguide is about 5 dB/cm. The coupling loss between the SOA and passive regions is about 1 dB, including the active-to-passive coupling loss and deep-ridge to buried coupling loss. SOA lengths are 600 μm, and total chip length is 4.5 mm.

The working principle of the SIPAS is similar to that of the SLALOM [3.14]. An input CW light is divided into clockwise (CLW) and counterclockwise (CCW) traveling lights. Since the PAS is asymmetrically placed in the loop, the CLW and CCW lights reach the SOAs at different times, which leads to different phase modulation between CLW and CCW lights when signal light is input into the SOAs. After traveling the loop, CLW and CCW lights are superimposed and transmitted to the output port due to differential phase modulation (DPM). We place the PAS asymmetrically by 0.5 mm so that the switching window thanks to DPM becomes 10 ps, which enables the high-speed operation over 40 Gbit/s. If the PAS is set in the cross state the signal light cannot get into the loop, which shows the possibility of filter-free wavelength

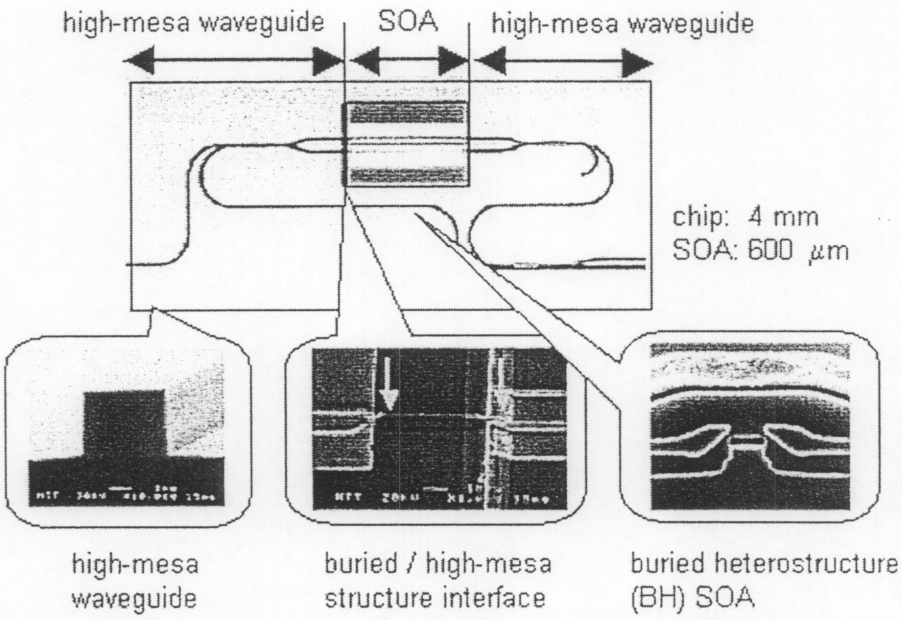

Figure 3-28 Structure of a SIPAS

conversion.

3.4. Summary of Chapter 3

Chapter 3 discusses hybrid integration of SS-SOA and planar lightwave circuit (PLC). The hybrid integration is considered to be an attractive way to fabricate practical modules with functional PLC waveguides, such as couplers or arrayed waveguide gratings (AWGs). Moreover, it is easy to connect PLC waveguides to fiber arrays.

A 4-channel SS-SOA gate array was assembled on a PLC platform for the first time. The PLC has an angled waveguide facet structure, which effectively reduces the waveguide facet reflection without any significant coupling loss increase. The coplanar waveguide formed on a thick silica layer ensures high-speed electrical signal transmission. The 4-channel SS-SOA/PLC hybrid gate array module has an extinction ratio higher than 35 dB, operating at less than 50 mA. The polarization dependence is less than 1 dB throughout an ultra-wide-band of 1530-1600 nm. The spot-size conversion structure of the SS-SOA reduces the coupling loss to about 4 dB and improves the 1-dB down tolerance to better than 2 and 20 μm for the horizontal and axial directions, respectively. These large tolerances are essential for suppressing the coupling loss variation among channels.

We demonstrated the first 4-channel high-speed wavelength selector with a combination of two modules: an SS-SOA hybrid gate array module and a PLC-AWG. It can be used in a practical system because polarization independent and ultra-wide-band (1530-1600 nm) operations were proven. The rise- and fall-times were less than 1 ns, which make the wavelength selector suitable for packet switching.

In the part of chapter 3, Sagnac interferometer integrated with parallel-amplifier structure (SIPAS), is described. The SIPAS is fabricated monolithically by butt-coupling the passive high-mesa waveguide and buried active layer. It enables a fast wavelength conversion and filterless operation.

References in Chapter 3

3.1. M. Kawachi, "Recent progress in silica-based planar lightwave circuits on silicon", IEE proc.-Optoelectron., vol. 143, no. 5, pp. 257-262, 1996.

3.2. Y. P. Li, and C. H. Henry, "Silica-based optical integrated circuits", IEE proc.-Optoelectron., vol. 143, no. 5, pp. 262-280, 1996.

3.3. A. Kilian, J. Kirchhof, B. Kuhlow, G. Przyrembel, and W. Wischmann, "Birefringence free planar optical waveguide made by flame hydrolysis deposition (FHD) through tailoring of the overcladding", IEEE J. Lightwave Technol., vol. 18, no. 2, pp. 193-198, 2000.

3.4. T. Goh, M. Yasu, K. Hattori, A. Himeno, M. Okuno, and Y. Ohmori, "Low loss and high extinction ratio strictly nonblocking 16x16 themooptic matrix switch on 6-in wafer using silica-based planar lightwave circuit technology", IEEE J. Lightwave Technol., vol. 19, no. 3, pp. 371-379, 2001.

3.5. I. Ogawa, F. Ebisawa, F. Hanawa, T. Hashimoto, M. Yanagisawa, K. Shuto, T. Ohyama, Y. Yamada, Y. Akahori, A. Himeno, K. Kato, N. Yoshimoto, and Y. Tohmori, "Hybrid integrated four-channel SS-SOA array module using planar lightwave circuit platform", Electron. Lett., vol. 34, no. 4, pp. 361-363, 1998.

3.6. M. Zirngibl and C. H. Joyner, "High performance, 12 frequency optical multichannel controller", Electron. Lett., vol. 30, no. 9, pp. 700-701, 1994.

3.7. F. Ebisawa, I. Ogawa, Y. Akahori, K. Takiguchi, Y. Tamura, T. Hashimoto, Y. Yamada, Y. Suzaki, N. Yoshimoto, Y. Tohmori, S. Mino, T. Ito, Y. Kawaguchi, A. Himeno, K. Kato, "High-speed 32-channel optical wavelength selector using PLC hybrid integration", Optical Fiber Communication Conference, 1999, and the International Conference on Integrated Optical Fiber Communication. OFC/IOOC'99, Technical Digest, vol. 3, pp. 18-20, 1999.

3.8. T. Ito, R. Sato, R. Kasahara, I. Ogawa, Y. Kawaguchi, Y. Inoue, Y. Kondo, Y. Tohmori, and Y. Suzuki, "Novel bit-rate-free and format-free PMD compensation with a differential group delay monitoring using a SOA/PLC hybrid wavelength converter", OFC'2002, Anaheim, CA, TuU5, pp. 142,

2002.

3.9. K. Habara, Y. Yamada, A. Misawa, K. Sasayama, M. Tsukada, T. Matsunaga, and K. Yukimatsu, "Demonstration of frequency-routing type photonic ATM switch (FRONTIER NET) prototype," European Conference on Optical Communication, ECOC'96, Oslo, Norway, post-deadline ThC.3.4, vol. 5-41, Sep. 1996.

3.10. K. Sasayama, K. Habara, W. De Zhong, and K. Yukimatsu, "Photonic ATM switch using frequency-routing-type time-division interconnection network," Electron. Lett., vol. 29, no. 20, pp.1778-1780, 1993.

3.11. F. Ebisawa, I. Ogawa, Y. Akahori, K. Takiguchi, Y. Tamura, T. Hashimoto, Y. Yamada, Y. Suzaki, N. Yoshimoto, Y. Tohmori, S. Mino, T. Ito, Y. Kawaguchi, A. Himeno, K. Kato, "High-speed 32-channel optical wavelength selector using PLC hybrid integration", Optical Fiber Communication Conference, 1999, and the International Conference on Integrated Optical Fiber Communication. OFC/IOOC'99, Technical Digest, vol. 3, pp. 18-20, 1999.

3.12. R. Sato, T. Ito, K. Magari, Y. Inoue, I. Ogawa, R. Kasahara, M. Okamoto, Y. Tohmori, Y. Suzuki, and N. Ishihara, "Low input power (-10 dBm) SOA-PLC hybrid integrated wavelength converter and its 8-slot equipment", European Conference on Optical Communication, 2001, ECOC'2001, Th.F.2.3, 2001.

3.13. Y. Shibata, N. Kikuchi, S. Oku, T. Ito, H. Okamoto, Y. Kawaguchi, Y. Suzuki, and Y. Kondo, "Monolithically integrated parallel amplifiers structure for filter-free wavelength conversion", the Indium Phosphide and Related Materials, Indium Phosphide and their Related Materials, IPRM2001, FB1-5, Nara, Japan, pp. 587-590, 2001.

3.14. J. Leuthold, C. H. Joyner, B. Mikkelsen, G. Raybon, J. L. Pleumeekers, B. I. Miller, K. Dreyer, and C. A. Burrus, "100 Gbit/s all-optical wavelength conversion with integrated SOA delayed-interference configuration", Electron. Lett., vol. 36, no. 13, pp. 1129-1130, 2000.

Chapter 4

Photonic subsystems using all-optical signal processing

Chapter 4 describes the goal of this work; photonic subsystems for near-future networks. Using hybrid integrated devices, simultaneous wavelength conversion from C-band to L-band and from equal-spacing WDM channel to unequal-spacing WDM channel was demonstrated. Bit-rate-independent and format-independent polarization mode dispersion (PMD) compensation using hybrid wavelength converter has been achieved for the first time. Full bit-rate conversion was successfully demonstrated using a monolithic integrated wavelength converter.

4.1. Simultaneous wavelength conversion from C- to L-band

4.1.1. Simultaneous wavelength conversion using FWM

The capacity of the long-haul WDM network is continuously growing. The progress in optical fiber amplifier technologies expands the carrier wavelength region of wavelength division multiplexing (WDM) transmission systems from the conventional C-band (1530-1570 nm) to the S-band (1490-1530 nm) or L-band (1570-1610 nm). Unequal channel spacing is used in Japan to avoid the four-wave mixing (FWM) in dispersion shift fiber (DSF), while equal channel spacing is used in US or Europe. Both a coarse WDM system of more than 400-GHz spacing and a dense system of 25-GHz spacing may be used in adjacent fibers. Simultaneous wavelength conversion of multi-WDM channels is expected to be a key technique for connecting such networks with different band or channel spacing.

Here, we present an efficient 4-channel simultaneous wavelength conversion from C-band to L-band WDM signals. A hybrid wavelength selector, which consists of polarization-insensitive SS-SOA gate arrays on a PLC platform and two PLC arrayed waveguide gratings (AWGs), is used as the four-wave mixer. Each wavelength conversion was achieved by using FWM in each SS-SOA gate. The spacing between the input WDM optical signal and the WDM pump light was set equal to the free-spectral-range (FSR) of the AWG.

Compared to the usual optical-electrical-optical (O/E/O)-conversion [4.1], our simultaneous wavelength conversion is format-independent, have a possibility to operate of more than 100 Gbit/s, and can be used as a wavelength dispersion compensator. Moreover, the total cost can be reduced using a multi-frequency laser [4.2] as a multi-wavelength pump source.

4.1.2. Experimental setup and result

The feasibility of the simultaneous wavelength conversion was evaluated using a system comprising four WDM-channels. Figure 4-1 shows the experimental setup. Four WDM signal lights in the 1550-nm band (which is in the first FSR of the wavelength selector) were modulated at 2.5 Gbit/s. Another four wavelengths in the 1560-nm band (which is in the second FSR) were multiplexed as pump lights using an AWG and a coupler. A fiber amplifier (FA) with a wavelength of 1530-1565 nm was used to compensate for the optical loss, and 4-pairs of signal and pump lights were fed into the wavelength selector. The input power of the signal and pump lights was 8 dBm and 10 dBm at the input of wavelength selector. The pump light had circular polarization to reduce the polarization dependence of the four-wave mixing (FWM). The signal and pump lights were demultiplexed at the first AWG of the wavelength selector. Each signal-and-pump pair was launched into the individual SS-SOA on the PLC platform. Channel 5-8 of the wavelength selector were used as four-wave mixers. Each SS-SOA operates as a wavelength converter using FWM. The injection currents of the SS-SOAs were 170 mA. The converted lights in the 1570-nm band (which is in the third FSR) were multiplexed at the second AWG of the wavelength selector. The optical output was enhanced using a FA with a wavelength of 1570-1600 nm, so that the input signal and pump lights could be cut. The spectrum and bit error rate were evaluated for the converted lights.

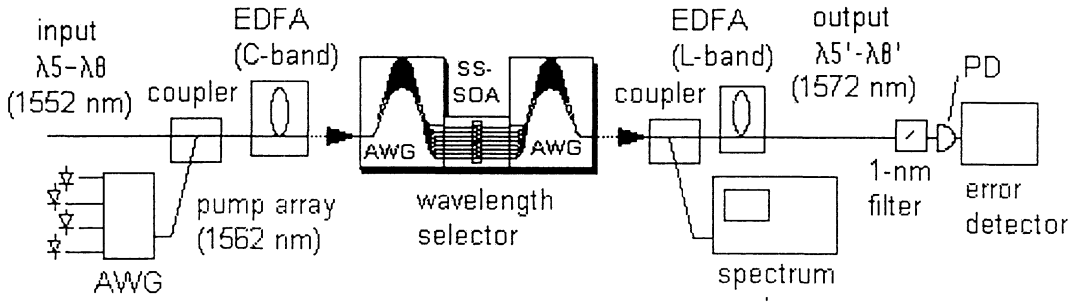

Figure 4-1 Experimental setup for simultaneous wavelength conversion

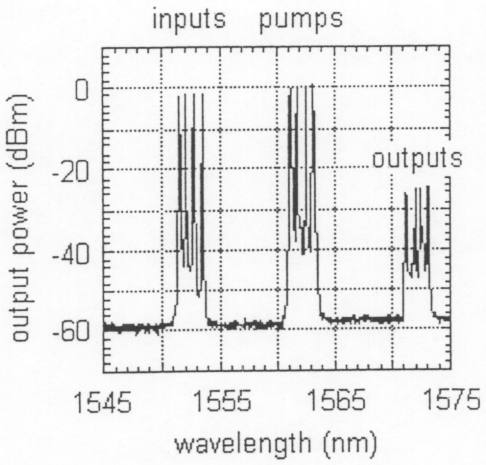

Figure 4-2 Optical spectrum of simultaneous wavelength conversion

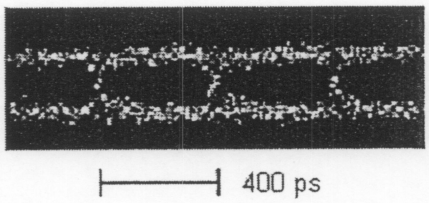

Figure 4-3 Eye pattern of a converter signal

Figure 4-2 shows the spectrum of the simultaneous wavelength conversion. Four converted lights were obtained with four signals and four pumps. The output power of the converted lights was about -25 dBm. Considering the coupling loss and transmission loss of the AWGs, the input power and conversion output power at the SS-SOA facets were about 0 and -17 dBm, respectively. The conversion efficiency of a SS-SOA, therefore, was -17 dB. The polarization dependence of the conversion was less than 1 dB. This small dependence is due to the low polarization sensitivity of the SS-SOA and AWG, and the circular polarization of the pump. Thus, we concluded that a WDM channel with conventional C-band can be converted to L-band.

Dynamic performance was measured at 2.5 Gbit/s. Figure 4-3 shows the eye patterns of the converted light. The eye openings are clear. Figure 4-4 shows the bit error rate (BER) characteristics for a typical input and four converted signals. Only a small power penalty of less than 0.5 dB was observed. The receiver sensitivity was -31 dBm at a BER of 10^{-9}. These results indicate that this simultaneous wavelength

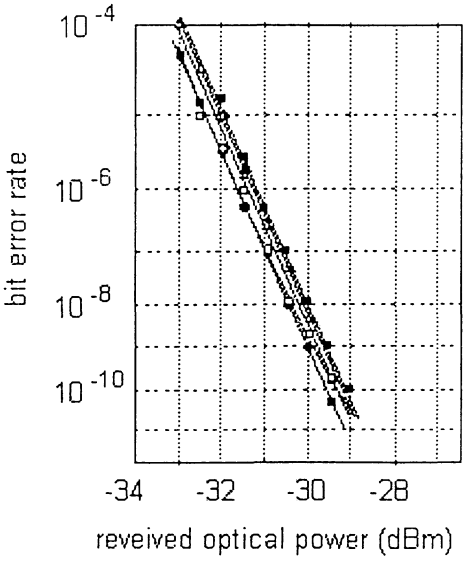

Figure 4-4 Bit error rate

conversion is a useful technique for WDM systems. It may also be used with much larger scale systems that have more (i.e., 16 or 32) WDM channels.

4.2. Simultaneous wavelength conversion from equal- to unequal-spacing

4.2.1. Simultaneous wavelength conversion using XGM

Several networks use equal channel spacing with conventional single-mode fibers [4.3], while others have adopted unequal channel spacing to avoid four-wave mixing (FWM) impairment over dispersion-shifted fiber (DSF) [4.4, 4.5]. Channel spacing of 25, 50, and 100 GHz has been utilized individually.

Simultaneous wavelength conversion of multi-WDM channels is expected to be a key technique for connecting networks with different bands or channel spacings. To solve the SNR and the level fluctuation problems, we introduced simultaneous wavelength conversion using a hybrid wavelength selector module, which consists of spot-size converter integrated semiconductor optical amplifier (SS-SOA) gate arrays

and two arrayed waveguide gratings (AWGs). Because the wavelength selector has an individual SS-SOA for each WDM channel, there is negligible interference between channels. It should be noted that our aim is not random wavelength switching but fixed wavelength conversion to connect different networks. This allows very easy operation and control, which is necessary for practical use. The optical power level of the converted signals can be controlled individually. However, the FWM technique, as mentioned in section 4.1, can not change the WDM channel spacing, for example from 100 to 50 GHz or from equal to unequal spacing, because of the complicated wavelength arrangement of WDM input signals, pumps, and converted signals.

Here, we present the first ever eight-channel simultaneous wavelength conversion from equal to unequal WDM channel spacing using input and output AWGs and a hybrid integrated SS-SOA array. The key device is the input AWG, which concurrently demultiplexes both the equal-spaced WDM signal and unequal-spaced pump lights to couple a pair comprising a signal and a pump. In the experiment, eight signal-and-pump pairs were launched into each SS-SOA, which operated as a cross gain modulation (XGM) device. The output AWG multiplexed only the converted unequal-spaced conjugated signal.

4.2.2. Experimental setup and results

To evaluate the feasibility of the simultaneous wavelength conversion, we demonstrate a system using eight WDM channels.

Figure 4-5 shows the experimental setup. Eight equally spaced WDM signal lights were modulated at 2.5 Gbit/s. Another eight lights with unequal spacing were used as pump lights. A fiber amplifier was used to compensate for the optical loss. The averaged input power of the equally spaced signal was 0 to +2 dBm at the output of the fiber amplifier. Note that a single input AWG demultiplexed both the signals and pumps, and each signal-and-pump pair was launched into each SS-SOA. It is true that the input AWG should be specially designed considering the wavelength of WDM signals and pumps [4.6], but here we used a conventional 50-GHz spacing AWG, because our

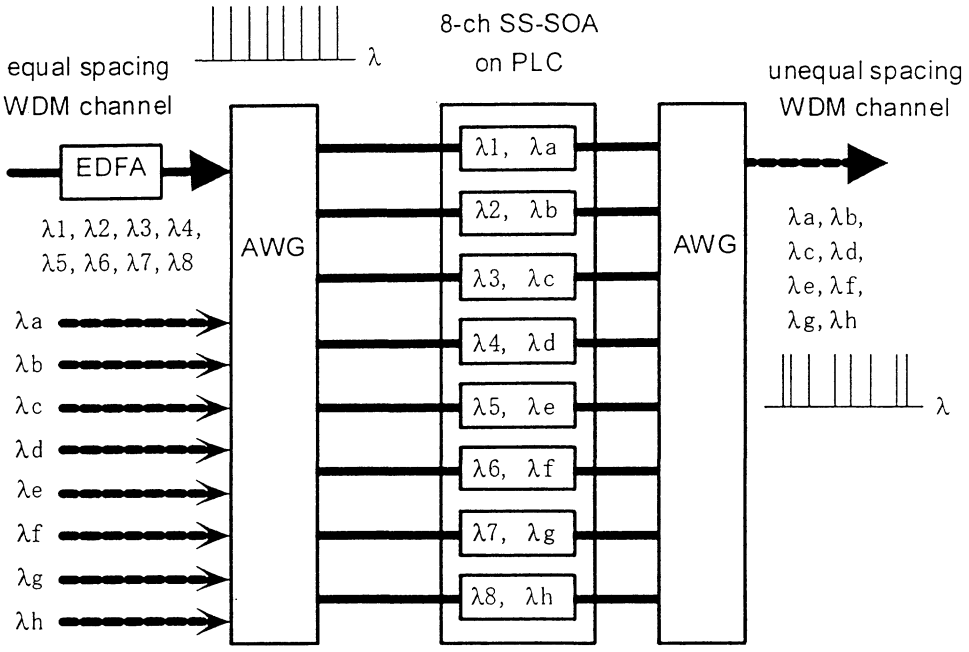

Figure 4-5 Experimental setup for simultaneous wavelength conversion From equal to unequal channel spacing

purpose here was simply to confirm the feasibility. The wavelength arrangement for the input AWG is shown in Table 4-1.

Two four-channel SS-SOA gate arrays were hybrid integrated on a PLC platform. Each SS-SOA operates as a wavelength converter using XGM. The injection currents of the SS-SOA range from 70 to 100 mA according to the wavelength dependence of XGM. The converted lights were multiplexed at the second output AWG. The spectrum and BER were evaluated for the converted lights.

Figure 4-6 shows the XGM characteristics of a SS-SOA. The horizontal axis is the signal power before the first

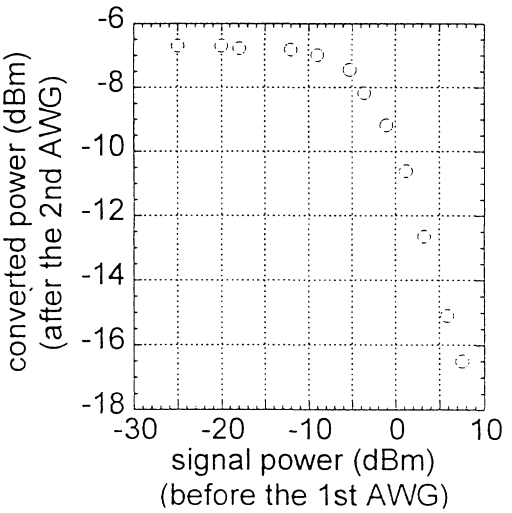

Figure 4-6 XGM characteristics

Table 4-1 Wavelength arrangement of the input AWG (nm)

in \ out	1	2	3	4	5	6	7	8
1	1545.8	-	-	-	-	-	-	-
2	-	1546.5	-	-	-	-	-	-
3	-	-	-	-	-	-	-	-
4	-	-	-	-	-	-	-	-
5	-	-	-	-	-	-	-	-
6	-	-	1548.1	-	-	-	-	-
7	-	-	-	-	-	-	-	-
8	-	-	-	1549.3	-	-	-	-
9	-	-	-	-	1550.1	-	-	-
10	-	-	-	-	-	-	-	-
11	-	-	-	-	-	-	-	-
12	-	-	-	-	-	1550.7	-	-
13	-	-	-	-	-	-	-	-
14	-	-	-	-	-	-	1552.9	-
15	-	-	-	-	-	-	-	1553.7
16	1551.3	1551.7	1551.7	1552.5	1552.9	1553.3	1553.7	1554.1

unequal spacing

equal spacing

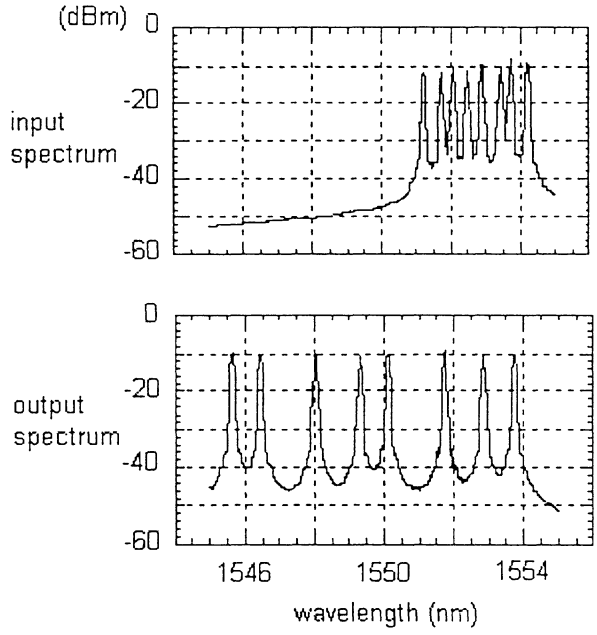

Figure 4-7 Input and output spectrum

AWG, and the vertical axis is the converted power after the second AWG. The optical loss was 15 dB, which is due to the loss of the AWGs. The extinction ratio was 10 dB.

Figure 4-7 shows the spectrum of the input and output WDM signals.

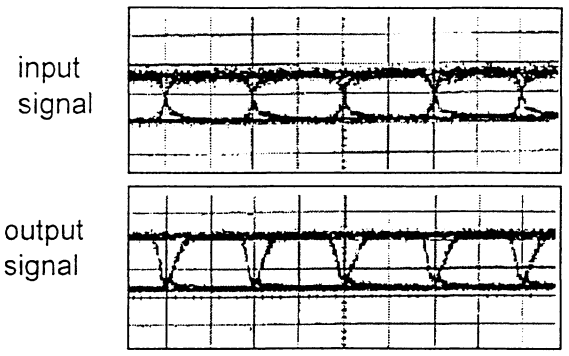

Figure 4-8 Eye patterns

Simultaneous wavelength conversion from equal to unequal spacing is successfully demonstrated. The polarization dependence of the conversion was less than 0.5 dB. This small dependence results from the low polarization sensitivity of SS-SOA and AWGs.

Dynamic performance was measured at 2.5 Gbit/s. Figure 4-8 shows the eye patterns of the converted light at the wavelength of 1550.1 nm. The eye openings are clear. Figure 4-9 shows the BER characteristics for eight converted signals. Only a small power penalty of less than 0.5 dB was observed. The receiver sensitivity was

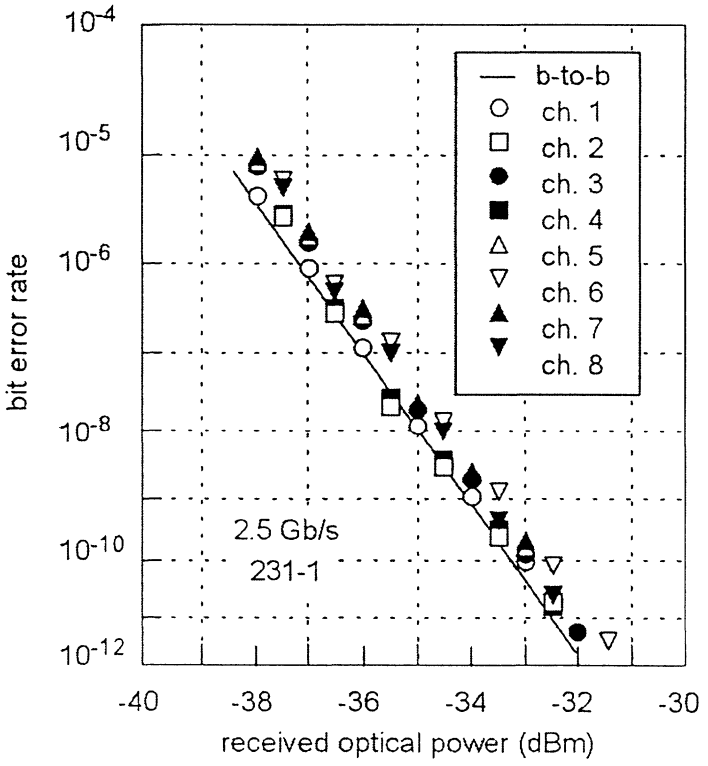

Figure 4-9 Bit error rate

-33 dBm at a BER of 10^{-9}. These results indicate that this simultaneous wavelength conversion is useful for channel-space shifting in WDM networks. It could also be used with much larger scale systems that have more (i.e., 16 or 32) WDM channels.

4.3. Full bit-rate conversion

4.3.1. Bit-rate conversion using SIPAS

Recent progress for upgrading the total throughput of the WDM system requires a high bit-rate of 10 Gbit/s WDM channels for metropolitan networks and an extremely high (> 40 Gbit/s) bit-rate for long-haul network. It should be noted that metropolitan networks usually use non-return-to-zero (NRZ) format, while long-haul networks are supposed to use return-to-zero (RZ) format.

A full bit-rate conversion from 10-Gb/s random WDM channels to a 40-Gb/s channel, including NRZ-to-RZ format conversion and reconversion, was successfully demonstrated. The key technique is wavelength conversion using a monolithic Sagnac Interferometer integrated with parallel-amplifier structure (SIPAS).

Another important procedure, phase adjustment procedure for 10-Gbit/s-to-40 -Gbit/s bit-rate conversion, was also successfully demonstrated, using slight wavelength conversions with a planar lightwave circuit (PLC) and semiconductor optical amplifier (SOA) hybrid integrated Mach-Zehnder Interferometer (MZI) and wavelength dispersion of an optical fiber.

4.3.2. Configuration for full bit-rate conversion

Figure 4-10 shows the configuration of the demonstration system. The key features are as follows.

I) NRZ/RZ and MUX

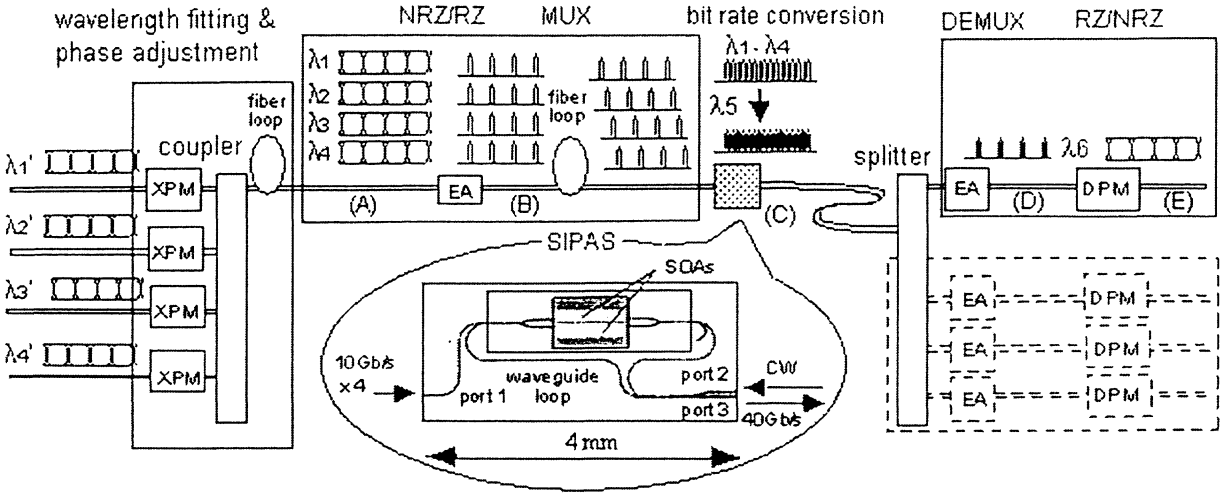

Figure 4-10 Experimental setup for full bit-rate conversion

Four 100-GHz spacing WDM channels of 10-Gb/s NRZ format (A) were launched into a polarization independent EA modulator [4.7] with 10-GHz sinusoidal modulation. The modulator simultaneously converted the four NRZ signals to RZ formats with a pulse width of 25 ps (B). A fiber loop was used to arrange the piled up RZ pulses into a serial bit stream. It should be noted that the bit stream was formed with a single modulator and a single fiber, which is a simple and extensible technique for stream forming. This technique can also be used in larger-scale WDM systems, ones with 8 or 16 channels, for example.

II) Wavelength fitting and phase adjustment

In confirming NRZ/RZ and MUX operation, there are two important issues: the channel spacing, which must be nearly equal, and the phase of the four WDM channels, which must be adjusted. Using a multi-channel XPM module, each input WDM channels was arranged to have an equally spaced fixed wavelength. Then a slight wavelength adjustment (ex., 0.1 nm) provided a phase shift at the fiber loop, which assured the phase adjustment at the EA modulator. A thermal tuning of the CW source achieved this phase adjustment.

III) Bit-rate conversion using SIPAS

For 40-Gb/s bit-rate conversion, four different wavelengths of the multiplexed bit stream were converted to a single wavelength by using a SIPAS with a gating window of less than 25 ps (C). Differential phase modulation (DPM) can compensate for the slow carrier recovery time of SOAs to achieve high-speed wavelength conversion. The SIPAS has a low wavelength dependency and offer the possibility of filter-less operation.

IV) DEMUX and RZ/NRZ

An EA modulator was also used to demultiplex the converted 40-Gb/s stream into the 10-Gb/s RZ format (D). Another DPM device with a gating window of 100 ps enlarged the pulse width, thus completing the 10-Gb/s RZ-to-NRZ reconversion (E).

4.3.3. Experimental results of full bit-rate conversion

Figure 4-11 shows the experimental setup. Four 10-Gb/s WDM channels were converted to equal spacing using a multi-channel PLC-SOA hybrid integrated MZI module. The CW and averaged signal powers of the XPMs were –2 to 2 dBm. A 10-MHz clock with a wavelength of 1310 nm was served, utilizing the unoccupied port of the XPM module. This clock is indispensable for the synchronization of bit rate conversion. The four converted signals were coupled to an optical fiber with a dispersion of 150 ps/nm. Therefore, a slight wavelength adjustment of less than 0.5 nm provides a phase shift of 75 ps. Four phase-adjusted WDM channels with 100-GHz spacing from 1552 to 1555 nm were launched into an EA modulator with 10-GHz 4V sinusoidal modulation (A, B). A second 2-km fiber loop with a total wavelength dispersion of -25 ps/100-GHz was used to arrange the piled up RZ pulses into a serial bit stream with a pulse width of 25 ps. A part of the bit stream was monitored and the converted wavelengths of the XPMs were controlled to the most suitable values.

10 to 40-Gb/s bit-rate conversion was done using DPM in a SIPAS. Four different wavelengths of the multiplexed bit stream were converted to a single

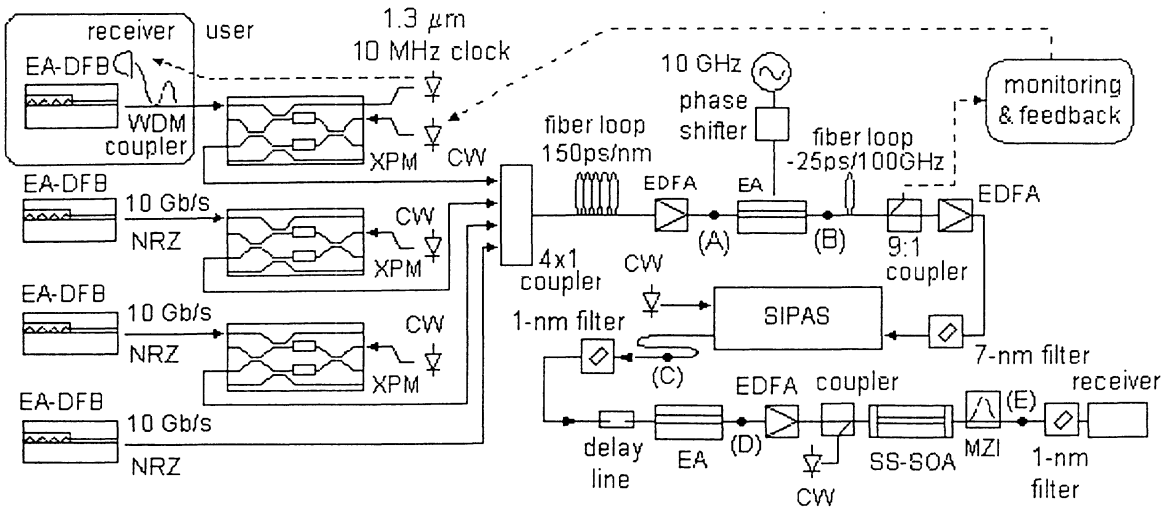

Figure 4-11 Experimental setup

wavelength, 1551 nm, by using the SIPAS with a gating window of less than 25 ps (C). The CW and averaged signal powers were about 10 dBm. The current of the SOAs was about 200 mA.

A second EA modulator was used to demultiplex the 40-Gbit/s stream into 10-Gbit/s RZ format (D). Another DPM device, which consists of a SS-SOA and a PLC asymmetric MZI with a gating window of 100 ps, enlarged the pulse width, thus completing 10-Gbit/s RZ to NRZ conversion (E). The input current of the SS-SOA was 80 mA. The CW and signal powers were about 0 dBm.

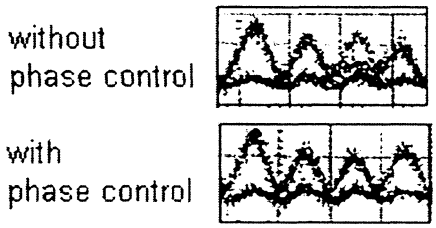

Figure 4-12 Optical signals with and without phase control

Figure 4-12 shows the 10-Gbit/s x 4 bit-stream signals before the SIPAS. By adjusting the wavelength of channel 3 by 0.1 nm (phase sift of 15 ps), it is possible to avoid the cross point of the NRZ signal. Figure 4-13 shows the eye patterns measured at points (A) to (E). Clear eye openings for NRZ-to-RZ conversion (B), 10 to 40-Gbit/s

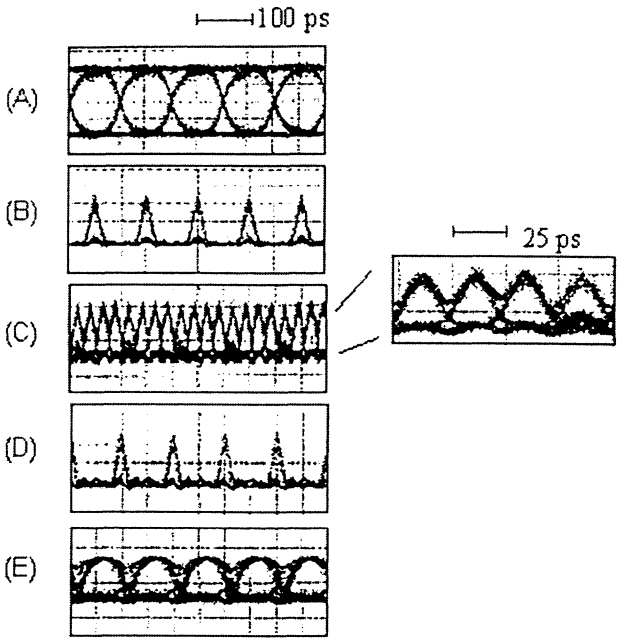

Figure 4-13 Eye patterns of the full-bit rate conversion

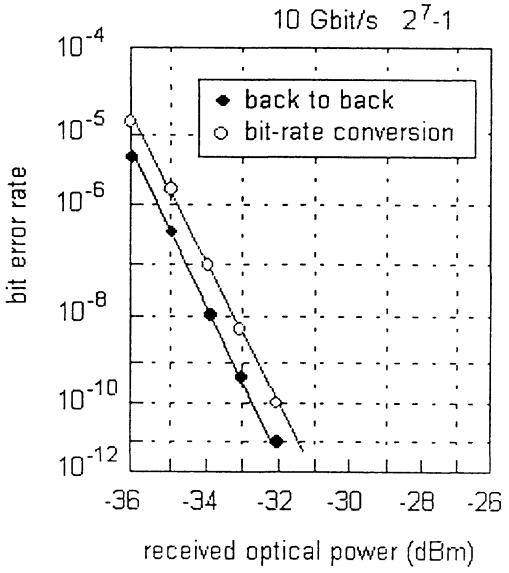

Figure 4-14 Bit error rate of the full-bit rate conversion

conversion (C), 40 to 10-Gb/s reconversion (D) and RZ to NRZ reconversion (E) were observed. Figure 4-14 shows the bit error rate from point (A) to (E). The receiver sensitivity at a bit rate of 10^{-9} was less than -32 dBm. Only a small power penalty of less than 0.8 dB was observed. These results indicate that the above techniques will be useful for future bit-rate conversion.

4.4. Polarization mode dispersion (PMD) compensation

4.4.1. PMD compensation

The explosive growth of data traffic has increased the bit-rate of WDM transmission systems to 40 Gbit/s or more, which reduces the dispersion margin of the bit train. Polarization mode dispersion (PMD), which is caused by the slight birefringence of the optical fiber, is an obstacle to upgrading long-haul transmission networks.

For monitoring the differential group delay (DGD), we proposed a novel technique that uses a semiconductor optical amplifier (SOA) and planar lightwave circuit (PLC) hybrid integrated wavelength converter (WC). Thanks to the XOR operation of the WC, this technique is bit-rate independent and format-independent.

4.4.2. DGD monitoring technique using a hybrid integrated wavelength converter

Figure 4-15(a) shows a schematic view of the hybrid integrated WC [4.8]. We employ PLC hybrid integration technologies, which are attractive for constructing optical modules with fiber array pigtails. The hybrid module consists of a PLC Mach-Zehnder interferometer and a 2-channel SOA with spot-size converters (SS-SOA). The polarization-insensitive 2-channel SS-SOA array is 1200 μm long x 800 μm wide with channel spacing of 400 μm. The SS-SOA consists of a 600-μm bulk active region (band-gap wavelength = 1.55 μm) and two 300-μm vertically tapered SS regions (band-gap wavelength = 1.3 μm at the facet). The stripe width is 0.5 μm. The SS-SOA

array was flip-chip bonded on the PLC platform, which is 30 x 3 x 1 mm^3 in size, using a passive alignment technique. The space between the SS-SOA and PLC's angled facet is 10-15 μm and the coupling loss is about 4 dB. The four-single-mode-fiber array was directly attached to both sides of the PLC using UV-curable adhesive. The built-in peltier device in the package precisely controls the module temperature.

The DGD monitoring technique is as follows. The input optical powers of the divided two polarization states (TE and TM) are fed to both arms of the hybrid integrated WC. The WC is normally set to the cross state. This minimizes the output power of the converted light at the bar port, which is the monitor port of the DGD. If a large DGD exists, the phase difference between the two arms results in switching of the

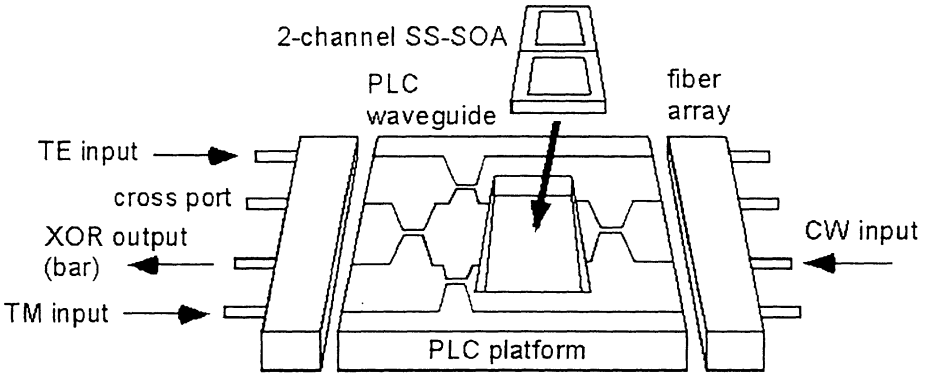

(a) Hybrid wavelength converter

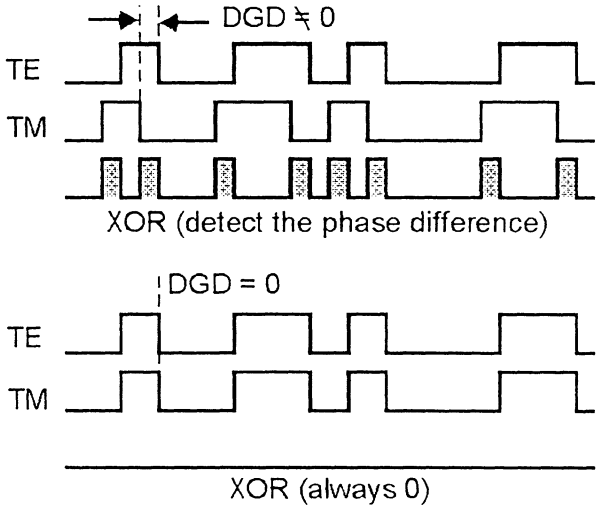

(b) XOR circuit using wavelength converter

Figure 4-15 Hybrid wavelength converter as an XOR circuit

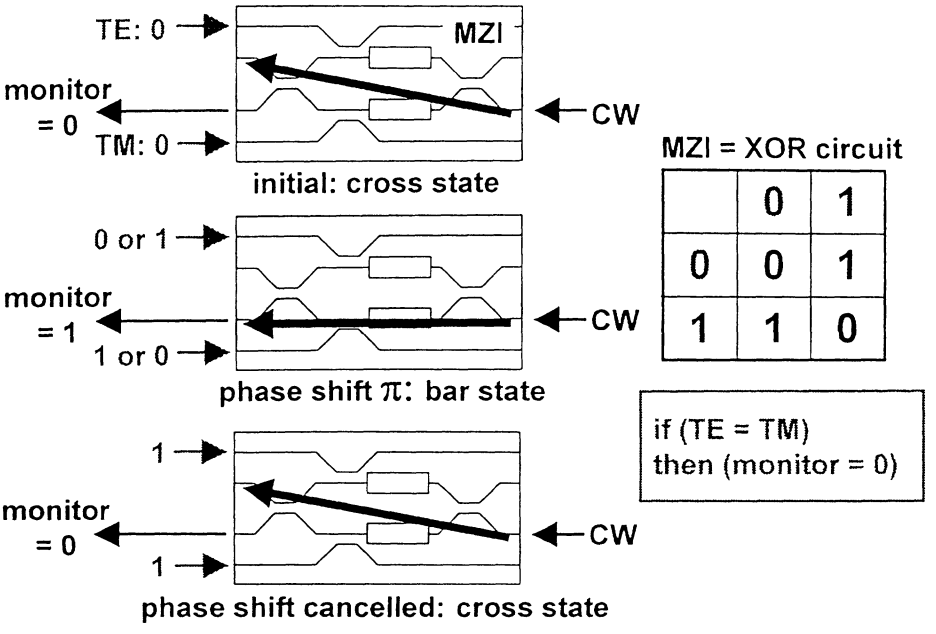

	0	1
0	0	1
1	1	0

Figure 4-16 Mach-Zehnder interferometer as an XOR circuit

converted light from the cross port to the monitor bar port, and the output power of the monitor bar port increases as shown in Fig. 4-15(b). A minimum output power means the value of DGD is also at the comfortable minimum state, which should be kept by controlling the PMD equalizer. As a result, the WC operates as an XOR circuit. The monitor port shows "0" when the input powers of the two arms are equal, while it shows "1" when they are unequal, as shown in Fig. 4-16. This circuit has a possibility to work at more than a 100 Gbit/s, because the push-pull switching mechanism (DPM: differential phase modulation) of the WC cancels the slow relaxation of the induced refractive index change [4.9].

4.4.3. Experimental setup and results for 20-40 Gbit/s input signals

Figure 4-17 shows the experimental setup for input signals of 20-40 Gbit/s. Three types of optical signals with wavelength of 1556 nm were used. A 40-Gbit/s RZ signal was formed using two polarization insensitive electroabsorbtion (EA) modulators and an optical multiplexer consisting of two couplers and optical delay lines. The

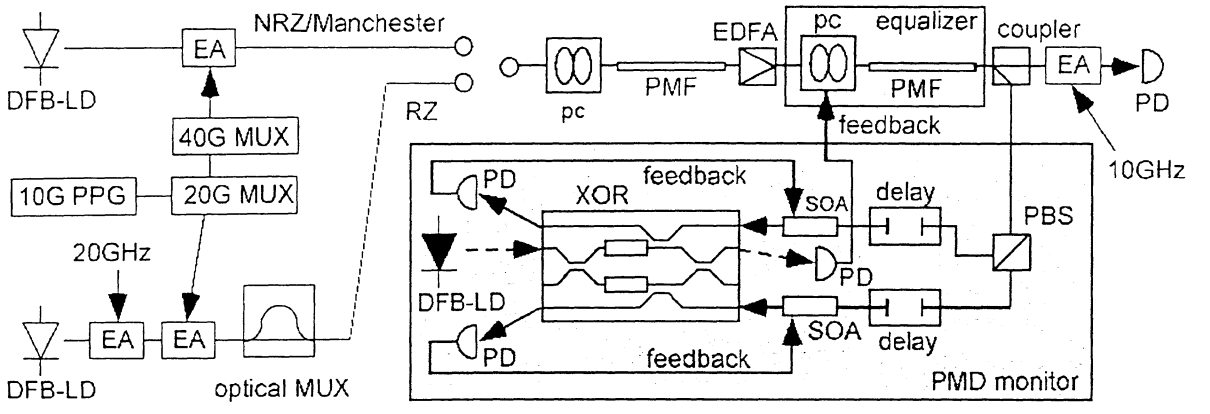

Figure 4-17 Experimental setup for 40 Gbit/s PMD compensation

40-Gbit/s NRZ signal and 20-Gbit/s Manchester signal were generated using an electrical multiplexer and a phase shifter. To emulate the waveform distortion caused by PMD, we prepared polarization-maintaining fiber (PMF) whose DGD between the fast and slow axis was about 30 ps. The power ratio between the two principal polarization states was changed from 0 to 10 dB, by adjusting the polarization controller (PC) before the PMF.

To equalize the PMD, a second PC and a PMF having a DGD of 28 ps were used. A part of the signal was divided for monitoring, and then the polarization states of the monitored signal were divided using a bulk polarization beam splitter (PBS) module. The optical powers of the divided two polarization states were equalized within 1 dB using the SOAs and fed to both arms of the hybrid integrated wavelength converter. The optical lengths between the PBS and the arms of the wavelength converter were adjusted to be equal using optical delay lines. Of course, this adjustment of optical length can be achieved easily if the integrated PLC-PBS is used. The wavelength converter has input power monitor ports with power meters, which make it possible to adjust the optical power of both arms.

A DFB laser with a wavelength of 1552 nm was used for the optical source of the WC. With the SS-SOA current biases of 80 and 82.5 mA, the WC was normally set to the cross state. The WC operates as an XOR circuit. The output power from the XOR circuit (bar port) was minimized by controlling the PMD equalizer. The optical signal,

after PMD compensation, was optically demultiplexed to 10-Gbit/s RZ format using an EA modulator, and the BER was evaluated.

Figure 4-18(a) shows the eye patterns for the 40-Gbit/s RZ, 40-Gbit/s NRZ and 20-Gbit/s Manchester signals. Though large waveform distortions were observed before the PMD compensation, a clear eye pattern was observed after the compensation. Figure 4-18(b) shows the BER of the PMD compensation of 40-Gbit/s RZ and NRZ formats. The minimum received optical power at 10^{-9} was -33 dBm, and the power penalty for both formats was less than 0.8 dB. These results confirm bit-rate independent and

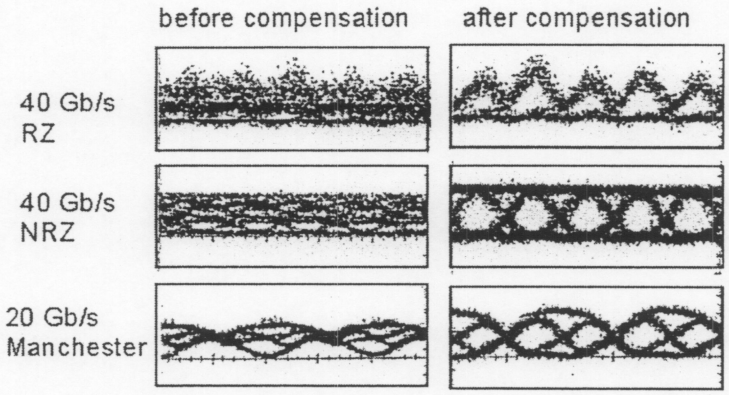

(a) Eye patterns

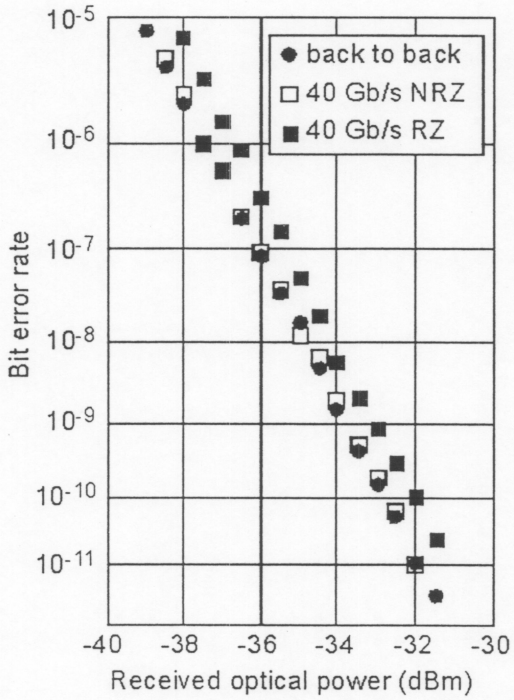

(b) Bit error rate

Figure 4-18 PMD compensation at 40 Gbit/s

format independent PMD compensation using the hybrid integrated wavelength converter.

4.4.4. Experimental setup and results for 80 Gbit/s input signal

The data signal was prepared using a 1555-nm optical pulse stream generated by a fiber mode-lock laser with a repetation rate of 9.95328 GHz. The pulse width was 5

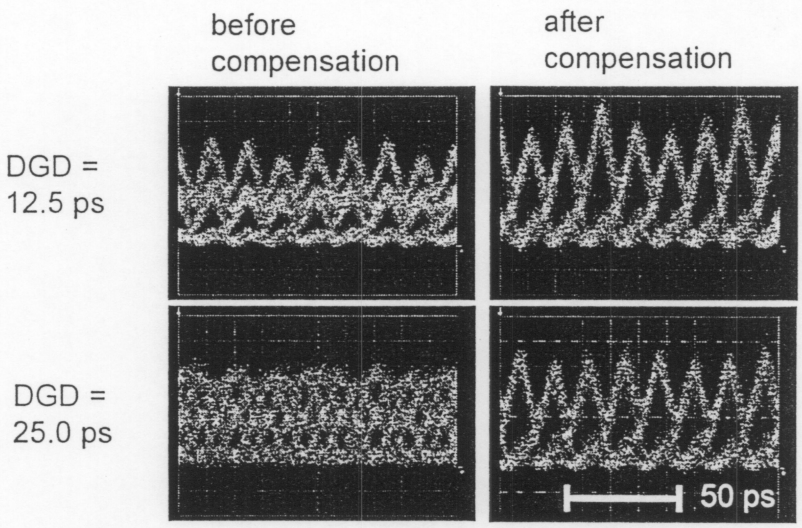

(a) Eye patterns before and after the PMD compensation

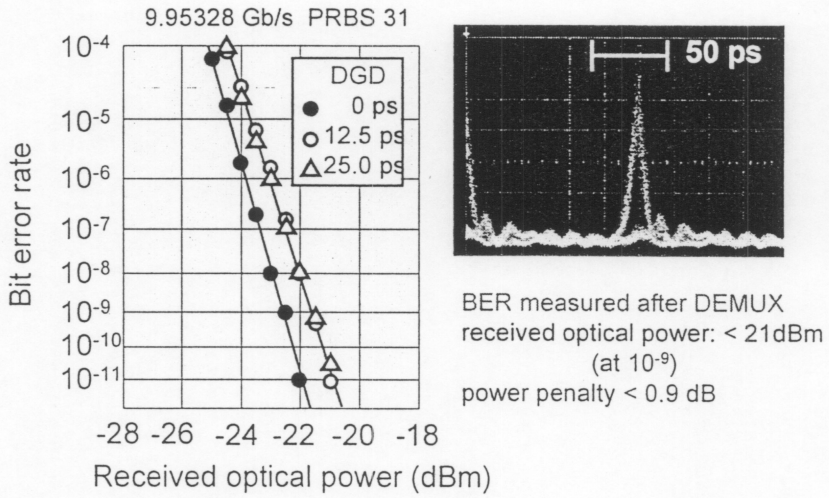

(b) Bit error rate

Figure 4-19 Experimental results for a 80 Gbit/s signal

ps. An 80 Gbit/s signal was formed using $LiNbO_3$ modulator and optical MUX circuit. To emulate the PMD waveform distortion, we used polarization-maintaining fibers (PMFs) whose DGDs between the fast and slow axis were 12.5 and 25.0 ps.

To equalize the PMD, a second polarization controller and a variable DGD generator were used. The optical signal, after PMD compensation, was optically DEMUX to 10 Gbit/s using the SIPAS, and the BER was evaluated.

Figure 4-19(a) shows the eye patterns for 80 Gbit/s, with DGDs of 12.5 ps and 25.0 ps. Though large waveform distortions were observed before the PMD compensation, a clear eye pattern was observed after the compensation. Figure 4-19(b) shows the BER at 10 Gbit/s. The minimum received optical power at 10^{-9} was -21 dBm, and the power penalties were less than 0.9 dB. These results confirm the high bit-rate operation of the all-optical XOR circuit.

4.5. Summary of Chapter 4

Chapter 4 describes photonic subsystems for upgrading transmission networks.

First, we introduce simultaneous wavelength conversion using a hybrid wavelength selector module that consists of SS-SOA gate arrays and two PLC-AWGs. Because the wavelength selector has an individual SS-SOA for wavelength conversion of each WDM channel, there is negligible interference between channels. The optical power level, and the WDM channel spacing of the converted signals can be controlled individually. It should be noted that our aim is not random wavelength switching but fixed wavelength conversion to connect different networks. This will allow very easy operation and control, which are necessary for practical use.

We demonstrated, for the first time, simultaneous wavelength conversion from C-band to L-band using four-wave mixing (FWM) in a wavelength selector [1.60]. Another type of simultaneous wavelength conversion, from equal to unequal channel spacing, was demonstrated using cross-gain modulation (XGM) in a wavelength selector.

Then we demonstrated full 40-Gbit/s all-optical bit-rate conversion. A SIPAS

was utilized for the conversion. A clear eye opening, error-free operation, and low power penalty were observed throughout the 10-to-40-to-10-Gbit/s and NRZ-to-RZ-to-NRZ conversion.

Lastly we have proposed a novel technique in monitoring the state of the differential group delay (DGD) of an optical fiber, using a hybrid integrated wavelength converter. Thanks to the XOR operation of the wavelength conversion, this technique is bit-rate-independent and format-independent. Using this monitoring technique, compensation of polarization mode dispersion (PMD) was successfully demonstrated. It has the possibility to work even for input signal of more than a 100-Gbit/s as well as for high-speed burst signal. The hybrid integration is very attractive because the PLC can easily implement a polarization beam splitter (PBS), one of the key components for PMD compensation.

By monitoring the output power from the wavelength converter, the PMDs of 40-Gbit/s and 80-Gbit/s RZ format, 40-Gbit/s NRZ format, and 20-Gbit/s Manchester format were successfully compensated. Only a small power penalty of less than 0.8 dB was evaluated.

These subsystems in Chapter 4 successfully demonstrate a direct connection between different optical networks and provide high bit rates and bit-rate transparency. Furthermore, they have the possibility to be used in future commercial networks, because no complex control circuits are needed.

.

Reference in Chapter 4

4.1. K. Inoue, and M. Jinno, "Signal improvement effect in O/E-E/O conversion using an electro-absorption (EA) modulator," IEEE Photon. Technol. Lett., vol. 9, pp. 109-111, 1997.

4.2. M. Zirngibl, C. H. Joyner, C. R. Doerr, L. W. Stulz, and H. M. Presby, "An 18-channel multifrequency laser," IEEE Photon. Technol. Lett., vol. 8, pp. 870-872, 1996.

4.3. A. K. Srivastava, D. L. Tzeng, A. J. Strentz, J. E. Johnson, M. L. Pearsall, O. Mizuhara, T. A. Strasser, K. F. Dreyer, J. W. Sulhoff, L. Zhang, P. D. Yeates, J. R. Pedrazzani, A. M. Sergent, R. E. Tench, J. M. Freund, T. V. Nguyen, H. Manar, Y. Sun, C. Wolf, M. M. Choy, R. M. Kummer, D. Kalish, and A. R. Chrapilyvy, "High-speed WDM transmission in allwave^{TM} fiber in both the 1.4-μm and 1.55-μm bands," Proc. 9th Opt. Amp. and their Applications (OAA), Vail, Colorado, post deadline paper, PD 2, 1998.

4.4. T. Sakamoto, K. Hattori, M. Fukutoku, M. Fukui, M. Jinno, and K. Oguchi, "Properties of gain-shifted EDFA (1580 nm-band EDFA) cascades in WDM transmission systems," Proc. 9th Opt. Amp. and their Applications (OAA), Vail, Colorado, TuB3, pp. 88-91, 1998.

4.5. F. Forghieri, R. W. Tkach, A. R. Chraplyvy, and D. Marcue, "Reduction of four-wave mixing crosstalk in WDM systems using unequally spaced channels," IEEE Photon. Technol. Lett., vol. 6, pp.754-756, 1994.

4.6. ITU-T Recommendation G.692, "Optical interfaces for multichannel systems with optical amplifiers," Appendix V.2, V.3, Oct. 1998.

4.7. K. Tsuzuki, Y. Kawaguchi, S. Kondo, Y. Noguchi, N. Yoshimoto, H. Takeuchi, M. Hosoya, and M. Yanagibashi, "Four-channel arrayed polarization independent EA modulator with an IPF carrier operating at 10 Gb/s", IEEE Photon. Technol. Lett., vol. 12, no. 3, pp. 281-283, 2000.

4.8. R. Sato, T. Ito, K. Magari, Y. Inoue, I. Ogawa, R. Kasahara, M. Okamoto, Y. Tohmori, Y. Suzuki, and N. Ishihara, "Low input power (-10 dBm) SOA-PLC

hybrid integrated wavelength converter and its 8-slot equipment", European Conference on Optical Communication, 2001, ECOC'2001, Th.F.2.3, 2001.

4.9. J. Leuthold, C. H. Joyner, B. Mikkelsen, G. Raybon, J. L. Pleumeekers, B. I. Miller, K. Dreyer, and C. A. Burrus, "100-Gbit/s all-optical wavelength conversion with integrated SOA delayed-interference configuration", Electron. Lett., vol. 36, no. 12, pp. 1129 –1130, 2000.

Chapter 5

Conclusion

Semiconductor optical amplifier (SOA) based wavelength conversion is the most promising for those subsystems, because the all-optical wavelength conversion has advantages of bit-rate transparency and high-speed operation. Therefore, the design and characteristics of SOA must be studied carefully.

(1) The SOA described in Chapter 2 has an extremely low fiber-to-fiber lossless current of 5.4 mA at a 1580 nm input, because of its small square bulk active region of 0.3 μm (thickness) × 0.3 μm (width). This operation current is lower than that of any SOAs so far reported.

(2) The scattering of the polarization dependence gain, which is due to the unintended stain in the active layer, is within 0.5 dB, while the scattering in conventional SOA is as large as 2.0-2.5 dB. This is because the buried structure reduces the amount of strain introducing to the square active layer.

(3) The monolithic integration of spot size converters at both the input and output ports of the SOA array gates is indispensable for connecting an SOA to planar lightwave circuit (PLC) waveguide, because it enlarges the spot-size of SOA and keeps a large misalignment tolerance. A 4-channel polarization insensitive SOA integrated with spot-size converters (SS-SOA) gate array has been fabricated. The integrated spot-size converter utilizes a new butt-joint structure to optimize the bulk active layer

and the spot-size converter region individually.

(4) To reduce the evaluation cost of a SOA, the polarization characteristics must be measured before the module fabrication process, and, if possible, before the anti-reflection (AR) coating is applied. We have proposed a novel method of precisely measuring the polarization dependent gain of a SS-SOA. By averaging the signal gain over a wide wavelength range, the polarization dependence gain can be accurately estimated with low reflection from gain ripples. We successfully evaluated the polarization dependence gain of an angled-facet SS-SOA even before the AR coating process. The measurement error is within 0.5 dB, which is small enough to evaluate the chip characteristics.

(5) The polarization dependence in the coupling efficiency between a SS-SOA and optical fiber has also been evaluated by measuring the photo-current for TE and TM input signals. It is possible, therefore, to specify the polarization characteristics of the active region and spot-size converter region of a SS-SOA. The details of the switching time of the SS-SOA gate are also described. By using a speed-up condenser, the switching time including the turn-on delay time is reduce to less than 2.5 ns, which is fast enough for packet switching.

(6) Another type of SOA, with a 0.47 % tensile-strained MQW active region, has also been constructed. By controlling the peak wavelength of the amplified spontaneous emission (ASE) to be 1520 nm at the lossless operating current, we achieved polarization independence for a signal wavelength between 1530 and 1580 nm. This is, to our knowledge, the largest wavelength range as an SOA with tensile-strained active layer. The fabricated MQW-SOA has low polarization dependence of 0.3 dB, which remains unchanged over driving currents between 30 and 60 mA and mesa stripe width between 1.0 and 1.75 μm.

Chapter 3 discusses hybrid integration of SS-SOA and planar lightwave circuit (PLC). The hybrid integration is considered to be an attractive way to fabricate practical modules with functional PLC waveguides, such as couplers or arrayed waveguide gratings (AWGs). Moreover, it is easy to connect PLC waveguides to fiber

arrays.

(7) A 4-channel SS-SOA gate array was assembled on a PLC platform for the first time. It has an extinction ratio higher than 35 dB, operating at less than 50 mA. The polarization dependence is less than 1 dB throughout an ultra-wide-band of 1530-1600 nm. The spot-size conversion structure of the SS-SOA reduces the coupling loss to about 4 dB and improves the 1-dB down tolerance to better than 2 and 20 μm for the horizontal and axial directions, respectively. These large tolerances are essential for suppressing the coupling loss variation among channels.

(8) We demonstrated the first 4-channel high-speed wavelength selector with a combination of two modules: an SS-SOA hybrid gate array module and a PLC-AWG. It can be used in a practical system because polarization independent and ultra-wide-band (1530-1600 nm) operations were proven. The rise- and fall-times were less than 1 ns, which make the wavelength selector suitable for packet switching.

(9) In the part of chapter 3, Sagnac interferometer integrated with parallel-amplifier structure (SIPAS), is described. The SIPAS is fabricated monolithically by butt-coupling the passive high-mesa waveguide and buried active layer. It enables a fast wavelength conversion and filterless operation.

Chapter 4 describes photonic subsystems for upgrading transmission networks.

(10) We introduce simultaneous wavelength conversion using a hybrid wavelength selector module that consists of SS-SOA gate arrays and two PLC-AWGs. Because the wavelength selector has an individual SS-SOA for wavelength conversion of each WDM channel, there is negligible interference between channels. We demonstrated, for the first time, simultaneous wavelength conversion from C-band to L-band using four-wave mixing (FWM) in a wavelength selector.

(11) Another type of simultaneous wavelength conversion, from equal to unequal channel spacing, was demonstrated using cross-gain modulation (XGM) in a wavelength selector.

(12) Then we demonstrated full 40-Gbit/s all-optical bit-rate conversion. A SIPAS

was utilized for the conversion. A clear eye opening, error-free operation, and low power penalty were observed throughout the 10-to-40-to-10-Gbit/s and NRZ-to-RZ-to-NRZ conversion.

(13) Lastly we have proposed a novel technique in monitoring the state of the differential group delay (DGD) of an optical fiber, using a hybrid integrated wavelength converter. Thanks to the XOR operation of the wavelength conversion, this technique is bit-rate-independent and format-independent. By monitoring the output power from the wavelength converter, the PMDs of 40-Gbit/s and 80-Gbit/s RZ format, 40-Gbit/s NRZ format, and 20-Gbit/s Manchester format were successfully compensated [1.64, 1.65]. Only a small power penalty of less than 0.8 dB was evaluated.

By using these SOA based subsystems, it is possible to replace conventional electrical ones. As the SOA based wavelength converters have superior characteristics of bit-rate and format transparencies, they are the key technologies in upgrading the capacity and flexibility in the future WDM networks, which accommodate the increasing numbers of broadband subscribers.

Appendix

Photonic inter-module connector

A Photonic inter-module connector (PIMC) for near-future electronic communications switching systems is demonstrated through the use of PLC 8 x 8 switches [1]. A small switch matrix is sufficient because those systems will consist of a limited number of electronic modules. If an active module is fails, a stand-by module must quickly take its place. The experimental PIMC can switch 156-Mbit/s photonic interconnections between seven subscriber-line-concentrator modules and eight circuit-switching modules [2].

A.1. Introduction

Near-future electronic switching systems are expected to accommodate an increasing number of subscribers, satisfy demands for high-quality services, and fulfill requests for improved reliability. These systems will be made up of several function blocks, or modules, interconnected via optical interfaces [3, 4]. Multi-module schemes are advantageous because if an active module fails, is can be easily replaced with a stand-by module by switching the inter-module connector.

A photonic inter-module connector (PIMC) that uses optical switches for the interconnection, offers simple system construction, reduces hardware, and eliminates O/E or E/O conversion. Small-scale space-division (SD) optical switches are sufficient as PIMCs, because the number of modules is limited.

Optical switching systems are currently being developed, and a great deal of

the effort is focusing on developing large-scale polarization-independent optical switching devices having low loss and low crosstalk [5, 6].

Silica-based PLC waveguide switches have been fabricated [7]. An experimental 8-line photonic space-division switching system has been demonstrated using this optical switch [8]. The PLC switch was experimentally confirmed to have a number of advantages, such as low loss, low cosstalk, and long-term stability. Therefore, this switch is one of the most probable candidates for the switching device in the PIMC.

An experimental PIMC using crossbar type 8x8 optical switch is described. Each switch consists of 64 switching elements. The experimental PIMC can switch 155.52 Mbit/s inter-module connections through these optical switches.

A.2. Photonic inter-module connector

Figure A-1 shows the expected role of the PIMC in a future switching system comprising several modules such as subscriber-line-concentrator modules and circuit-switching modules. Each module is duplicated to provide quick recovery from a minor fault or accident. In addition, a common stand-by circuit-switching module is provided for serious faults, when both the affected module and its duplicate are damaged, and require a long recovery time.

The PIMC, which is located between the duplicated subscriber-line-

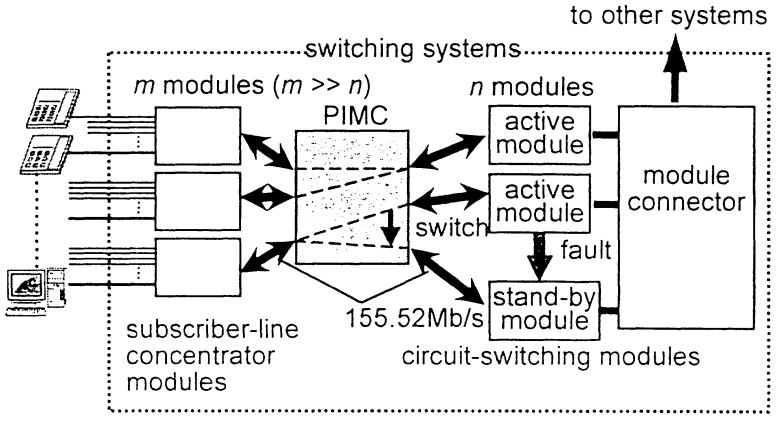

Figure A-1 Configuration including a PIMC

concentrator modules and the duplicated circuit-switching modules, can quickly aid in the recovery of serious module failure by changing the path from the affected module to the stand-by circuit-switching module. The switching of the PIMC path is controlled by the maintenance commands sent from the console.

This system can,

1) reduce the recovery time for a fatal fault, and

2) diagnose and repair a faulty circuit-switching modules without affecting the other active circuits.

Furthermore, by using optical switching, the PIMC can

3) reduce the complexity in system design and amount of hardware by eliminating the need for E/O and O/E convertors, and

4) accommodate the rising module interface bit-rate, because the optical switch matrix is not sensitive to bit-rate transparency.

Table A-1 shows the difference between a photonic and an electronic inter-module connector. The optical interface was a 155.52 Mbit/s Synchronous Digital Hierarchy (SDH) interface [9, 10]. Because of the loss of the optical switches, the PIMC needed some loss margin, unlike the electronic connector, for the interconnection. Therefore, we used a higher-powered output light and more sensitive detectors for the PIMC than for the electronic connector.

The PIMC does not have SDH endpoint termination. Therefore, the system can not diagnose the section overhead of the SDH interface, which the electronic connector

Table A-1 Difference between electronics inter-module connector and PIMC

	electronic inter-module connector	PIMC
SDH interface	no loss margin required	loss margin required
	fault detection by diagnosing the section overhead of the SDH interface	fault detection by monitoring the input / output light power
bit rate (Mbit/s)	51.84 and 155.52	155.52
switching type	space division and time division	space division

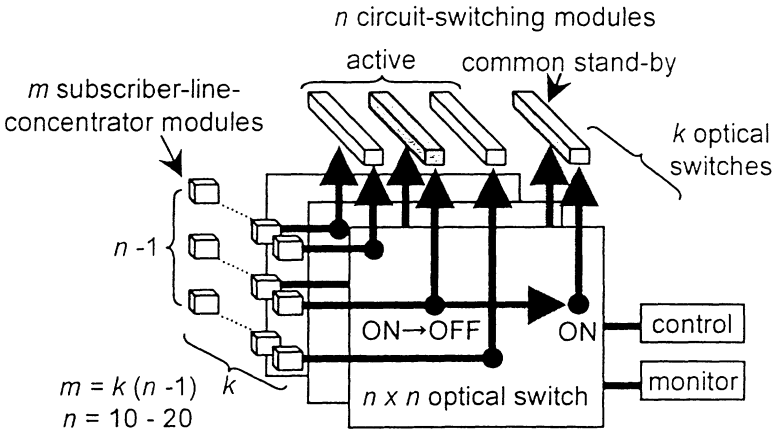

Figure A-2 Shematic of a PIMC in a future system

uses to detect the interface trouble (such as fiber breakage) and the breakdown of the inter-module connector itself. So, it is indispensable for the PIMC to be able to monitor the input/ output signal light powers to detect such faults.

The switching time of an optical switch is about 1.0 ms [11]. The PIMC paths are changed by commands from the maintenance system. This change takes a lot of time (more than several minutes) because the stand-by module requires software (e.g. subscriber information) loading. Therefore, the switching speed of the optical switch is sufficient. Because of the relatively slow switching, the PIMC cannot switch through time-division switching like an electronic system, but instead switches between fibers through SD switching.

Figure A-2 shows a schematic of a PIMC in a future system, where, m, n, and k are the number of subscriber-line-concentrator modules, circuit-switching modules, and optical switches, respectively. Each module and switch is duplicated to safeguard against fatal system error (thus, the real number of modules and switches are $2m$, $2n$, and $2k$). The n is assumed to be limited, to say 10-20, and m is assumed to be more than 100. Then, $k = m/(n-1)$. By using n x n optical switches, all subscriber-line-concentrator modules can select any circuit-switching module, including the common stand-by circuit-switching module. Therefore, a small-scale (10-20) matrix switch is sufficient for such practical systems.

As stated above, the PIMC can be constructed with relatively small, and slow optical switches. It will therefore probably be the first photonic switching application introduced into commercial switching systems.

A.3. Experimental system

A.3.1. General configuration

Figure A-3 shows the configuration of an experimental PIMC, which can switch duplicated circuit-switching modules to several active modules and one stand-by module by commands from the console.

The optical switches are silica-based 8x8 PLC thermo-optics (TO) matrix switches. Each module has an up-stream fiber and down- stream fiber, so one set of the duplicated modules has four fibers for the interconnection. One optical switch is used for each fiber, so the experimental PIMC has four optical switches, which move in parallel. Considering the number of input/output ports of the 8 x 8 switches, this system can maximally connect seven duplicated circuit-switching modules to seven active and one stand-by duplicated subscriber-line-concentrator modules.

A small part of each PIMC's input/output signal is divided and the optical powers are constantly monitored to detect faults. The control currents of the optical switches are also monitored to detect electrode breakage.

The console can display and control the set-up of the inter-module connections and the 64 cross points of each optical switch. The monitored light powers and electrode currents can also be displayed. Figure A-4 shows a photograph of the experimental PIMC. The rack consists of one optical monitoring package, four optical switch

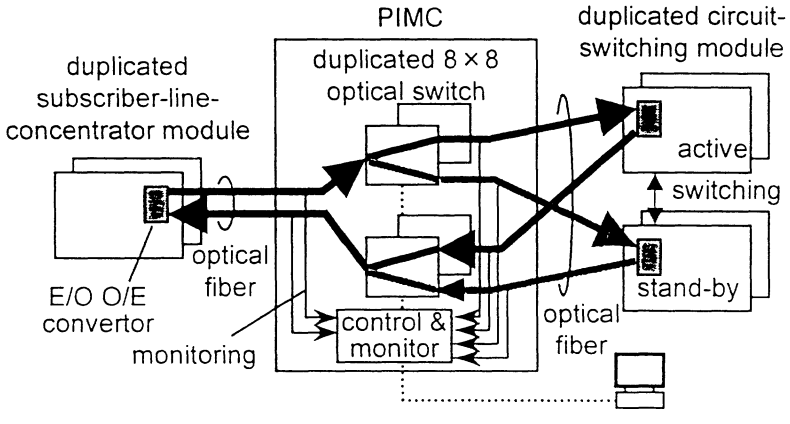

Figure A-3 Experimental PIMC

packages, four SDH-test packages with high output-power lasers and high-sensitivity detectors, and one power supply package.

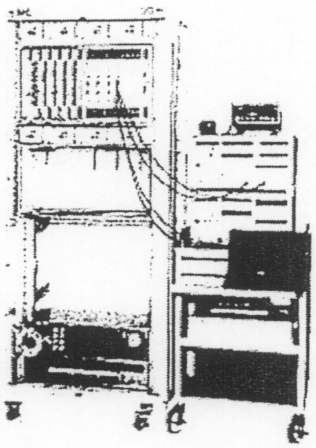

Figure A-4 Photograph of experimental PIMC

A.3.2. Adjustment of optical switches

The TO switch has a small polarization sensitivity [12] as well as wavelength sensitivity; both induce serious crosstalk problems. Polarization-insensitive operation, i.e., tolerance to indefinite polarization states in the input light, can be achieved by adjusting the bias and switching powers supplied to each switching element until the crosstalk reaches a minimum with unpolarized light. As the wavelength range of the optical interface is defined to be 1290-1330 nm, the heater current should be adjusted to the minimum crosstalk point for the unpolarized optical signal whose wavelength is 1310 (center of 1290-1330) nm. Therefore, we developed a compact (220 x 150 x 120 mm) fiber-optics depolarizer [13] with excellent mechanical stability.

The depolarizer, which is shown in Fig. A-5, consists of a half-wave-plate, two polarization beam splitters, a polarizer and a polarization-maintaining PANDA fiber [14]. The light passes through the half-wave-plate and is divided into P and S waves through the polarization beam splitter BS1. The S wave is launched into the

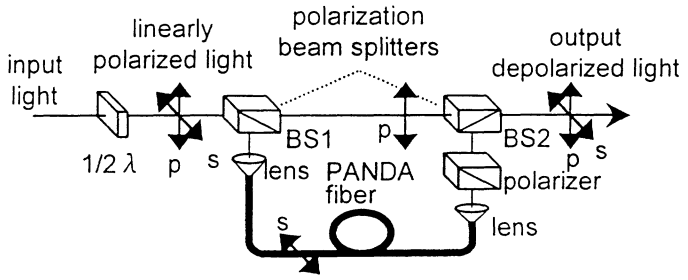

Figure A-5 Configuration of depolarizer

polarization-maintaining PANDA fiber, whose one principal axis is parallel to the polarization of the S wave. The output light from the PANDA fiber is then coupled orthogonally with the P wave at the second beam splitter BS2, after passing through the polarizer.

When the group-delay time difference, due to the length of the fiber delay line, is longer than the coherence time of the light, (1) the two waves are completely uncorrelated. And by adjusting the rotation angle of the half-wave-plate, (2) the two waves are incident with an equal power at the second beam splitter BS2. Therefore, the output from the depolarizer becomes a completely depolarized light. In fact, the experimental depolarizer can depolarize the outputs of DFB lasers to a degree of polarization of less than 0.03 at 1305 nm.

Figure A-6 shows the crosstalk of a TO switch element in the bar state versus

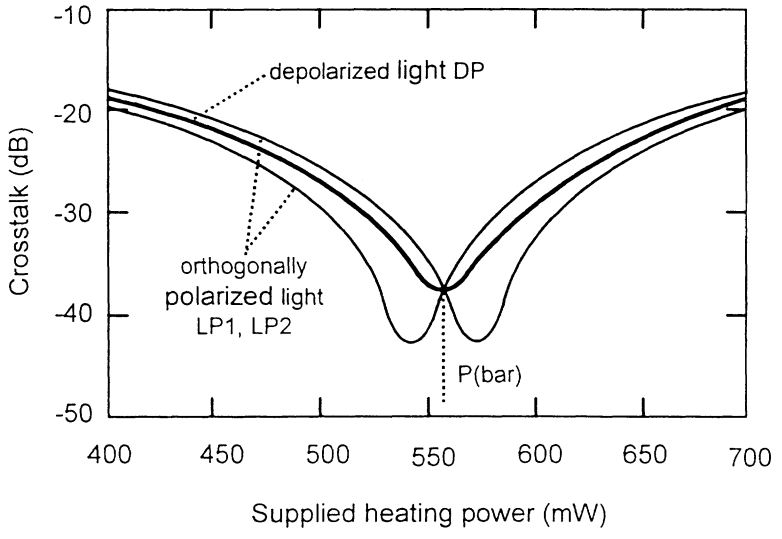

Figure A-6 Bar state crosstalk versus supplied heating power for different polarization states

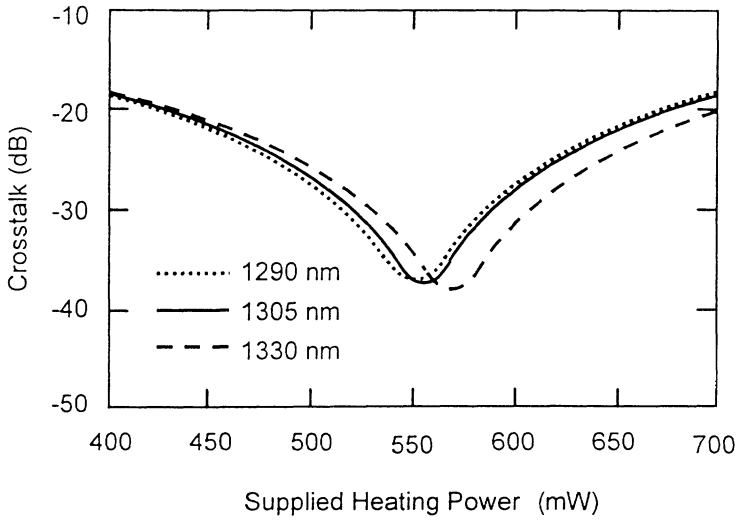

Figure A-7 Bar state crosstalk versus supplied heatingpower for different wavelengths

supplied heating power for different polarization states of a 1305-nm DFB laser light. When orthogonally polarized light waves were launched, the crosstalk was minimized at different supplied power due to anisotropic stress concentrations during heating, as shown by curves LP1 and LP2. The crossover point of these curves, i.e., the desired heating power in the bar state P(bar), occurs at the minimum point of curve DP which was obtained for depolarized light. The optimum heating power in the cross state, P(cross), was also determined.

Figure A-7 shows crosstalk in the bar state versus supplied heating power; these curves were obtained when depolarized light with a wavelength of 1290, 1305, or 1330 nm was launched into the switch. The wavelength sensitivity is caused mainly by the wavelength dependency of the 3-dB couplers in the MZ interferometer. By setting the heating power to P(bar) at 1305 nm, the crosstalk at both 1290 and 1330 nm differs by less than 0.7 dB from that at 1305 nm. Consequently, when lasers used in practical applications operate over a wide bandwidth, the optimum heating power for wavelength-insensitive operation can be found by using depolarized light at the central wavelength. Each of the 64 optical switch elements was adjusted to the optimum powers for both the cross and bar states, using these techniques.

The TO switch was mounted on a printed circuit board with drivers and control

logic circuits. The package is 280 x 330 x 50 mm. Figure A-8 shows a photograph of an optical switch package. Mounted on the package are a pigtailed 8 x 8 optical crossbar switch, SC connectors, an on-board power supply, and variable registors that adjust the heater powers.

A.3.3. Optical monitoring

For detection of faults in the SDH optical interface and the PIMC itself, input/output light power monitoring is indispensable. Therefore, a small part, -7 dB, of each signal light is split by a coupler, and the signal power is constantly monitored.

If both the input/output powers are detected, the system is assumed to be in a normal state. If neither power is detected, the input fiber or the front-side module, may be affected. If only the input power but not the output power is detected, the PIMC itself (maybe the optical switch) is affected by a fault.

In this experiment, we prepared only 12 silica-based wavelength-insensitive couplers [15], to allow the experimental PIMC to merely switch the path between a duplicated subscriber-line-concentrator module and two duplicated circuit-switching modules. The average, minimum and maximum insertion loss of the 12 couplers are 1.6, 1.3, and 2.0 dB, respectively.

Figure A-9 shows a photograph of an optical monitoring package. Mounted on this package are an optical switch control unit with a micro-processor, SC connectors,

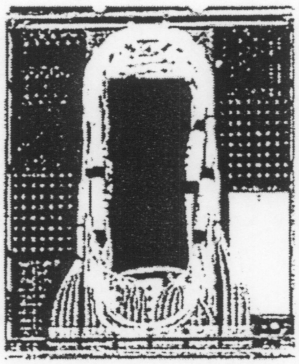

Figure A-8 Photograph of optical switch package

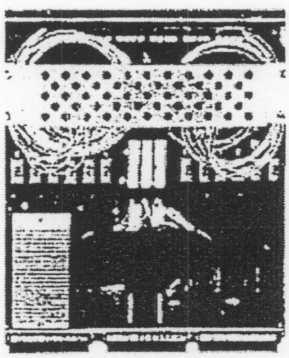

Figure A-9 Photograph of monitoring package

an on-board power supply, 12 silica-based wavelength insensitive couplers, and 12 monitor circuits. Each monitor circuit consists of a O/E convertor, a simple integrator and a comparator.

A.4. System performance

A.4.1. Bit error rate

The bit error rate of the employed optical interface is designed to be less than 10^{-11}, on condition that signal power SP=-32 dBm, and system crosstalk CT=-8 dB. These specifications should be evaluated by an experimental system incorporating several optical switches.

Figure A-10 shows an example of the bit error rates between a subscriber-line-concentrator module and a circuit-switching module, connected through a PIMC. The amount of cosstalk is adjusted by the attenuator. The signal powers satisfying the bit error rate of 10^{-11} are SP=-42.1 and SP=-41.7 dBm for CT=-∞ and CT=-8 dB, respectively. Therefore, the power penalty is 0.4 dB. The maximum and average power

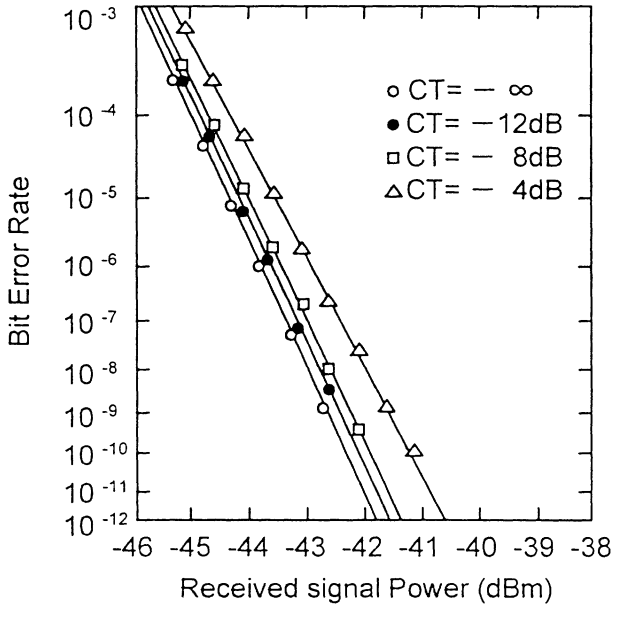

Figure A-10 Bit error rate

penalty were 1.4 and 0.8 dB for the four examples combined.

Figure A-11 shows the eye pattern of the PIMC output light for SP=-41.7 dBm and CT=-8 dB.

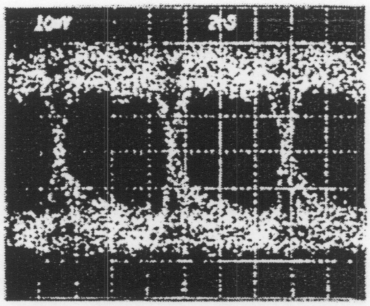

Figure A-11 Eye pattern

A.4.2. Multiple crosstalk

For an 8 x 8 switch, the multiple crosstalk, i.e., which is the crosstalk of the one port that received the crosstalks from the other seven paths, should be

(multiple crosstalk) = (crosstalk of a single element) + 10 $\log_{10}7$ (dB)

As the crosstalk of each element (Fig. A-6 or Fig. A-7) was less than -20 dB, the averaged multiple crosstalk of the optical switch is evaluated to be

CT = -20 + 10 $\log_{10}7$ = -11.5 (dB)

The multiple crosstalk will be enlarged by the loss difference between the switch elements and by the input light power difference.

The loss distribution of the optical switch was about 3 dB. Therefore, to satisfy the designed interface, which defined CT as -8 dB, the difference in the input power should be adjusted to within 0.5 dB by the attenuator placed at each input port.

Figure A-12 shows the loss-level diagram of a PIMC. The insertion loss is 22.5 dB when the average input optical power is 0 dBm. Considering the required minimum signal power of the designed interface, which is -32 dBm, the minimum loss margin is 9.5 dB.

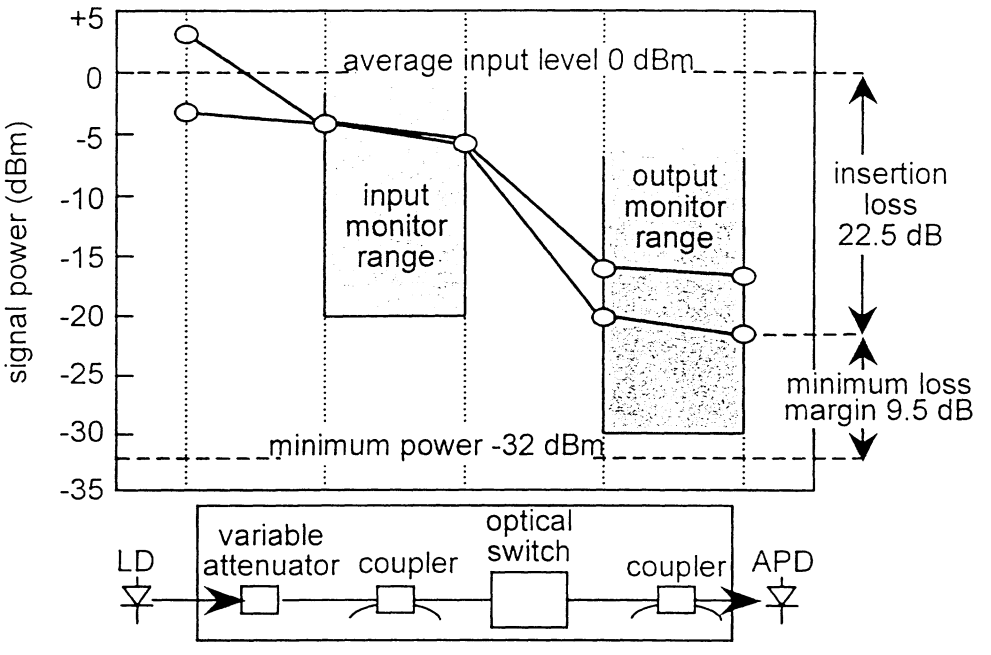

Figure A-12 Loss-level diagram of PIMC

The experimental optical monitoring packages could detect the input and output signal light of -20 and -30 dBm, respectively. As shown in Fig. A-12, these packages can successfully monitor the SDH interface. The lower monitoring limit of these packages each have an 8-15 dB margin from the signal powers. The lower limit of the output monitor range exceeds the condition of SP=-32 dBm by 2 dB.

A.5. Summary of appendix

As considered above, the PIMC can successfully connect subscriber-line-concentrator modules and circuit-switching modules with low loss and low crosstalk. The experimental system successfully demonstrated switching and monitoring between a duplicated subscriber-line-concentrator module and two duplicated circuit-switching modules, maintaining an error-free state.

References in appendix

(1) T. Ito et al., "Photonic inter-module connector using silica-based optical switches", GLOBECOM' 92, pp. 187-191, 1992.

(2) Y. Inoue et al., "Nodal system architecture", NTT Review, vol. 3, no. 2, pp. 70-75, 1991.

(3) T. Sato et al., "Development of the upgraded D60 digital switching system", NTT Review, vol. 3, no. 4, pp. 69-73, 1991.

(4) S. Suzuki et al., "HDTV photonic space-division switching system using 8x8 polarization independent $LiNbO_3$ matrix switches", Tech. Digest of Photonic Switching Topical Meeting, pp. 168-170, 1989.

(5) A. Himeno et al., "Experimental optical switching system using space-division matrix switches gated by laser diodes" GLOBECOM' 88, pp. 928-932, 1988.

(6) N. Takato et al., "Silica-based single-mode waveguides on silicon and their application to guided-wave optical interferometers", IEEE J. Lightwave. Technol., vol. LT-6, pp. 1003-1010, 1988.

(7) M. Yamaguchi et al., "Experimental photonic multimedia switching system using integrated 8x8 silica-based guided-wave crossbar switch", GLOBECOM' 90, pp. 1301-1305, 1990.

(8) CCITT Recommendations (Blue Book), G707/ 708/ 709, 1988.

(9) K. Asatani et al., "CCITT standardization of network node interface of synchronous digital hierarchy", IEEE Communications Magazine, vol. 28, no. 8, pp. 15-20, 1990.

(10) A. Sugita et al., "Bridge-suspended silica-waveguide thermo-optic phase shifter and its application to Mach-Zehnder type optical switch", The Trans. IEICE, vol. E-73, no. 1, pp. 105-109, 1990.

(11) A. Sugita et al., "Strictly nonblocking 8x8 integrated matrix switch with silica-based waveguide on silicon substrated", ECOC' 90, WeG 4.1, pp. 545-548, 1990.

(12) K. Inoue et al., "Polarization sensitivity of a silica waveguide thermooptic phase

shifter for planar lightwave circuits", IEEE Photon. Technol. Lett., vol. 4, pp. 36-38, 1992.

(13) K. Takada et al., "New fiber-optic depolarizer", IEEE J. Lightwave Technol., vol. LT-4, pp. 213-219, 1986.

(14) Y. Sasaki et al., "8-km-long polarization maintaining fibre with highly stable polarization state", Electron. Lett., vol. 19, pp. 792-794, 1983.

(15) T. Miya et al., "Arrayed waveguide-type wavelength insensitive coupler for FTTH networks", in Optical Fiber Communications (OFC' 92), vol. 5, FA5, Washington DC, pp. 264, 1992.

List of publication related to this thesis

(1) T. Ito, M. Kohtoku, N. Yoshimoto, K. Kawano, S. Sekine, M. Yanagibashi, and S. Kondo, "Dynamic response of 2x2 InGaAlAs/InAlAs multiquantum well (MQW) directional coupler waveguide switch modules," Electronics Letters, vol. 30, no. 23, 1936 –1937, 1994.

(2) T. Ito, N. Yoshimoto, K. Magari, K. Kishi, and Y. Kondo, "Extremely low power consumption semiconductor optical amplifier gate for WDM applications," Electronics Letters, vol. 33, no. 21, pp. 1791 –1792, 1997.

(3) T. Ito, I. Ogawa, N. Yoshimoto, K. Magari, F. Ebisawa, Y. Yamada, Y. Yoshikuni, and Y. Hasumi, "Dynamic response of high-speed wavelength selector using hybrid integrated four-channel SS-SOA gate array on PLC platform," Electronics Letters, Vol. 34, no. 5, pp. 494 –496, 1998.

(4) T. Ito, N. Yoshimoto, K. Magari, and H. Sugiura, "Wide-band polarization-independent tensile- strained InGaAs MQW-SOA gate," The Institute of Electrical and Electronics Engineers (IEEE) Photonics Technology Letters, vol. 10, no. 5, pp. 657 –659, 1998.

(5) T. Ito, N. Yoshimoto, O. Mitomi, K. Magari, I. Ogawa, F. Ebisawa, Y. Yamada, and Y. Hasumi, "Polarization independent semiconductor optical amplifier gate and its application in WDM systems," The Institute of Electronics Information and Communication Engineers (IEICE) Transaction on Electronics, Vol. E81-C, No. 8, pp. 892-897, 1998.

(6) O. Mitomi, N. Yoshimoto, K. Magari, T. Ito, Y. Kawaguchi, Y. Suzuki, Y. Tohmori, and K. Kasaya, "Analyzing the polarization dependence in optical spot-size converter by using a semivectorial finite-element beam propagation method", IEEE J. Lightwave Technology, vol. 17, no. 7, pp. 1255-1262, 1999.

(7) T. Ito, I. Ogawa, Y. Suzaki, K. Magari, Y. Kawaguchi, and O. Mitomi, "Simultaneous wavelength conversion using SOA-PLC hybrid wavelength selector," IEICE Transaction on Electronics, Vol. E83-C, No. 6, pp. 892-897, 2000.

(8) T. Ito, I. Ogawa, Y. Suzaki, K. Magari, Y. Kawaguchi, Y. Suzuki, and N. Ishihara, "Eight-channel simultaneous wavelength conversion from equal to unequal channel spacing," IEEE Photonics Technology Letters, Vol.13, No. 10, pp. 1106 –1108, 2001.

(9) T. Ito, R. Sato, R. Kasahara, I. Ogawa, Y. Kawaguchi, Y. Inoue, Y. Kondo, Y. Tohmori, and Y. Suzuki, "Novel bit-rate and format independent PMD compensation with differential group delay monitoring using a SOA/PLC hybrid integrated wavelength converter" to be published in Electronics Letters.

(10) T. Ito, K. Magari, Y. Shibata, Y. Kawaguchi, Y. Kondo, Y. Tohmori, and Y. Suzuki, "Novel methods of estimating polarization dependence in semiconductor optical amplifiers integrated with spot-size convertors," to be published in IEICE Transaction on Electronics.

(11) T. Ito, Y. Shibata, H. Okamoto, S. Oku, Y. Kawaguchi, R. Sato, N. Kikuchi, Y. Kondo, and Y. Suzuki, "Bit-rate and format conversion from 10-Gbit/s WDM channels to a 40-Gbit/s channel using a monolithic Sagnac interferometer integrated with parallel-amplifier structure," to be published in IEE Proceeding of Opto-electronics.

Acknowledgements

I am particularly grateful to Professor Shinichi Takahashi of Keio University for his instructions and encouragement during this work. Thanks are extended to Professors Shinsuke Umegaki, Fumihiko Kannari, and Hiroyuki Tsuda at Keio University, for their valuable discussions and suggestions. I shall remain indebted to the late and much lamented Professor Shoichi Kurita for his encouragement.

Thanks are also due to Nippon Telegraph and Telephone Corporation (NTT), the author's employer, who provided the opportunity to perform the present work. I wish to express my deep gratitude to Yasuhiro Suzuki and Dr. Yuichi Tohmori for their helpful discussions and support of this work. I am also very grateful to Dr. Osamu Mitomi of NGK Insulators, LTD., and Dr. Kenji Kawano of Anritsu Corporation, who provided the initial motivation to study semiconductor devices. I would like to thank Naoto Yoshimoto, Yasuo Shibata, and Dr. Katsuaki Magari for the support on the processes, measurements, and discussions of semiconductor optical amplifier devices.

The present work was initiated and completed at NTT Photonics Laboratories. I am very thankful to Dr. Hiroshi Toba, the Project Manager of Photonic Integration Project. Thanks are also due to Yasuhiro Kondo, Dr. Hideo Sugiura, Hiroshi Okamoto, Yoshihiro Kawaguchi, Satoshi Oku, Rieko Sato, and Ken Tsuzuki, for their experimental supports.

Finally, thanks are given to my family, Ayako, Juria, Takumi, and Naoki Ito for their understading and patience, and also to my parents, Kazuo and Yasuko Ito for their lifelong encouragement.